UNIVERSITY OF MODENA AND REGGIO EMILIA
DEPARTMENT OF ENGINEERING "ENZO FERRARI"

PHD SCHOOL IN
INDUSTRIAL AND ENVIRONMENTAL ENGINEERING

XXXII CYCLE

AN INNOVATIVE HYBRID POWER UNIT ARCHITECTURE FOR SMALL VEHICLE APPLICATION: DESIGN, ANALYSIS, MANUFACTURING AND TESTING

Candidate:

Valerio Mangeruga

Tutor:

Prof. Matteo Giacopini

PhD School Coordinator:

Prof. Alberto Muscio

TABLE OF CONTENTS

1 ABSTRACT (ITALIANO)

Questa tesi presenta lo sviluppo di una *power-unit* ibrida partendo da un motore di derivazione motociclistica. Il sistema è costituito da un motore monocilindrico di 480 cc di cilindrata sviluppato sulla base del bicilindrico a V di 90 gradi della Ducati "*959 Superquadro*". Il motore termico è assistito da un motore elettrico realizzato per questa specifica applicazione (30 kW), alimentato da un pacco batterie agli ioni di litio. Il motore Ducati è stato scelto per l'elevato rapporto peso-potenza e per sfruttare il layout dell'architettura a V. Infatti, la testata verticale è stata rimossa e sostituita dal motore elettrico, direttamente collegato all'albero motore tramite la catena di distribuzione originale, ottenendo così un sistema molto compatto. Questa soluzione è adatta per molti motori a V e mira a ottenere un propulsore ibrido di piccola taglia, lasciando la porta aperta per possibili applicazioni motociclistiche.

Il motore a combustione interna di questo progetto è quindi un motore monocilindrico che risulterebbe sbilanciato rispetto alla configurazione originale (V90). Per questo motivo, sono stati analizzati diversi sistemi di equilibratura non convenzionali. In particolare, una delle soluzioni consiste nel sostituire il pistone inutilizzato con un bilanciere, ottenendo un meccanismo a quadrilatero articolato. Questa soluzione consente di ridurre le perdite per attrito e di eliminare le perdite di pompaggio. Tuttavia, è stata considerata la possibilità di mantenere il pistone originale che determina una perdita di potenza dovuta sia all'attrito che al pompaggio, ma che rappresenta però una soluzione meno invasiva.

Il comportamento meccanico della catena originale è stato valutato eseguendo un'analisi dinamica dell'intero manovellismo. In particolare, è stato fatto un confronto tra il modello del motore bicilindrico, che considera il sistema di distribuzione originale, e il modello del monocilindrico collegato al motore elettrico, al fine di valutare la possibilità di utilizzare la catena per questo scopo specifico.

Un altro aspetto importante riguarda la definizione della particolare geometria del *case* del motore elettrico, realizzato in Additive Manufacturing, al fine di includere l'alloggiamento della catena, il sistema di raffreddamento del motore elettrico e il sistema di lubrificazione. In particolare, la flangia di collegamento è progettata per adattarsi perfettamente al motore originale al fine di consentire al circuito di raffreddamento di combaciare con quello del motore elettrico. Inoltre, è stata eseguita un'analisi termo-strutturale al fine di valutare la resistenza meccanica del *case*.

Il dimensionamento del motore elettrico e del pacco batterie sono stati stimati sviluppando un foglio di calcolo che considera la potenza dissipata dal veicolo tenendo conto della massa della vettura, della resistenza al rotolamento e delle forze aerodinamiche. In particolare, il modello consente di identificare il miglior punto di funzionamento sia per il motore elettrico che per il motore a combustione interna. Sono state sviluppate diverse strategie relative alla suddivisione della potenza durante diversi cicli operativi tenendo conto delle prestazioni del veicolo, del consumo di carburante e del consumo di energia elettrica.

Infine, un primo prototipo della *powerunit* sviluppata è stato realizzato e testato al banco prova motore, fornendo così dati sperimentali utili per la validazione dei diversi modelli numerici impiegati.

1 ABSTRACT

This thesis presents the development of a hybrid power unit starting from a small engine derived from a motorcycle application. In particular, the system is made up of a brand new, single-cylinder 480 cc internal combustion engine developed on the basis of the Ducati "*959 Superquadro*" V90 2-cylinders engine. The thermal engine is assisted by a custom electric motor (30 kW), powered by a Li-Ion battery pack. The Ducati "*959 Superquadro*" engine is chosen because of its high power-to-weight ratio, and for taking advantage of its V90 2-cylinder layout. In fact, the vertical engine head is removed and it is replaced by the electric motor directly engaged to the crankshaft using the original valvetrain transmission chain, thus achieving a very compact package. This solution is suitable for many V-type engines and aims to obtain a small hybrid power unit, leaving the way open for possible motorcycle/small vehicle applications.

The resulting internal combustion engine of this project is a single cylinder engine which would result to be unbalanced if compared to the original V90 configuration. For this reason, several unconventional balancing systems are investigated. In particular, one of the solutions consists in replacing the unused piston with a balancer rod obtaining an articulated quadrilateral mechanism. This solution allows to reduce the friction losses and to specially drop off the pumping losses. In parallel, the possibility of keeping the original piston is considered which definitely represents a less invasive solution but determines a certain power loss due to both friction and pumping.

The mechanical behaviour of the original chain is investigated performing a dynamic analysis of the whole crank mechanism. In particular, the twin cylinder model considering the original valvetrain system is compared with the single cylinder model engaged with the electric motor, in order to assess the possibility to use the chain for this specific purpose.

A specific electric motor case is designed and manufactured via Additive Manufacturing technology, in order to include the chain housing, the electric motor cooling system and the lubricating system. Furthermore, the case flange is designed to perfectly fit with the original engine deck in order to allow the engine cooling circuit to match with the electric motor one. Specifically, a thermo-structural analysis is performed in order to assess the mechanical strength of the electric motor case.

The output power and size of the electric motor are estimated developing a spreadsheet which considers the power dissipated by the vehicle taking into account the mass of the car, the rolling resistance, the drag force and the lift force. Moreover, the maximum amount of energy needed is calculated thus allowing the capacity of the battery to be determined. In particular, the model allows the best operating point for both the electric motor and the internal combustion engine to be identified. Several strategies are developed concerning the power split during different operating cycles and taking into

account the vehicle performance, the fuel consumption, the electric energy consumption and CO_2 emissions.

Finally, a first prototype of the developed power unit is manufactured and tested at the bench test thus providing useful experimental data for the validation of the different numerical models employed.

2 INTRODUCTION

The automobile industry and the other industries that serve it constitute the pillar of the world's economy and employ the greatest share of the working population. However, the large number of automobiles in use around the world has caused and continues to cause serious problems for the environment and human life [1].

The transport sector is a significant and growing contributor to pollution and its share of CO_2 emissions is gradually increasing in all the regions of the world. The share of CO_2 emissions from the transport sector and its continuous growth have attracted the attention of economic, transport and climate change policy makers [2,3]. Today several technologies based on non-conventional propulsion systems are being studied in order to improve fuel economy and reduce environmental impact [4,5]. One of the most discussed innovations regards the developing and dissemination of the zero emission vehicles (ZEVs) which emits no exhaust gas from the on-board source of power generally derived from battery devices. However, battery electric vehicles (BEVs) can be considered Zero emission vehicles only locally, because they generally produce greenhouse gas in the power plants where electricity is generated. Additionally, the driving range of the BEVs are not yet comparable to the conventional internal combustion engine vehicles (ICEVs) being even heavier due to the extra weight of the batteries [6].

Hybrid electric vehicles (HEVs) combine the high fuel energy density benefits of gasoline engines and the zero pollution benefits of the electric motors [7]. The target of this project is to design a Hybrid powertrain for a light-duty vehicle (LDV) application starting from an existing engine. Consistent with European legislation, it is possible to define light-duty vehicles as four-wheel road vehicles which typically include passenger cars with no more than eight seats [8].

For a real application of the hybridization process an existing vehicle has been considered allowing the real testing process and the developing of the particular control strategies. The vehicle considered for this case of study is the Formula SAE car of the University of Modena and Reggio Emilia. By this way it is possible to define the specific boundary conditions and constraints that the hybrid *powerunit* has to comply. Although this kind of vehicle does not fit perfectly with the definition of LDV mentioned above, it meets approximately the same dimensions, weight and power at stake.

The aim of the thesis is therefore to present the benefits of electrifying a high-performance vehicle both from the performance aspects point of view, which characterizes the definition of a sports vehicle itself, as well as in terms of what concerns the environmental aspect related to lower fuel consumption and emissions to the planet.

Considering the feasibility of this application, the only FSAE event where hybrid propulsions are allowed is Formula Student UK which takes place in Silverstone circuit. Formula Student UK organizers do not provide specific rules

for hybrid powertrain [9], so it has been necessary to accord the particular limitations for the project directly with the competition judges. Substantially, the limits agreed are:

- for the IC engine a maximum engine displacement of 500 cc with a circular restriction of 20 mm diameter upstream of the intake system in order to limit the thermal power;
- regarding the electric motor a limited output power from the battery pack equal 30 kW.

The present thesis describes the design process to achieve an original and compact solution for this hybridization problem. The aim is to keep most of the engine components in order to contain costs and reduce possible reliability problems. In particular, the designed configuration is particularly suitable for V-type engines and represents a *"plug&go"* solution. In fact, it consists in replacing one of the engine heads with an electric motor connected to the crankshaft by the original valvetrain system, conforming to the maximum external sizes of the original engine. Particular attention has been also provided to keep unchanged the powertrain weight. However, also the introduction of additional components - such as battery pack and inverter - should be considered to estimate the overall weight of the hybrid *powerunit*.

In the following sections the main steps that leads to the definition of the final geometry of the electric motor housing are analysed. Specific dimensional constraints have to be considered in order to allow the replacing of the engine head with the electric motor without further modifications. Therefore, the use of the original valvetrain transmission chain is discussed considering its load capability and the transmission ratio required. In particular, a detailed dynamic analysis of the transmission chain has been performed in order to assess the correct behaviour of the chain and of the entire system.

Several electric motor cooling circuit layouts are then examined and consequently analysed through 3D CFD simulations in order to determine the most suitable solution in terms of pressure drop and heat transfer coefficients (HTC) distribution. In the final step, a detailed Finite Element thermo-structural analysis is performed in order to assess the mechanical behaviour of the component considering the HTC resulting from the CFD analysis together with the maximum loads derived from the electric motor and from the transmission chain.

Finally, a preliminary control strategy has been developed which defines how the power has to be split during vehicle operations referring to the energy management problem. An HEV can avoid low-efficiency operating points of the ICE by first storing excess power in the batteries and later using it when needed, thus providing some of the torque during short acceleration phases [10].

3 HEV ARCHITECTURES

Over the past 10 years, many automakers have turned to the development of hybrid technologies. The leading high-end car makers are presenting in recent years their interpretations of supercars and hypercars belonging to this new category of hybrid vehicles, Ferrari with the LaFerrari and SF90 Stradale, Lamborghini with concept Asterion and Sian FKP 37, Porsche with the Porsche 918 Hybrid, Mclaren with P1, Mercedes AMG with Project One and Aston Martin with Valkyrie and Valhalla.

An HEV is a vehicle in which propulsion energy is available from two or more kinds or types of sources, where at least one of them is an electric energy storage [11]. *The main issue for HEV design is controlling the energy transfer from sources to the loads with minimum loss of energy which depends on the driving cycles* [12].

The managing of the multiple sources represents an important aspect of the HEV design, which is highly dependent on driving cycles, ICE sizing, battery sizing, motor sizing, and battery management. The aim is to maximize the efficiency of the powertrain ensuring appropriate performance in terms of acceleration, range, dynamic response, comfortness, etc., also compared with ICE car [13,14].

The efficiency of an ICE strictly depends on the wideness of the load conditions. An HEV usually has a smaller ICE which can operate under less varying load, where it can be optimized for efficiency. Simultaneously, the electric motor can compensate the power requirement needed by the car. Definitely, the ICE ensures an extended driving range to the hybrid vehicle, while the EM increases efficiency and fuel economy also regenerating energy during braking and storing the exceeding energy produced by the ICE into the batteries [15]. Unlike a pure electric vehicle, a hybrid electric vehicle does not require an external battery charging system, so it can be independent of charging infrastructures. However, a HEV can also be plug-in, if a battery charging system is inserted on board the vehicle by connecting to the electric grid as a pure electric vehicle [16,17]. The most common HEV architectures can be divided into three types: Series, Parallel and a combination of both [18].

The most common architecture is the ICE vehicle which represents the basis for the following description of the various hybrid configurations. An ICE vehicle presents a long driving range and a short refuelling time, but it is currently related to pollution and fuel consumption problems. In Figure 3.1, the Internal Combustion Engine is denoted as ICE, the fuel tank as Fuel, the Transmission as Trans, the battery as BAT, the Voltage Source Inverter as VSI, the Electric Motor as EM. Moreover, the orange lines identify the mechanical couplings and the black lines are used to identify the electric connections. The grey items with dashed edges represent the components not existing in the ICE architecture observed.

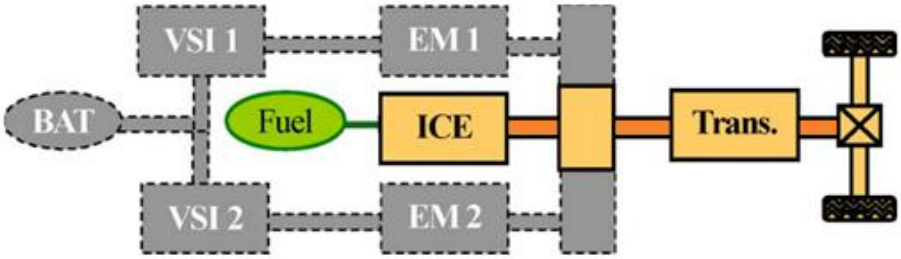

Figure 3.1. ICE vehicle architecture [15].

3.1 SERIES HEV

It is possible to consider a series hybrid vehicle such as an electric vehicle equipped with an on-board battery charger represented by the ICE. The ICE is connected to the generator (EM2 in Figure 3.2) and it generally runs at an optimal efficiency point in order to better convert the fuel energy and charge the propulsion batteries. The converted electricity from the batteries can be used to propel the wheels via EM1 and the transmission (Figure 3.2). However, there are two energy conversion stages: the first is during the transformation of the fuel energy into electric energy, and the second is the conversion of the latter in mechanical energy. Each conversion presents a specific efficiency, so some energy is definitely lost during this process. It must be noted that the ICE has no mechanical connection with the wheels, which means it never directly powers the vehicle [15,19]. Thanks to the excellent performance of the electric motor also at the low revs, it is possible to avoid the oversizing of the ICE as it generally has to ensure good performance in acceleration. Therefore, downsizing is carried out keeping the ICE works at a fixed-point following the best efficiency approach. Then, the torque value depends on the engine speed at which there is the lowest specific fuel consumption. The torque feature of the electric motor allows the elimination of the multiple-speed gearbox by simplifying the entire transmission. However, it can be useful to consider a two-speed gearbox for braking analysis purposes (recovery of electricity). If the car exists both in a purely electric version (therefore necessarily plug-in) and in a hybrid series version (not necessarily plug-in thanks to the ICE), then this second variant can be considered as an evolution of the pure electric version that can guarantee a longer range, and it is in fact called *electric with range extender*. [16,20–22].

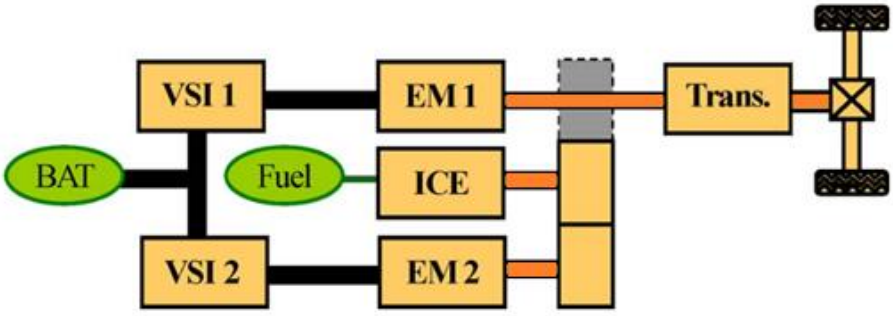

Figure 3.2. Series HEV [15].

3.2 PARALLEL HEV

The parallel hybrid architecture has been the powertrain of choice for their first step into vehicle electrification [23]. In a parallel powertrain, both ICE and EM are connected to the wheels and the traction power can be supplied by ICE alone, by EM1 alone, or by both acting together (see Figure 3.3). Many modes of operation exist depending on the particular transmission mechanism adopted to couple the EM to the ICE [24]. It is possible to charge the battery using the EM1 during braking or when the power output of the ICE is greater than the power required to drive the wheels. This parallel HEV architecture requires only one electric motor (EM1) and the ICE. In addition, a smaller engine and a smaller electric motor can be used to obtain the same dynamic performance. *Even for long trip operation, only the engine needs to be rated for the maximum sustained power, while the electric motor may still be about half* [25]. However, the ICE cannot always operate in its optimal region because of the mechanical coupling between the ICE and the transmission, and thus, clutches are often necessary in order to allow the decoupling of the two machines [15].

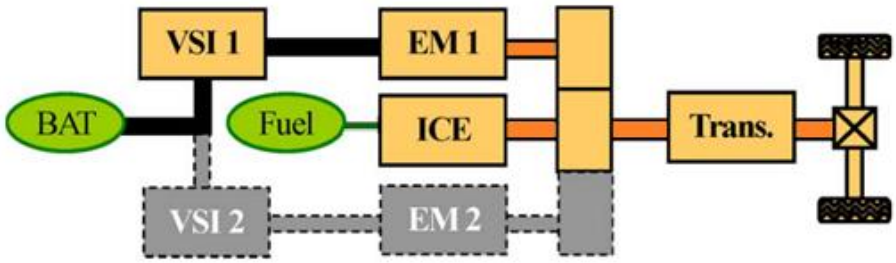

Figure 3.3. Parallel HEV [15].

Parallel hybrid architectures can be categorised into several configurations, depending on the relative position of the electric motor with respect to the ICE, which are typically referred as *P0* to *P4*, shown in Figure 3.4.

In particular, in the configuration *P0* the EM is engaged to the ICE using a belt or a chain. Consequently, the efficiency results to be limited due to the belt/chain losses. In the configuration *P1* the EM is directly mounted coaxial on the crankshaft, so it is restricted to the length of the axis. This provides higher torque than the *P0* architecture due to the absence of a belt/chain drive, so with no belt losses there is a greater efficiency. In the configuration *P2* the EM is located on the gearbox primary shaft before the starting clutch (*C0*). This layout also provides a mechanical disconnection between the EM and the ICE by activating the clutch *C1*. By this way it is possible to drive in full electric mode keeping the advantages of the gearbox. Similarly, also the configuration *P3* allows the full electric drive but it is not possible to use the gearbox because the EM is engaged to the gearbox output (secondary shaft). Both configurations *P2* and *P3* ensure a better efficiency but lead to higher costs. In the configuration *P4* the EM is connected directly to the halfshaft thus providing 4-wheel drive capabilities and the increase of the recovered energy. [23,26]

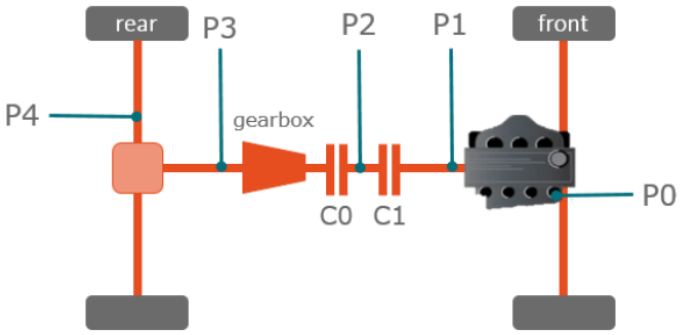

Figure 3.4. Hybrid parallel powertrain configurations.

Finally, it is possible to combine series and parallel architectures in order to take the advantages of both configurations. The resulting architecture allows more control strategies, but it is a more complex and expensive system. Nevertheless, this configuration is quickly becoming the standard in passenger vehicle hybridization. [27–30]

3.3 FORMULA 1 HYBRID ARCHITECTURE

Another interesting application to be mentioned concerns the Formula 1 hybrid architecture developed in the last years because of new regulations that include multiple energy recovery systems and fuel flow restrictions. The new formula reintroduced turbocharged engines, which last appeared in 1988. These *powerunits* present an efficiency improved by turbo-compounding and by the introduction of more energy recovery systems, with energy to be recovered from the brakes and exhaust gases. A compromise was reached to adopt V6 turbocharged engines instead. The internal combustion engines are limited to 15,000 rpm, but rarely exceed 12,000 rpm during a Grand Prix due to the new reliability and fuel flow restrictions. Energy recovery systems such as KERS had a boost of 160hp and 2 MJ per lap. KERS was renamed as Motor Generator Unit-Kinetic (MGU-K). The power in the MGU-K is known to be able to power along a family saloon nicely. Heat energy recovery systems were also allowed, under the name Motor Generator Unit-Heat (MGU-H). [31,32]

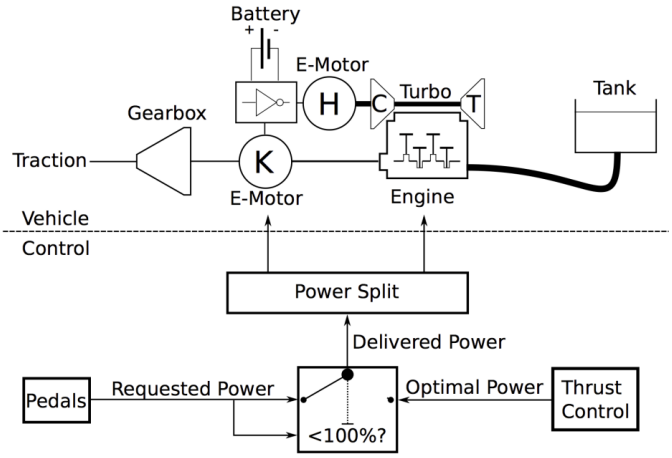

Figure 3.5. Formula 1 Hybrid Powerunit layout.

4 HYBRID POWERTRAIN

For this specific project a parallel hybrid configuration has been chosen for the particular simplicity of this architecture. In fact, one of the main targets is to perform the hybridization process in a non-invasive way obtaining a *plug&go* solution. In this section the different choices of the EM and the ICE are discussed considering the application field. In particular, the vehicle considered is a Formula SAE car which well represents the dimensions and the performance required for the project which is focused on a small vehicle application.

This section describes the proposed hybrid *powerunit* starting from the internal combustion engine choice and the design of the electric motor. In particular, specific sections are dedicated to the changes made on the ICE, the sizing of the EM, the design of the EM case including the thermo-structural analysis and the CFD analysis of the cooling system. Moreover, also a brief mention about the energy storage system is included.

A competitive Formula SAE vehicle needs to be compact and lightweight, so all the components must be as lighter as possible. The *Ducati 959 Panigale* engine results to be a good compromise between weight and power output. Table 1 summarizes the main characteristics of the thermal engine chosen.

Displaced volume	955 cc
Lay-out	2-cylinders, V90°
Bore x Stroke	100 x 60.8 mm
Compression ratio	12.6:1
Number of Valves per cylinder	4
Type of valve actuation	Desmodromic
Fuel metering	Gasoline Port Injection
Maximum Power	110 kW @ 10,500 rpm
Maximum Torque	102 Nm @ 9,000 rpm
Dry weight	59 kg

Table 1. Ducati 959 Panigale engine.

The total displacement of this engine exceeds the maximum value agreed with Formula SAE judges. Therefore, an important focus of the project is the modification of the layout of the stock engine in order to comply the allowed displacement. In particular, the displacement almost doubles the limit, but this is what we are searching for. In fact, one of the cylinders has been switched to a passive mechanism and consequently one of the engine head has been removed (head 1 in Figure 4.1). The head has been subsequently replaced by the electric motor (EM in Figure 4.2) engaged directly to the crankshaft using the original valvetrain transmission chain. The aim is to obtain a solution suitable for generic V-type engines. The choice of the head to be replaced has been dictated by the vehicle assembly arrangements. In particular, head 2 better fits with an easy intake and exhaust system layout.

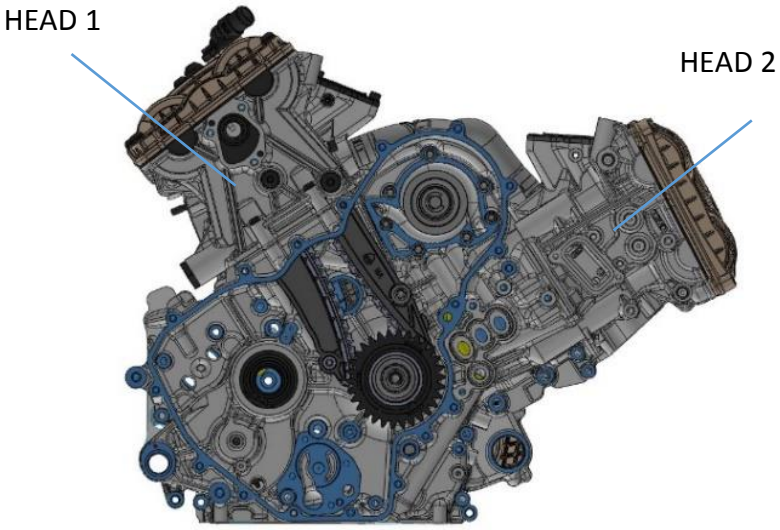

Figure 4.1. Stock engine layout.

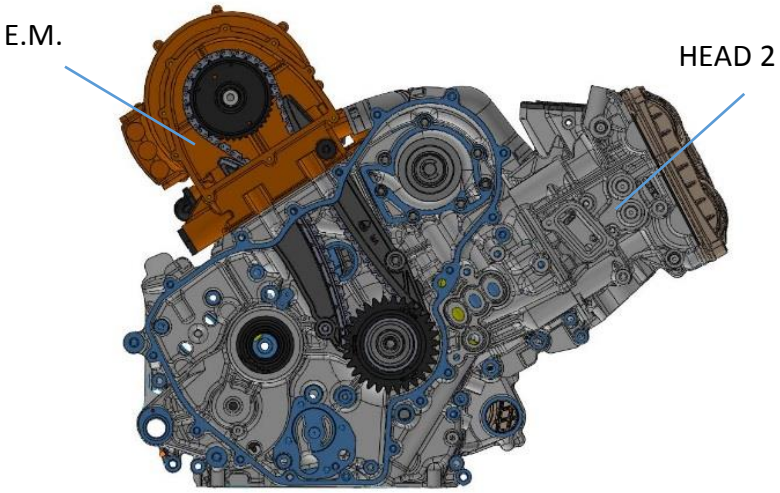

Figure 4.2. Hybrid layout.

The resulting hybrid architecture is named *parallel hybrid* [30] in which the output of the engine and the electric motor are blended together upstream of the transmission. In particular, this architecture refers to the configuration *P0* (described in the section 3) as the EM is connected directly to the ICE crankshaft with a transmission chain. The electric motor provides an extra boost and it allows the battery charging during braking. In detail, the layout adopted is schematized in Figure 4.3.

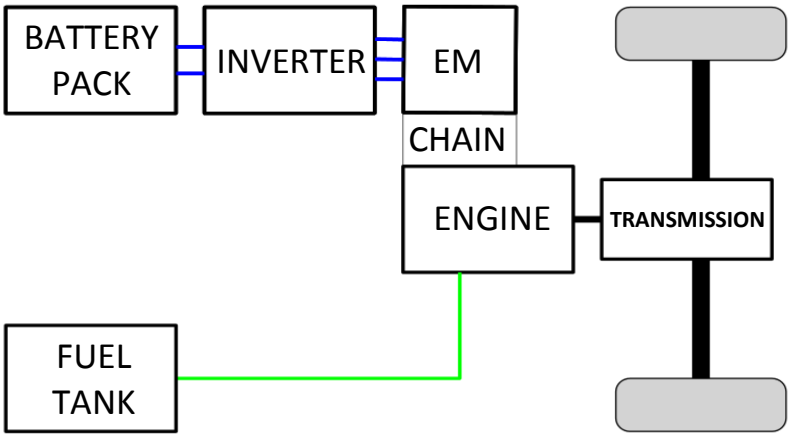

Figure 4.3. Parallel hybrid layout. The blue lines indicate the electrical connection, the green lines represent the fuel feeding and the black lines represent the mechanical connections.

4.1 INTERNAL COMBUSTION ENGINE

The resulting single cylinder internal combustion engine has a displacement equal to half of the original one. In particular, a complete CFD-1D simulation of the ICE has been performed and discussed in a specific study [33] and of which only the results are reported. The simulated values of power and torque are shown in Table 2, which take into account the displacement variation and the influence of the restrictor.

Displaced volume	477 cc
Bore x Stroke	100 x 60.8 mm
Maximum Power	46 kW @ 10,500 rpm
Maximum Torque	44 Nm @ 8,500 rpm

Table 2. Single cylinder ICE power and torque.

Figure 4.4 shows power and torque curves extrapolated from the 1D simulations.

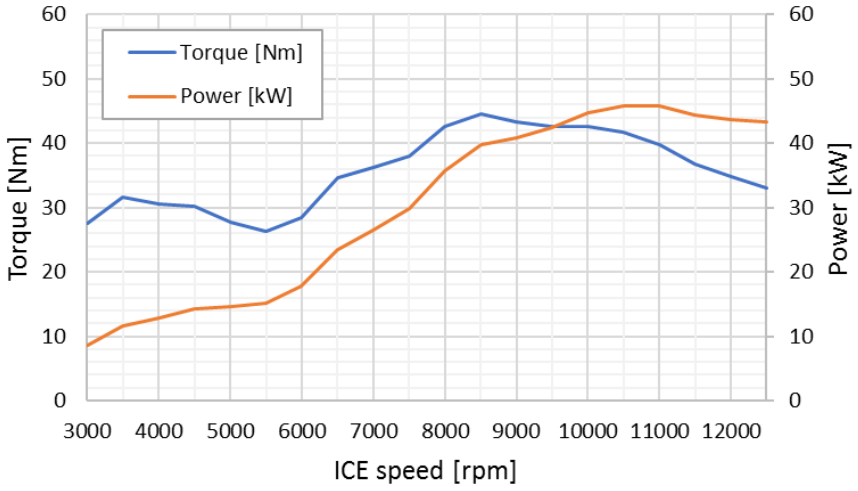

Figure 4.4. Single cylinder internal combustion engine: full load performance predicted by GT-Power model.

A complete experimental campaign has been performed on the single cylinder engine using the dynamometer bench of the university. The engine is mounted on the bench without the EM, so only the thermal engine is considered in order to validate the 1D model of the ICE. In particular, both intake and exhaust system have been redesigned in order to optimize the actual single cylinder engine configuration. Consequently, a calibration process of the engine has been necessary focusing on fuel consumption, power, regularity and reliability of the ICE.

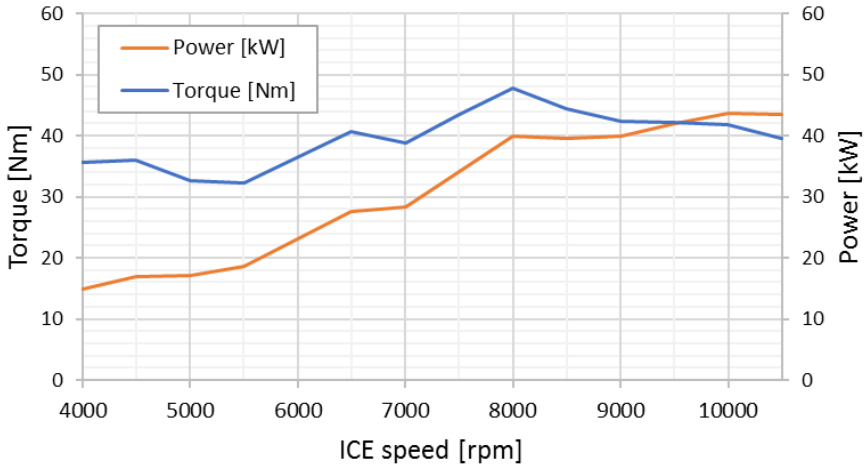

Figure 4.5. Single cylinder internal combustion engine: full load performance derived from experimental tests.

Moreover, ICE torque curves at several loads have been collected obtaining a complete torque map of the ICE. Similarly, the *brake specific fuel consumption* (*BSFC*) has been measured at each engine load and speed. These data are useful for the implementation of the hybrid *powerunit* control, described in a following section.

Another important focus about the ICE modifying steps consists on the balancing system. A dedicated section has been considered describing the fundamentals of the engine balancing systems (section 5). Although different solutions have been investigated (described in section 0 and 0), finally, it has been decided to keep the original V90 architecture of the crank mechanism (with the sole modification of the passive piston geometry in order to annul its compression capabilities) because of its natural balancing with respect to the first order inertial reciprocating forces. In fact, other balancing systems showed a comparable weight, but presented higher costs and possible reliability problems.

4.2 ENERGY STORAGE SYSTEMS

Powertrain hybridization as well as electrical energy management are imposing new requirements on *electrical storage systems (ESSs)* in vehicles. This requirements for the ESSs include cycle life, high dynamic charge acceptance particularly for regenerative braking and robust service life in sustained partial-state-of-charge usage [34,35].

In general, the most common *energy storage systems* developed in the automotive field are *batteries*, *supercapacitors*, *flywheels* and *fuel cells*.

Supercapacitors are devices capable of managing high power rates compared to batteries, but they are not able to store the same amount of charge as batteries do. *Supercapacitors* can be used for high-power requirements such as regenerative braking [36].

The *flywheel* system consists of a large rotating disk where the kinetic energy is stored and a motor/generator which is coupled to the flywheel to convert kinetic to electrical energy. So, this system stores energy in the kinetic form, which can then be transformed into electricity. Sometimes, this kind of architecture is named mechanical hybrid, because the energy accumulator consists of a kinematic device [37].

Fuel cells is a device that takes fuel as input and produces electricity as output. *Fuel cells* are powered by hydrogen, which could be produced remotely as a part of the hydrogen economy. Consequently, this system requires on-board tanks for the hydrogen storage [38].

Batteries have been one of the main focuses of automotive development in the last years. Technologies that have been in use for a very long time, such as the *lead–acid* battery, are indispensable but need improvement. The variety of vehicles has increased with the introduction of hybrid vehicles, plug-in hybrid vehicles and electric vehicles and, for each type, suitable battery types are being used or are under development. Appropriate battery system designs and charging strategies are needed. Battery technologies can be classified according to their energy density, their charge and discharge characteristics, system integration and costs. Further relevant performance parameters are the cycle lifetime, the low and high temperature performances and the safety [39].

Figure 4.6 compares all types of electrified vehicle with respect to the energy and power demand.

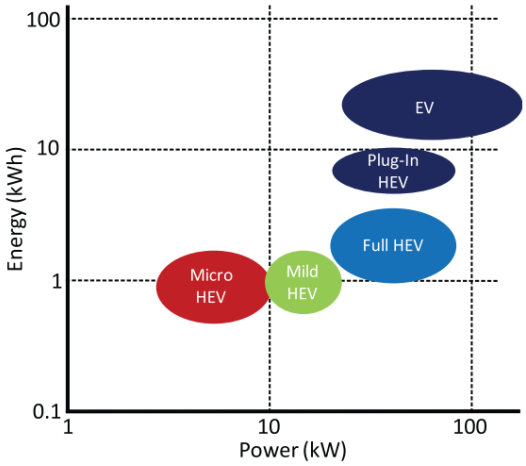

Figure 4.6. Energy and power demands on batteries for different types of vehicle [39].

The different battery technologies can be classified based on various characteristics. The most important parameters are described as follows.

- The *gravimetric power density* (also called the *specific power density*) and the *volumetric power density* are among the most important parameters for hybrid vehicles. High values usually imply a low electrical resistance, resulting in low energy losses and high-power capability.
- Besides the power, the *gravimetric energy density* (also called the *specific energy density*) and the *volumetric energy density* are important as well. *Supercapacitors* can certainly deliver a high power, but only for a short time, while the energy density of batteries is higher. Figure 4.7 gives an overview of the specific gravimetric power and energy density of batteries.
- The ratio of the discharged energy to the charged energy is the *energy efficiency*. Energy losses are transformed into heat and must be removed to avoid overheating of the batteries.
- The *cycle lifetime*, on the other hand, describes how many cycles the battery can perform until it fails. The *cycle lifetime* depends on the cycle depth, current rate and average State of Charge (SOC). The capacity turnover is measured in full equivalent cycles.
- Besides technical aspects, the *costs* are relevant for choosing a battery system. However, the costs strongly depend on the specific requirements and the quality of the battery.

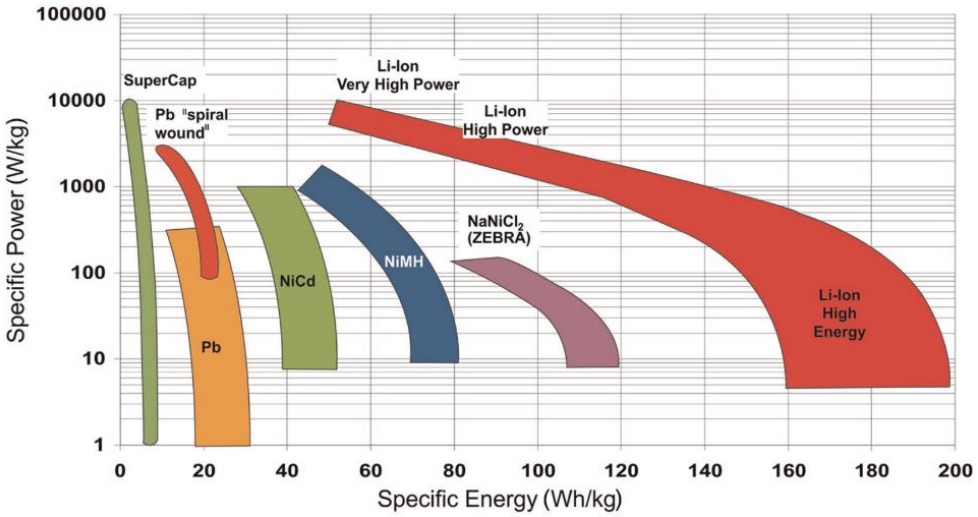

Figure 4.7. Ragone plot of various battery technologies with specification at cell level for automotive applications [39]. *SuperCap: supercapacitor; Pb: lead; Li-ion: lithium-ion; NiCd: nickel–cadmium; NiMH: nickel–metal hydride; NaNiCl2: sodium–nickel chloride.*

Some of the batteries widely diffused in the automotive sector are *acid lead*, *metal hydrocarbons* and *lithium-ions* batteries. *Acid lead* batteries are the cheapest batteries used in vehicles where there is no high demand for power and energy density, generally used in traditional vehicles for *starting-lighting-ignition (SLI)* application (i.e. for electric auxiliary devices and the vehicle's starter). *Metallic hydrocarbon* batteries are used for mild and full hybrid vehicles. They provide a higher energy and power density than the former, but the price is definitely higher. Finally, *lithium-ion* batteries, which entered the market in the early 1990s, are the most expensive, but they can provide high energy density and power values, about 3-4 higher than acid lead batteries. They are currently widely used in new electric and hybrid vehicles [40]. Table 3 shows the main characteristics of the types of batteries listed:

	Lead Acid	**Metal Hydrocarbon**	**Lithium Ions**
SPECIFIC ENERGY [Wh/kg]	30-50	60-120	100-265
SPECIFIC POWER [W/kg]	75-300	250-1000	250-340
ENERGY EFFICIENCY [%]	70-80	60-70	85-98
AUTO-DISCHARGE [%/DAY]	0.033	2.5-3.0	0.1-0.3
LIFE CYCLES	100-2000	500-1000	500-3000
COST for POWER UNIT [$/kW]	175-600	150-1500	175-4000
COST for ENERGY UNIT [$/kWh]	150-400	150-1500	500-2500

Table 3. Key features of the three battery categories: Lead Acid, Metal Hydrocarbons, and Lithium Ions.

The *lithium-ion* battery technology has been considered for this specific application. In particular, the cell takes advantage of the chemical intercalation mechanism, which consists of inserting lithium ions between the graphite layers during the charging phase, while in the discharge phase the lithium ions

come out of the material to carbon. Lithium ions oscillate through the electrolyte and separator, from one electrode to another. During the discharge process the ions pass from the negative electrode to the positive, vice versa for the charging process, leaving the graphite structure intact [41].

The main lithium-ion batteries are: *Lithium-Cobalt* (LCO), which despite being used by some car manufacturers is not considered safe for the automotive sector, *Lithium-Oxide of Manganese* (LMO), *Lithium-Nickel-Manganese-Cobalto* (NMC), *Lithium-Nickel-Cobalt-Aluminum* (NCA) and *Lithium-Ferro-Phosphate* (LFP). Another category is *Lithium-Titanium* (LTO), whose acronym derives from the lithium titanium oxide anode, and the cathode is graphite [41]. In the following are briefly described the main features of each battery family:

- *Lithium-Cobalt (LCO)*: has a nominal cell voltage of 3.6V and a specific energy of 200Wh/kg. It has a reduced self-discharge allowing to carry out between 500 and 1000 discharge cycles. The disadvantages are the high cost due to cobalt, the safety, low thermal stability and the loss of capacity in presence of deep discharge-charge cycles;
- *Lithium-oxide of manganese (LMO)*: it has a nominal cell voltage equal to 3.8V, a specific energy of 100-150Wh/kg and can reach 300-700 life cycles. It is also not a toxic material, costs less and possesses a high thermal stability compared to Lithium-Cobalt;
- *Lithium-Nickel-Manganese-Cobalt (NMC)*: the combination of these elements results in more specific energy and longer battery life. It has a nominal voltage of 3.6-3.7V, specific energy 150-220 Wh/kg and 1000-2000 life cycles. In addition, the use of a lower concentration of cobalt reduces costs and safety issues.
- *Lithium-Nickel-Cobalt-Aluminium (NCA)*: it has similar characteristics to the battery shown above: 3.6V nominal voltage, 150-220 Wh/kg specific energy and high battery life. In addition, the presence of aluminium improves thermal stability and electrochemical performance. The disadvantages are the high cost and low security.
- *Lithium-Ferro-Phosphate (LFP)*: has a nominal voltage of 3.2V, a specific energy of 90-120Wh/kg and 1000-2000 life cycles. The main advantages are thermal stability at high temperatures, high safety and low cost. On the other, it has a larger self-discharge.
- *Lithium-Titanium (LTO)*: has a nominal voltage of 204V, a specific energy of 70-110Wh/kg and a lifespan of 1000 life cycles. The main advantages are safety due to the lack of carbon and high thermal stability, on the other side the cost is high.

4.2.1 Battery

The battery typology chosen for this specific application is the cylindrical cells referred to the *Sony VTC6* in the *18650* format. The dimensions of the cell are a diameter of 18mm and a length of about 65 mm. The chemistry of the Sony VTC6 batteries is the *lithium-oxide of manganese*. Each cell presents a 3000mAh capacity and a maximum continuous discharged current of 15A, according to Sony; however, if the temperature of the cell remains below 80°C, the continuous discharge current increases to a notable 30A.

Battery systems for HEVs require the batteries to be combined into packs made up of multiple cells connected together. In particular, battery cells are arranged in battery modules which represent a separate subsystem with internal electrical circuits. The cells are connected in series and parallels in order to achieve the desired pack voltage and capacity [42].

For this specific application, the battery pack has been dimensioned starting from a need of 30 kW of power, corresponding to the limit imposed by the FSAE rules, as discussed in the introduction section.

Each pack consists of three 90-cells modules for a total of 270 cells, in a 27 series and 10 parallels configuration. Consequently, the total rated voltage is about 100 V and the maximum current is 300 A. Important aspects in pack design are mechanical requirements such as vibration and shock resistance, as well as how to handle temperature management.

A new concept for the installation of the cells in the pack has been developed, allowing for compactness, avoiding weldings and enabling efficient water cooling (Figure 4.8). In particular, the cells are connected each other by means of a copper plate which works as the conductor. An important role is represented by the contact area between the conductor and the cell. Although the welding process is easier to be developed, it hardly ensures repeatable and predictable contact area. Consequently, another solution consists on applying an axial force on the cells generating a certain contact pressure, ensuring a minimum contact area which strictly affects the electrical contact resistance [43]. However, the cells considered present a certain dimensional tolerance on the cell length. So, specific cup springs have been considered under each cell in order to ensure a constant force (thus contact area) on every single cell. The spring has been designed considering the stiffness of the single spring, the minimum force needed and achieving a displacement-control assembly using specific spacers. Moreover, this solution promotes the maintenance allowing each cell to be easily replaced with respect to the welded cells.

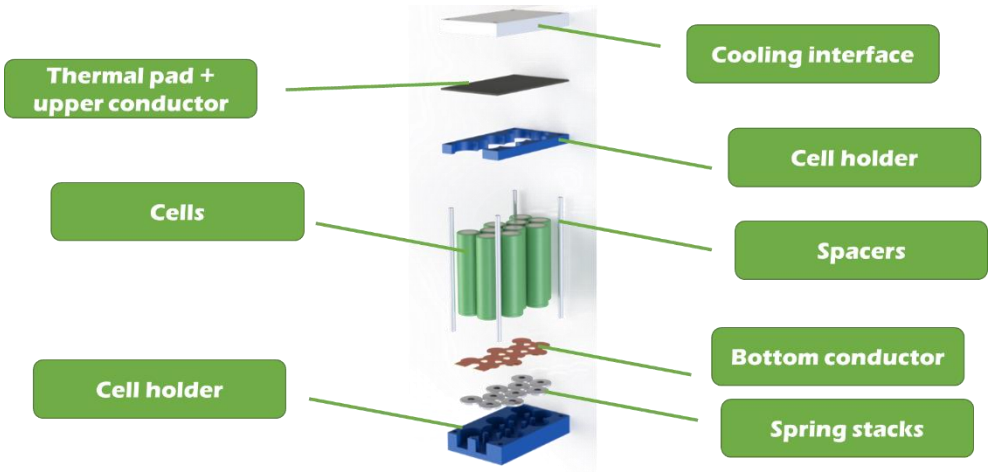

Figure 4.8. Assembly of an example module describing the proposed concept.

Lithium-ion batteries also require a monitoring system in order to control each cell, in terms of temperature and voltage. The *battery monitoring system (BMS)* is an electronic system that manages the battery pack protecting it from operating outside its safe operating area, monitoring its state, reporting that data, controlling its environment and providing the balance of the cells [44]. The *battery monitoring system (BMS)* module is located on the top of the battery modules together with the other power electronics devices (Figure 4.9).

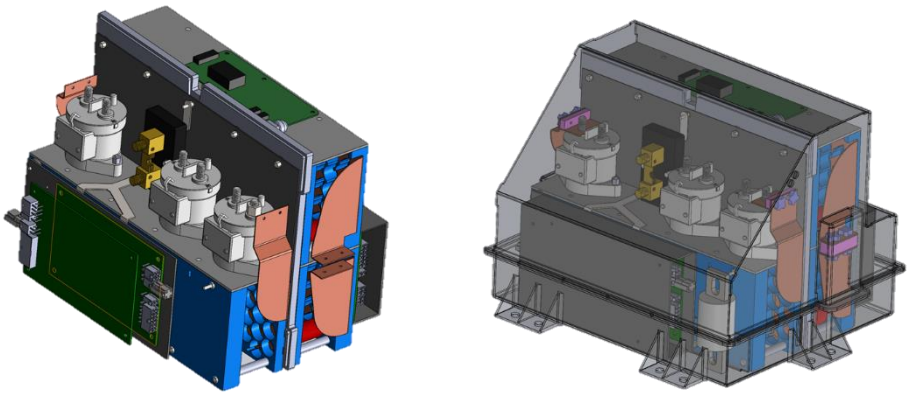

Figure 4.9. Battery pack assembly (on the left) and steel housing (on the right).

The battery modules, the BMS, the wiring and the cooling system, are inserted in a pack housing made of steel in order to protect the components against mechanical and thermal impacts.

4.3 ELECTRIC MOTOR

The selection of the electric motor for hybrid propulsion systems is a very important step that requires particular attention. In fact, *the automotive industry is still seeking for the most appropriate electric-propulsion system for hybrid electric vehicles (HEVs) and even for EVs*. The choice of the electric-propulsion system for HEVs mainly depends on three factors: driver expectation, vehicle constraints, and energy source. Driver expectation is defined by a driving profile, which includes the acceleration, maximum speed, climbing capability, braking, and range. Vehicle constraints, including volume and weight, depend on vehicle type, vehicle weight, and payload. The energy source is related to batteries, fuel cells, ultracapacitors, flywheels, and various hybrid sources [45]. In this case, key features are the interaction with the engine, reliability, and cost.

The motor drives can be classified into two main groups, namely the *commutator* motors and *commutatorless* motors. *Commutator* motors mainly are the traditional DC motors, which include *series excited*, *shunt excited*, *compound excited*, *separately excited*, and *permanent magnet* (PM) excited motors. DC motors need commutators and brushes to feed current into the armature, thus making them less reliable and unsuitable for maintenance-free operation and high speed. In addition, winding excited DC motors have low specific power density. On the contrary, *commutatorless* electric motors present several advantages including higher efficiency, higher power density and lower operating costs. They are also more reliable and maintenance-free compared to commutator DC motors because of the lack of brushes. Thus, *commutatorless* electric motors are widely used for HEVs and EVs applications [46].

Focusing on the *commutatorless* electric motors, the major types of electric motors adopted or under serious consideration for HEVs, as well as for EVs, include the *Induction Motors (IM)*, the *Permanent-Magnet Synchronous Motors (PMSM)* and the *Switched Reluctance Motors (SRM)* [45].

Induction Motors (IM)

Induction Motors (IM) are widely accepted as a *commutatorless* motor type for EV and HEV propulsion. This is because of their low cost, high reliability, and maintenance-free operation. However, conventional control of induction motors such as *variable-voltage variable-frequency* (VVVF) cannot provide the desired performance, suffering low efficiency at low light loads and limited constant-power operating range [47].

Permanent-Magnet Synchronous Motors (PMSM)

Permanent-Magnet Synchronous Motors can eliminate conventional brushes, slip rings, and field copper losses, by replacing the field winding of conventional synchronous motors with PMs [48]. Actually, these PM synchronous motors are also called *PM brushless AC motors*. When PMs are mounted on the rotor surface, they behave as *nonsalient* synchronous motors because the

permeability of PMs is similar to that of air. By burying those PMs inside the magnetic circuit of the rotor, the saliency causes an additional reluctance torque, which leads to facilitating a wider speed range at constant power operation [49].

Switched reluctance motors (SRM)

Switched reluctance motors (SRM) have been recognized to have considerable potential for EV and HEV applications. SRMs have the definite advantages of simple construction, low manufacturing cost, and outstanding torque-speed characteristics for EV and HEV applications. Although they possess simplicity in construction, this does not imply any simplicity of their design and control. Because of the heavy saturation of pole tips and the fringe effect of pole and slots, their design and control are difficult and subtle [46]. Traditionally, SR motors operate with shaft sensors to detect the relative position of the rotor to the stator. These sensors are usually vulnerable to mechanical shock and sensitive to temperature and dust, reducing the reliability of SRMs. Moreover, SRMs generate acoustic noise causing several NVH issues and constraining some applications [50].

Regarding the energy efficiency issue, the selection of an appropriate type of traction motor is very complicated. Motor efficiency is significantly influenced by material quality, design parameters and control technology. It is possible to consider two dominating motor losses, such as copper loss and iron loss. Copper loss is squarely proportional to the motor current. In IM and SRM, a portion of this current is also the motor magnetizing current, which produces magnetization or excitation loss. PMSM is naturally excited through magnets and, therefore, has no excitation loss. However, this is only true below the base speed of the motor. Above the base speed, PMSM requires external excitation to weaken its naturally existing magnetic field. Therefore, torque per copper loss is inherently better below the base speed in PMSM. Moreover, at very high speed, iron loss becomes significant. Iron losses are a function of flux density and frequency of flux alternation. The PMSM has rotor magnets so it has theoretically zero rotor iron loss. The only iron loss in PMSM is in the stator side [51,52].

In this study, PMSM is found to be best suited for the specific constraints. Then, the electric propulsion is committed to a PMSM expressly designed for this specific application. In particular, the rotor and the assembled stator with coils winding have been developed in collaboration with the *Promo srl* company. The details of the particular winding layout are not reported in this treatise.

The requirements needed for the definition of the EM are listed below:

1. External sizes of stator and rotor, such as diameter and length, must not exceed the overall dimensions of the replaced ICE head. In fact, the EM has to fit with the free space created by removing the ICE head. Since the position of the EM axis is constrained by the original transmission layout, the maximum external diameter of the stator is limited.

2. Considering that the EM has to be directly connected to the ICE, the maximum speed of the EM strictly depends on the transmission ratio between the crankshaft and the EM shaft. Known the maximum ICE speed it is possible to evaluate the corresponding maximum EM speed. In particular, the specific considerations on the transmission ratio are discussed in the following section.

3. The power that the EM has to manage is imposed by agreed FSAE rules. The aim is then to achieve a continuous power lower than this limit and a peak power a bit higher in order to use the EM in safety conditions.

According with these requirements, the dimensions of the stator and the rotor are summarized in the Table 4.

	Stator	**Rotor**
Outer diameter	135 [mm]	80 [mm]
Inner diameter	82 [mm]	30 [mm]
Length	94 [mm]	96 [mm]

Table 4. Overall dimensions of stator and rotor of the electric motor.

The outer diameter of the stator influences the external profile of the EM housing. Moreover, considering both the external diameter and the axial length of the stator it is possible to determine the interference fit needed, based on the maximum torque to be transmitted. The difference between the stator inner radius and the rotor outer radius represents the air gap thickness, in this case selected equal to 1 mm. Finally, the rotor inner diameter and length are parameters which affect the EM shaft design.

The specifications of the electric motor chosen in order to respect the mentioned features are shown in Table 5.

Supply Voltage	96	VAC
Continuous torque	19.5	Nm
Speed @ continuous torque	0-9600	rpm
Continuous power	19.5	kW
Speed @ continuous power	9600	rpm
Peak torque	36.5	Nm
Speed @ peak torque	0-8600	rpm
Peak power	32.5	kW
Speed @ peak power	8600	rpm

Table 5. Technical specifications of the electric motor.

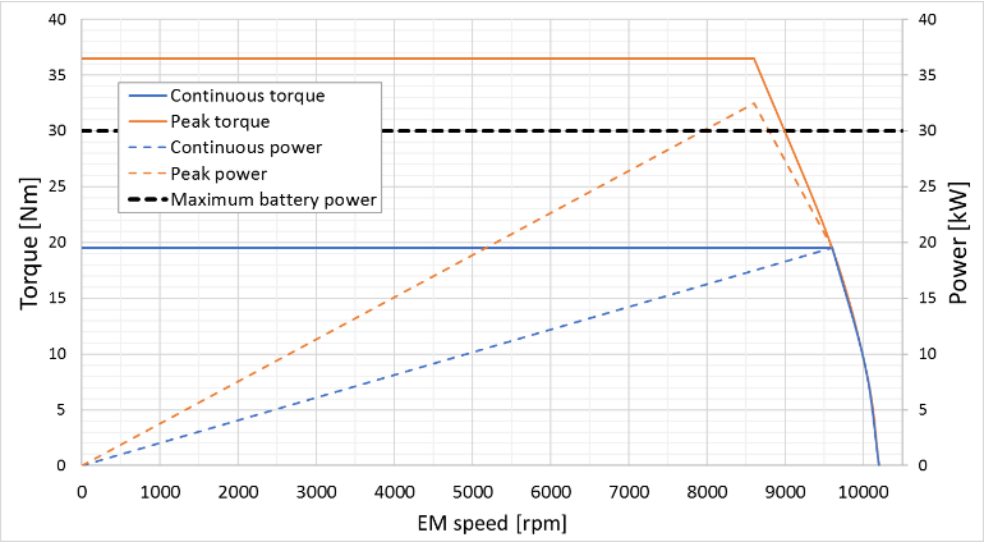

Figure 4.10. Continuous and peak power and torque curves of the electric motor.

Figure 4.10 depicts theoretical power and torque curves of the electric motor. The blue lines represent the continuous power and torque delivered by the EM, while the orange curves are referred to overload conditions. Actually, it is not possible to overload the motor above 30 kW because of the value imposed by the rules, which limit the maximum power output from the battery.

4.4 EM TRANSMISSION/DRIVE

The *valvetrain* transmission system of the original engine consists of both a timing chain and transmission gears, see Figure 4.11. Consequently, two different transmission ratios have to be considered referred respectively to the chain and the gears. The chain is kept in position by two guide rails: one is fixed (fixed guide rail in Figure 4.11) and the other can rotate in order to adjust the chain tension (floating guide rail in Figure 4.11). This task is entrusted by the hydraulic chain tensioner that ensure the proper tension during operating conditions.

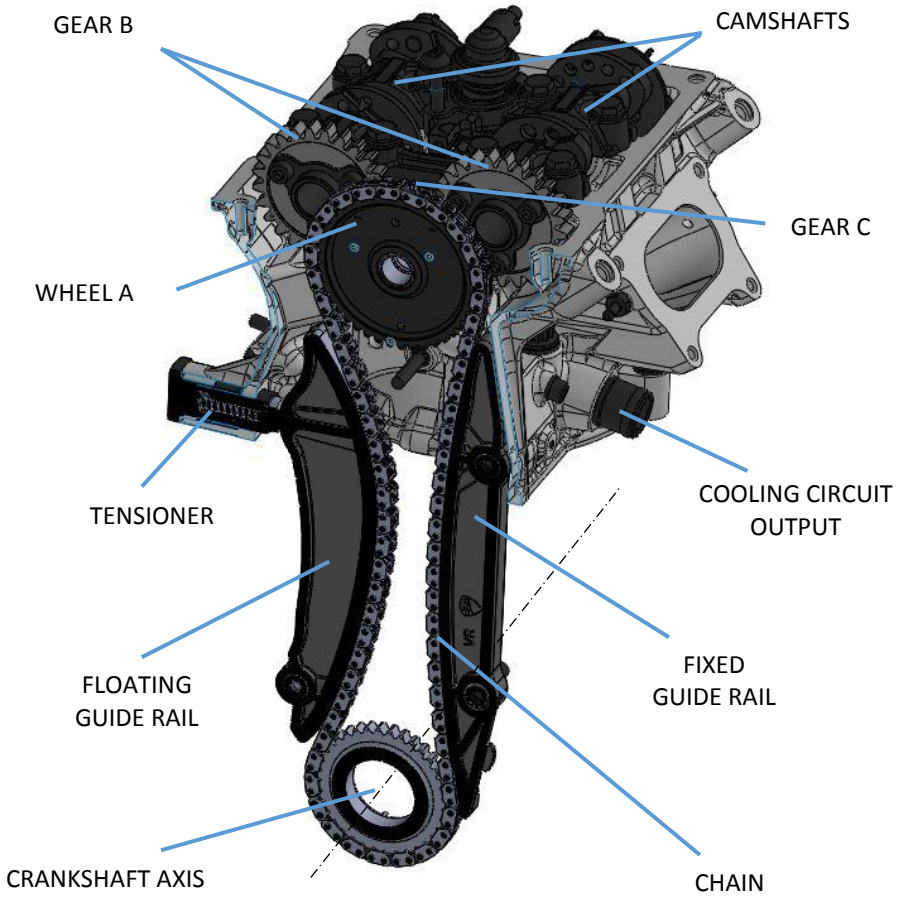

Figure 4.11. Original valvetrain transmission system layout.

Obviously, the original total transmission ratio is such that it makes the camshafts rotating at half of the speed of the crankshaft. In particular:

$$\tau_{\text{tot}} = \tau_{\text{chain}} \cdot \tau_{\text{gear}} = 1.20 \cdot 1.667 = 2 \qquad (4.1)$$

where τ_{chain} is the transmission ratio of the chain alone, and τ_{gear} is the transmission ratio between the gear B and C (Figure 4.11). The gear C is better identified in the Figure 4.12.

However, removing the camshafts, also gears B (Figure 4.11) are removed. Consequently, the EM shaft is directly connected to the chain upper wheel (wheel A in Figure 4.11) being the transmission ratio in this configuration equal to 1.2 (τ_{chain}).

Originally, the wheel hub did not provide any torque transmission device (as a keyed joint) because it was an idler gear. Therefore, a simple key seat has been added to the original wheel design in order to allow the torque transmission from the EM shaft to the ICE crankshaft.

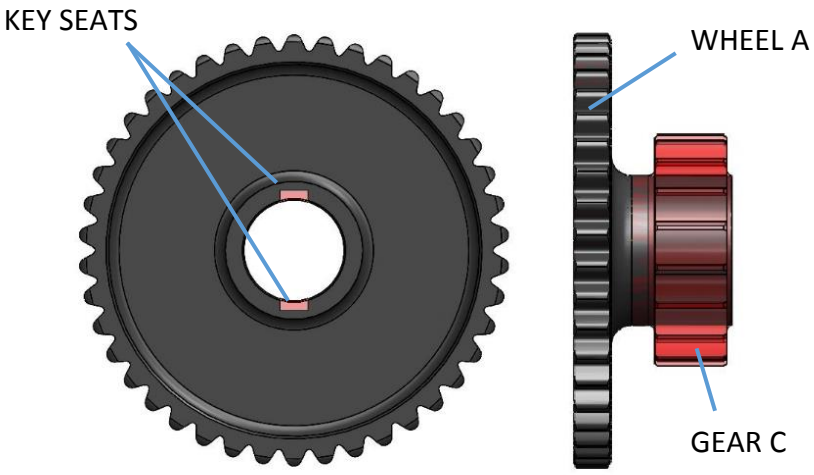

Figure 4.12. Chain upper wheel modification.

In Figure 4.12 the specific modifications applied on the wheel are highlighted in red. In particular, two diametrically opposed keyway have been considered due to balancing reasons. Moreover, the original wheel also embodies the teeth of gear C (Figure 4.11 and Figure 4.12) which no more engages the gears B. Consequently, this part can be removed in order to reduce the weight of the component and the rotating inertia of the EM rotating parts. In fact, the rotating inertia of these components is important for the *powerunit* performance analyses [53]. Moreover, the rotating inertia also affect the loads acting on the transmission chain (see section 6.1).

The ICE presents a maximum rotating speed (limiter) of 12000 rpm (see Figure 4.4) so the maximum speed allowed to the electric motor has been properly defined. In particular:

$$n_{EM} = \frac{n_{ICE}}{\tau_{chain}} = \frac{12000}{1.20} = 10000\ [\text{rpm}] \qquad (4.2)$$

where n_{ICE} is the maximum speed of the internal combustion engine and n_{EM} is the speed that the electric motor should not exceed. In fact, the characteristic of the EM presents a speed range varying up to 10000 rpm (Figure 4.10).

The drive is finally carried out by a silent type chain. A silent chain is an assembly of gear racks consisting of two teeth each. This kind of chain can operate at high speeds transmitting high loads and ensuring noise reduction

[54]. Compared with roller chain, because of the advantages in high durability, high transmission efficiency and low noise, silent chain is recently getting more widely used [55].

The analysis of the loads derived from the original *desmodromic* actuation and the maximum load declared by the chain manufacturer are considered in order to assess the possibility to employ the original chain for the connection between the electric motor and the crankshaft. In particular, a specific structural analysis has been performed considering the dynamic behaviour of the whole transmission system in order to assess the use of the OEM chain (described in the section 6).

Another important component involved in the torque transmission mechanism is the electric motor shaft. It has to fit with the EM rotor and has to be supported by the EM housing. During the design process proper bearings have been chosen considering the maximum rotating speed and the operating loads. Figure 4.13 shows a section of the assembly of the EM where the shaft, the stator, the rotor and all the other functional components are depicted.

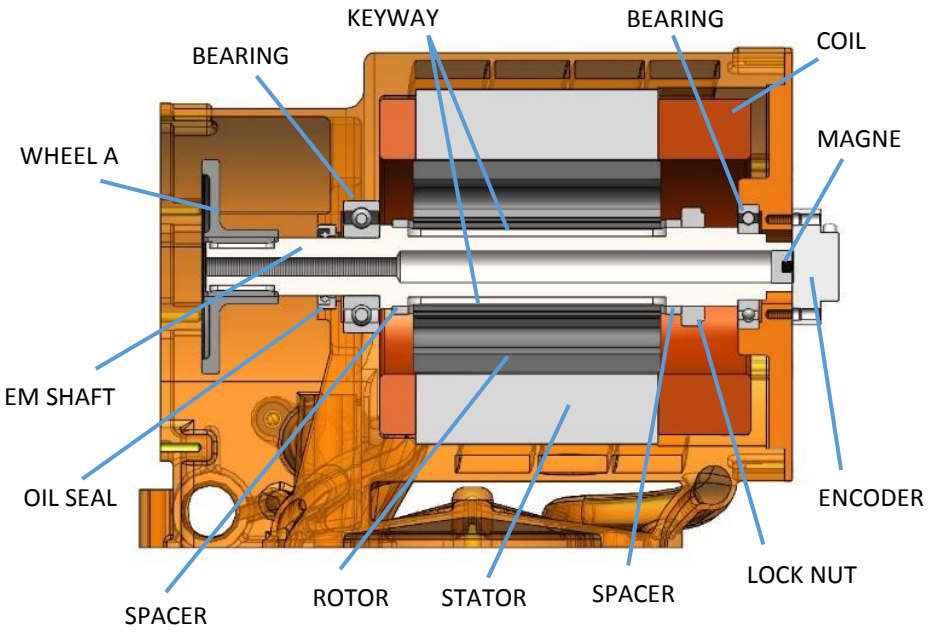

Figure 4.13. EM assembly section.

The position of the oil seal is chosen in order to keep clean the EM room isolating the volume of the engine carter. On the opposite side an encoder sensor is located able to precisely scan the rotating motion. To do so, a magnetic actuator is applied on the shaft end through a special adapter. The rotor is blended to the shaft through two keyways arranged diametrically opposite in order to avoid the arising of unbalanced forces. Finally, the shaft presents a through hole introduced to reduce shaft mass and rotating inertia.

4.5 EM HOUSING

In this section all the steps needed to define the final geometry for the custom electric motor housing are described. First, it has been necessary to identify the constraints that the component has to follow in order fit to the engine block. The *Ducati Panigale* engine is featured by a closed deck configuration. Figure 4.14 shows the top view of the engine deck interface where it is possible to identify both cooling circuit and lubrication system ports.

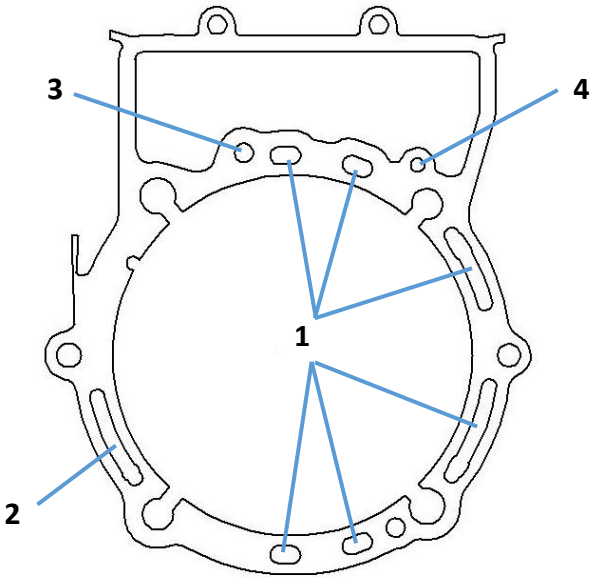

Figure 4.14. Engine deck interface.

Reference 1 indicates most of the engine cooling circuit outputs from the deck. These ports have been intercepted in order to make the coolant pass through the EM cooling circuit. Reference 2 represents another cooling port which has not been used for this application.

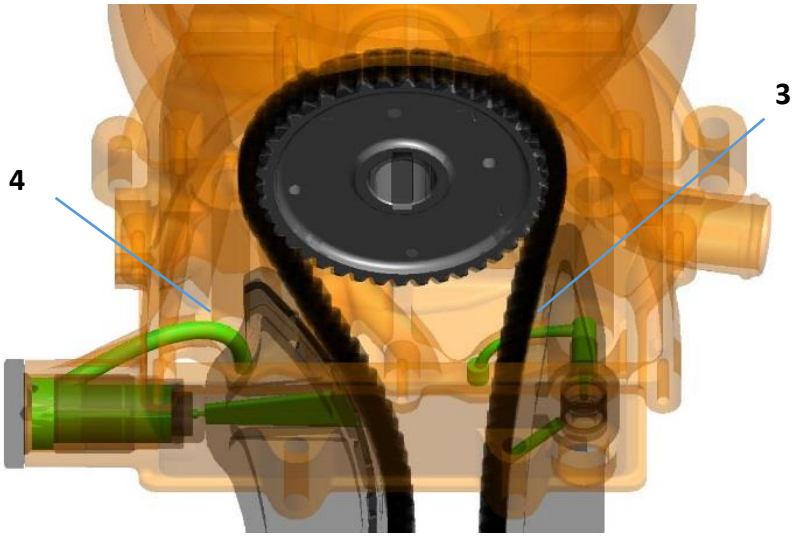

Figure 4.15. Oil channel details: feedings of chain guide rails and chain tensioner.

References 3 and 4 indicate the oil channels that come up from the lubrication system. In particular, channel 3 feeds oil to the standing timing chain guide rail while channel 4 feeds the chain tensioner. In Figure 4.15 the oil path from ports 3 and 4 to each guide rail is shown in green. This oil feeding is very important because of the choice to keep the original timing chain as a transmission chain. About that, the position of the chain upper wheel is maintained, and so the position of the chain guide rails (Figure 4.16).

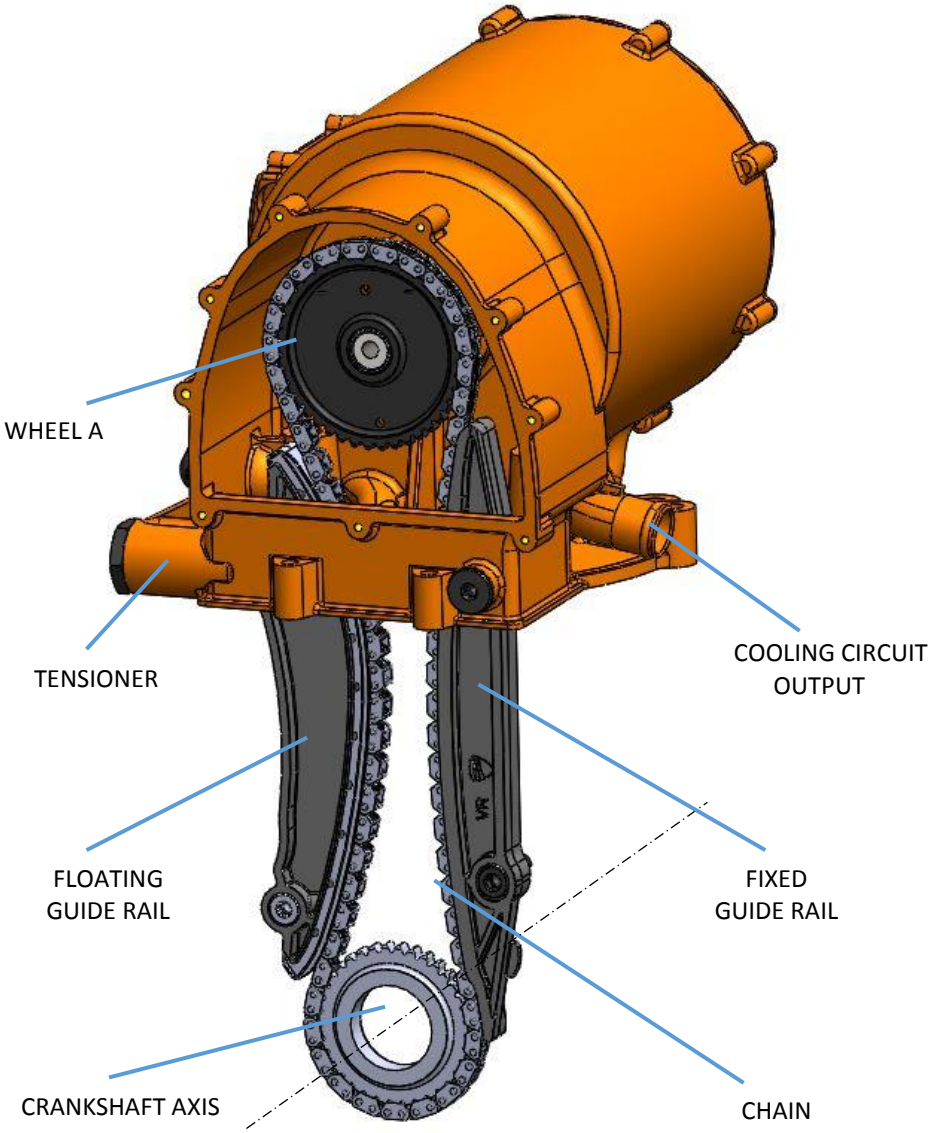

Figure 4.16. Electric motor housing layout.

Another important constraint to be respected is the position of the cooling circuit output (Figure 4.16). By this way it is possible to easily fit the original cooling lines coming from the ICE block. More details about the whole cooling system layout are shown in a following specific section.

4.5.1 Piston

The crank mechanism is the same of the stock ICE, choice better explained in section 5. The compression ratio considering the original combustion chamber volume is equal to 12.6:1, see Table 1. However, the combustion chamber is not present anymore because the ICE head has been replaced by the EM housing. A similar chamber has been included in the EM case design in order to accommodate the upper part of the piston top. The aim is to increase the volume of the resulting chamber in order to reduce the compression ratio, thus reducing the pumping losses.

Moreover, the piston has been modified in order to reduce its compression capabilities trying to keep the original piston weight.

Figure 4.17. Piston top holes machining detail.

In particular, for this application, several holes have been machined on the piston top in order to further reduce the drag effects. The final geometry of the "*fake*" piston is shown in Figure 4.17 (actually a pretty new piston design is ongoing). Reducing the compression force, also the thrust force exchanged between the piston and the liner is reduced and consequently the relative friction losses.

In Figure 4.18 is shown the assembly of the EM case with the liner and the upper part of the crank mechanism.

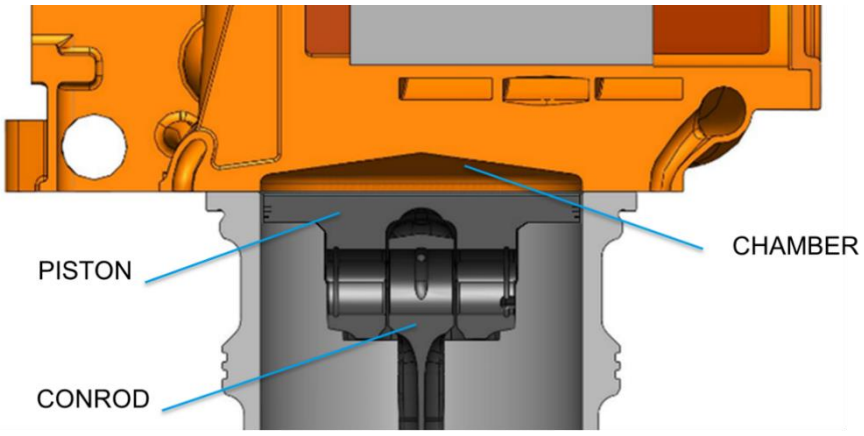

Figure 4.18. Assembly of the EM housing with the piston.

4.5.2 Positive crankcase ventilation

The ventilation of the crankcase is a very important aspect to be considered as it affects the transfer of air and oil mist across different areas of the engine crankcase. This phenomenon is increasingly important as engine speed increases, with a considerable impact on the parasitic losses. For this reason, the ICE presents a one-way valve that allows ventilation of the crankcase gases [56]. This *positive crankcase ventilation* (PCV) valve was originally located on the vertical head, onto the camshaft cover. Unfortunately, this is exactly the head that has been removed, so it has been necessary to provide an integration of the PCV valve in the EM housing (Figure 4.19).

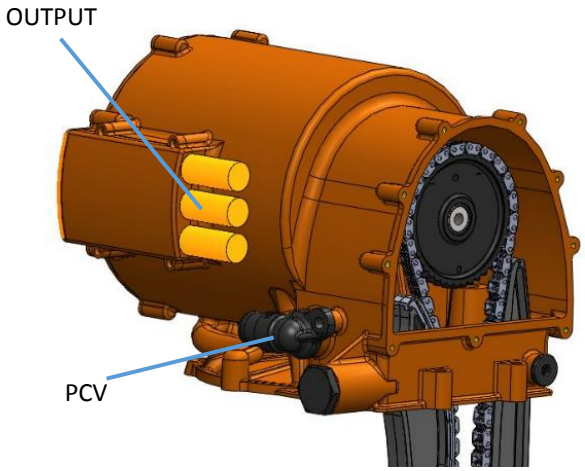

Figure 4.19. Side view of the assembly of the EM housing: detail of wiring output and PCV valve.

4.5.3 EM wiring

The stator of the EM is assembled into the housing through a press fitting process. After that, the wires coming from stator are lying down toward the side of the EM housing. Here is present a specific room which contains the welded portions with the output cables (Figure 4.19). Then, the coils of the stator are immersed in a special resin in order to ensure the electrical insulation and to improve the thermal conduction (Figure 4.20).

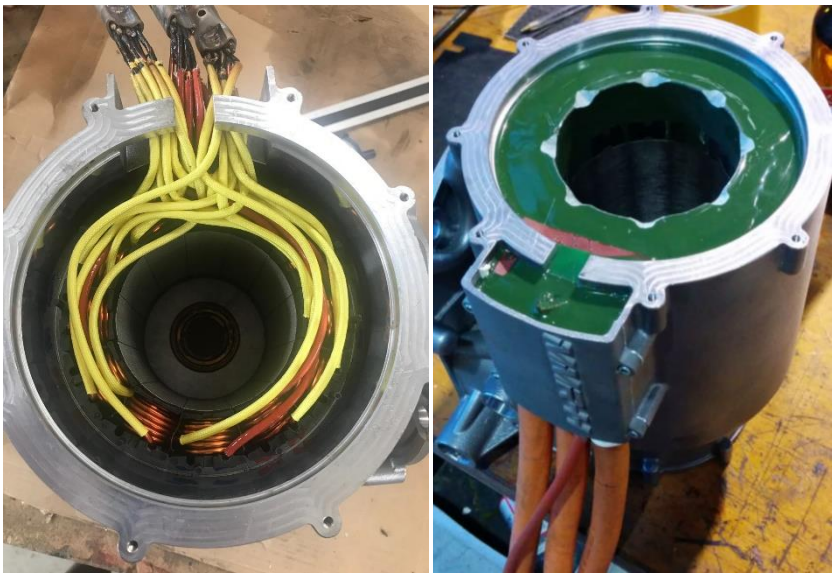

Figure 4.20. Wiring details before the resin deposit (on the left) and after (on the right).

Finally, the three wires corresponding to each phase of the motor come out from this room directly to the inverter along the minimum length path.

4.5.4 Manufacturing technology

The final geometry of the EM housing results to be very complex and consequently quite difficult to be produced via conventional technologies. In fact, the cooling circuit around the stator is realized in the same block. Similarly, the oil channels present a particular shape (see Figure 4.15) inaccessible by machining process.

For these reasons the component has been realized via Additive Manufacturing (AM) by Selective Laser Melting (SLM) technology. The material used for this application is the aluminium alloy AlSi10. Similarly, this technology has been also adopted to manufacture another components related to the same project as a new steel piston driven by topology optimizations [57,58].

SLM allows very complex details to be realized if suitable precautions are adopted. For example, some geometries can be built up only with proper support structures. These structures need to be accessible from outside in order to be easily removed after the manufacturing process. For these reasons, the component has been analysed through a manufacturing process simulation thus defining the position of the support structures. After this analysis, it has been necessary to modify some channels of the cooling circuit. In fact, the inner geometries have to be self-sustained because any support structures result to be inaccessible from outside. Consequently, the channel cross section has been modified considering a drop shape section which results self-sustained differently from a general circular section [59,60].

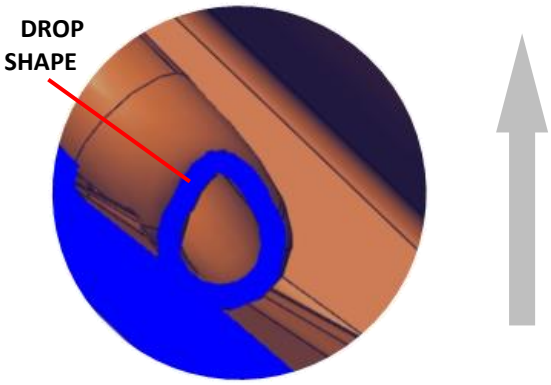

Figure 4.21. A channel cross section in correspondence with the drop shape: the arrow indicates the manufacturing growing direction.

In the Figure 4.21 is shown an example of the regions where the drop shape is required in order to allow the layer building process without support structures. The major axis of the drop shape has to be aligned with respect to the printing direction. The upper part of the drop shape presents a lower radius, thus does not need any support structure. Consequently, the part orientation had an important role during the AM process setup [61]. The orientation chosen for the part is about 44 degrees from the build plate as shown in the Figure 4.22 on the left. Similarly, the Figure 4.22 on the right shows the result of the printing process, including the support structures.

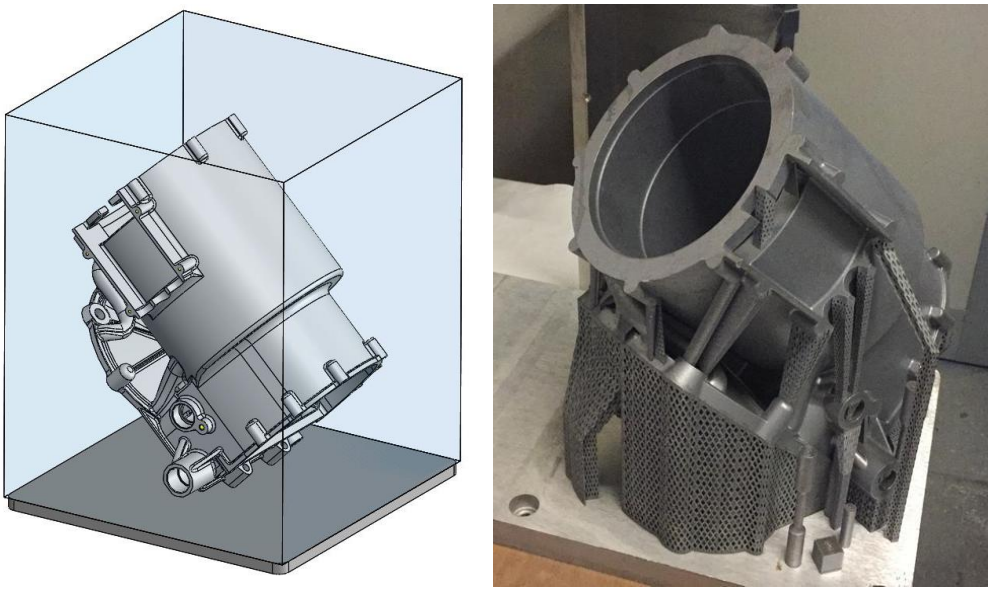

Figure 4.22. Fitting process of the part to the building volume with the proper orientation (on the left) and row part with the support structures after the printing process (on the right).

The final result of the AM process represents the raw component which has to be finished afterwards. Firstly, after the printing process the component needs to be cleaned up in order to correctly remove the powder exceeding. Secondly, the support structures can be carefully removed with specific tools. After that, the component has been subjected to a specific thermal treatment in order to restore and improve its mechanical properties. In fact, *AM*

techniques for metallic materials are characterized by extremely fast heating and cooling cycles, and as a consequence, metallic parts processed by AM are sensitive to the build-up of internal stresses [62]. A *design for manufacturing (DFM)* approach has been carried out in order to integrate manufacturability aspects during the design stage. In particular, both manufacturing process have been considered for the manufacturability evaluation, such as AM and machining [63]. In fact, several surfaces have to be machined in order to comply with the proper tolerances needed to ensure the optimal operation. Figure 4.23 highlights the parts subjected to machining process in which a suitable machining allowance has been considered in order to compensate for the distortions due to residual stresses derived from the spatially varied thermal cycles produced by the AM process. The residual stresses are associated with pronounced deformations especially for thin-walled features [64].

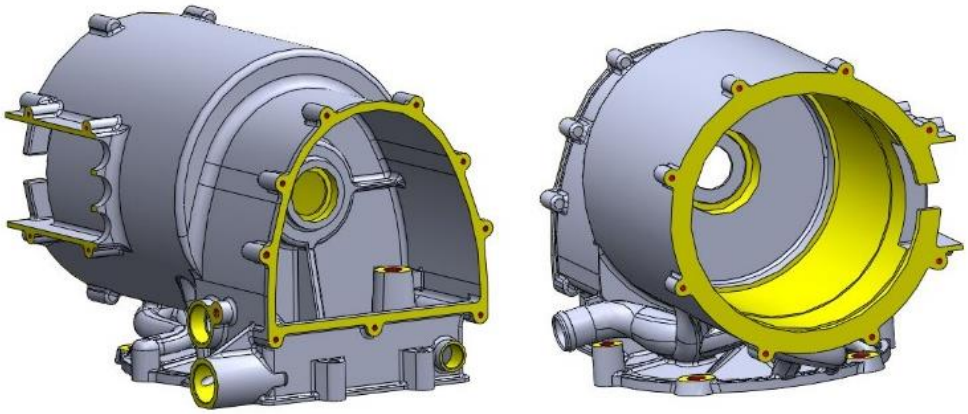

Figure 4.23. Machined surfaces for finishing process.

Finally, the Figure 4.24 shows the final product of the realized component after the printing and machining processes. The last step consists in the quality control process needed to assess the compliance of every dimension with respect to the specific tolerances.

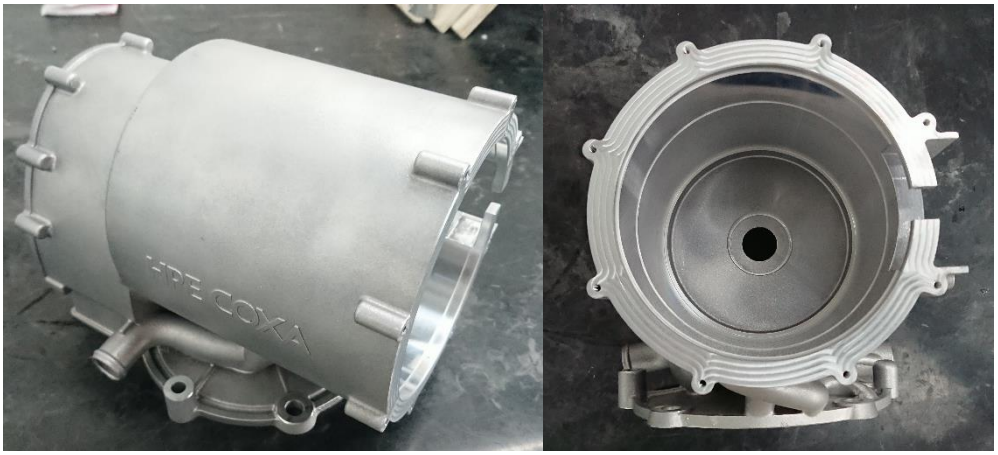

Figure 4.24. Final product of the EM case.

Material properties

The material adopted to manufacture the component is the aluminium alloy AlSi10. The mechanical properties of this material are strictly affected by the manufacturing process, inducing in the part several uncertainties. For these reasons, a wide experimental campaign has been carried out in order to determine the actual mechanical properties of the material adopted. To do so, several specimens of the same alloy have been produced by additive manufacturing and consequently tested.

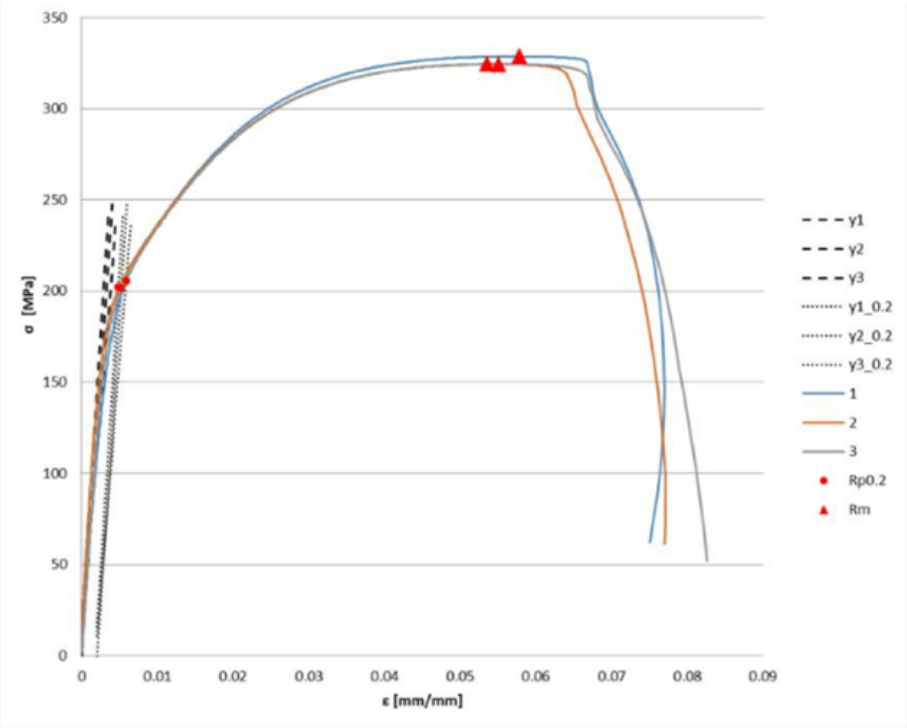

Figure 4.25. Mechanical properties of the AlSi10 alloy determined on additive manufacturing specimens.

In Figure 4.25 are shown the strain-stress curve referred to some specimens. In particular, the results show a good repeatability of the experimental tests.

4.5.5 Powerunit assembly

After the quality check, it is possible to proceed assembling the EM components. One of the bearing has been mounted before the stator in order to have easy access, while the other bearing is located on the cover on the opposite side (see Figure 4.13 on the right). Subsequently, the EM stator has been carefully press fitted in the specific housing including the wiring before applying the mentioned resin. Finally, the EM shaft has been previously assembled to the rotor and then inserted in the EM housing (see Figure 4.13).

Finally, the electric motor can be mounted onto the engine assembling the complete *powerunit*, shown in Figure 4.26.

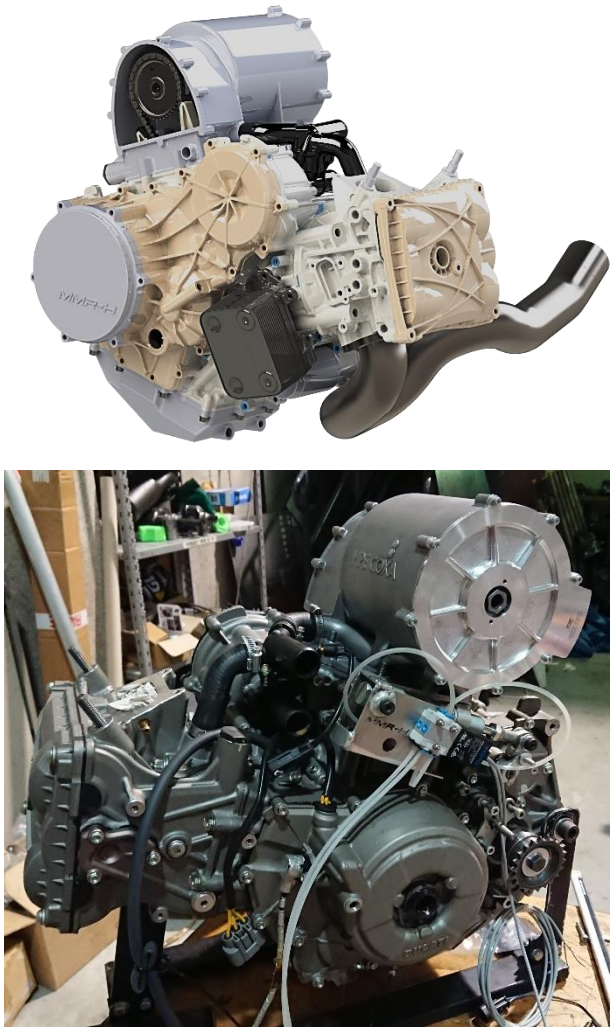

Figure 4.26. Assembly of the complete powerunit.

4.6 COOLING SYSTEM ANALYSIS

The cooling of an electric motor is very important because it strictly affects the EM efficiency. In fact, *there should be a strong interaction between the electromagnetic and thermal designs as it is impossible to accurately analyse one without the other, (i.e. the losses are critically dependent upon the temperature and vice versa)* [65]. Generally, an electric motor provide about 60% of total energy conversion from electric form to mechanical form [66].

For this reason, a dedicated cooling circuit should be realized in order to keep the temperature of the EM as low as possible. However, it means to consider separate cooling lines, radiators and pump, with respect to the ICE system [67], causing an increase of weight and costs. Furthermore, in this project a *plug&go* solution is considered aiming to replace the minimum number of components. Consequently, the original engine system has been investigated in order to directly connect the EM cooling circuit. In particular, the water pump body is incorporated in the engine block through which it is connected directly to the cylinders. From there, the coolant rises in the head and in the EM cooling circuit, as shown in the diagram of Figure 4.27. The black lines represent the channels inside the engine block, while the blue lines represent the external circuit hose up to the radiator.

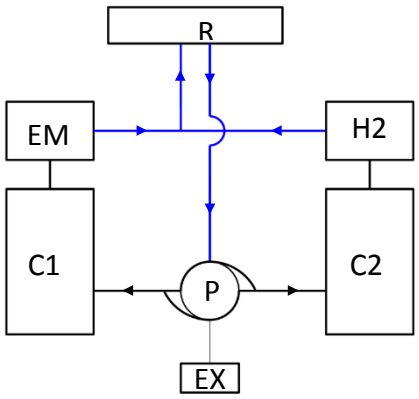

Figure 4.27. Cooling system layout: water pump (P); cylinder 1 (C1); cylinder 2 (C2); electric motor (EM); head 2 (H2); cooling radiator (R); water/oil heat exchanger (EX).

The outlets from the head and the EM are jointed together towards the cooling radiator, situated in the side pod of the vehicle. Consequently, the two circuits result to be connected in parallel. The fluid employed for the cooling system is distilled water since Formula SAE rules expressly prohibits the use of additives [9].

An important aspect of this study is to define the proper geometry of the whole EM cooling system in order to comply the following requirements:

1. Firstly, the characteristic of EM cooling circuit has to be defined such as to keep the original circuit balance ensuring the same flow rate to the ICE head;

2. Secondly, the particular geometry analysed has to maximize the heat transfer between the wall of the EM case and the fluid.

To achieve such results, a comparison between several geometries has been performed in order to find out the best solution. All these solutions have to respect the same constraints. In particular, both inlets and outlet have to be kept in the same position, as discussed above. In Figure 4.14, reference 1 indicates the inlet ports from the ICE cylinder. These ports could be jointed in a single inlet or kept separated in parallel circuit around the EM. Each path has to cover the maximum surface around the stator in order to ensure the largest amount of direct heat removing.

4.7 CFD ANALYSIS

Several geometries of the cooling circuit around the EM have been designed and analysed. However, for the sake of brevity, just two of them are presented hereafter:

- *Geom. 1*: the configuration causing the highest pressure drop;
- *Geom. 2*: the most permeable one.

In particular, as for the first, only a double-inlet design is analysed while, referring to the second, two different variants are proposed, one characterized by a unique intake (Geom. 2a) and one with a double inlet (Geom. 2b). Investigated geometries, as well as the original one, are shown in Figure 4.28.

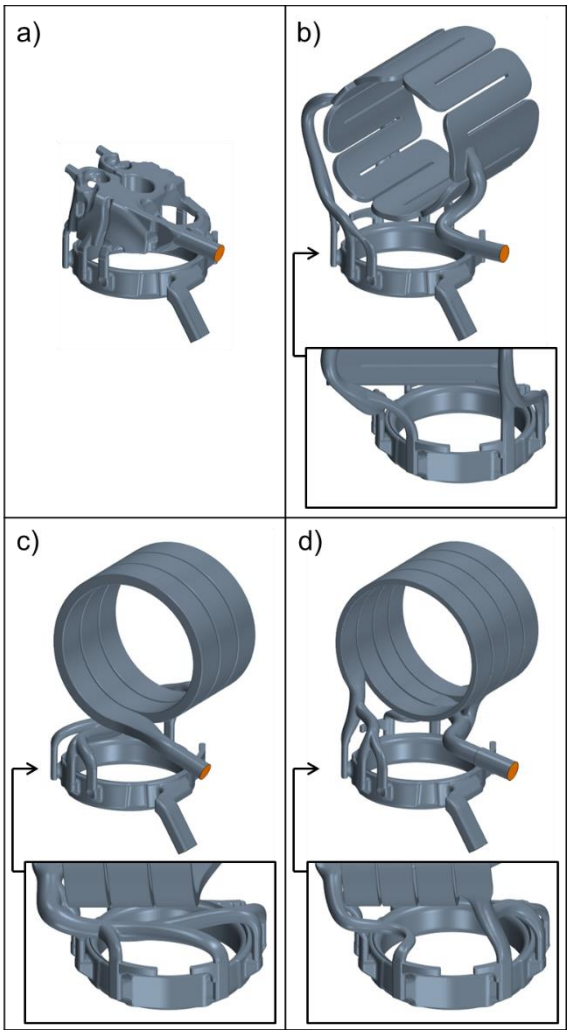

Figure 4.28. a) Original Geometry, b) Geom. 1, c) Geom. 2a, d) Geom. 2b.

4.7.1 Numerical Set-up

3D-CFD simulations of the coolant circuit have been carried out by means of a diffused commercial code for industrial applications, namely STAR-CCM+, licensed by Siemens PLM. Numerical analyses are steady-state and turbulence is fully modeled through a RANS approach. In particular, the two-equations k-ω SST turbulence model proposed by Menter [68] has been preferred, as particularly suitable for heat transfer problems with complex geometries [69]. Regarding the near-wall region, an "all y+" approach has been adopted, capable to provide a proper estimation of both wall shear stresses and wall heat fluxes regardless the particular y+ value [70,71]. In fact, on one hand the dimensionless distance can be hardly kept higher than 30 in the whole domain, as required by a high-Reynolds approach. On the other hand, y+ values lower than 3 as prescribed by a low-Reynolds approach would require a very thin near-wall grid with multiple layers, characterized by a huge number of cells and high computational costs. The adopted "all y+" model is based on a low-Reynolds version of the k-ω SST turbulence model and blended expressions for the wall laws, i.e. both velocity and thermal wall functions are merged with their respective "exact" expressions adopted in the viscous sub-layer.

Coolant consists of pure water, whose properties have been derived from NIST database. Since temperature variations are modest, it has been modeled as a constant density fluid and molecular viscosity, specific heat and thermal conductivity have been assumed constant too. As shown in previous analyses on a similar engine [72,73], boiling is a negligible phenomenon, and therefore it has not been modeled to save computational cost. Moreover, note that the heat flux to be removed from the electric motor is definitely lower than the heat flux to be removed from the original ICE head.

As for boundary conditions, a mass flow rate and a fixed pressure have been imposed at inlet and outlet respectively, whose values have been inherited from the actual peak-power operating condition of the engine which is the most critical condition from a thermal point of view and, hence, the most interesting one to be analyzed. Walls have been modeled as non-slip smooth boundaries with a fixed temperature.

4.7.2 Results

Selection of the best designed configurations among the investigated ones is based on two simultaneous criteria: it is necessary to promote heat removal from the EM without penalizing cooling of the ICE. Since coolant path is remarkably longer with the introduction of the EM (as visible in Figure 4.28), preliminary simulations highlighted a non-negligible reduction of the circuit permeability. As a consequence, all the investigated designs are characterized by fully-open passages of the gasket between block and head. Figure 4.29 shows pressure drops generated by the investigated geometries on the same imposed mass flow rate, equal to 100 l/min (similar to the actual one at peak-power condition). Dashed line highlights the resistance offered by the original circuit (w/o EM). Despite the effective cooling capabilities (as able to fully cover EM along its axis), Geom. 1 offers an abnormal resistance to the flow because of the continuous motion reversals along the EM axis, leading to a relevantly high pressure drop. On the contrary, both Geom. 2a and Geom. 2b promote flow reducing losses if compared to the original geometry.

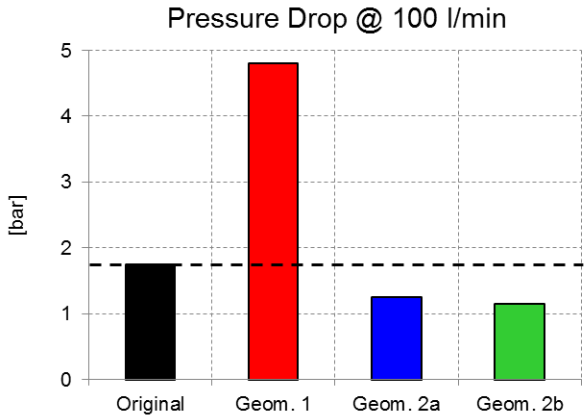

Figure 4.29. Pressure drops caused by investigated geometries for a mass flow rate of 100 l/min.

All the other geometries omitted in the present manuscript are characterized by high pressure drops, closer to Geom. 1. As a consequence, Geom. 2a and 2b have been preferred for the final solution. Last decision regarded the choice between one and two inlets to the EM circuit. Since pressure drops produced by Geom. 2a and Geom. 2b are very similar, decision was based on the effectiveness of the heat removal by the water jacket.

As heat transfer is strictly dependent on flow velocity, before any consideration on thermal aspects, the actual flow rate is required. In order to obtain the real flow rate, characteristic curves of circuit and pump have to be compared in a prevalence-mass flow chart. At this point it is useful to remember that in such a coolant circuit, characterized by two parallel branches as visible in Figure 4.27, features and principles of parallel circuits are valid. From a practical point of view this means that the characteristic of a single branch can be directly compared to the pump curve to obtain the flow rate of that specific branch or, even, in case of two symmetric branches, if the curve of a branch is known, the characteristic of the whole coolant circuit is easily extrapolated considering, for a given prevalence, a double flow rate. For example, in Figure 4.30 different characteristics are reported. The red line represents the pump curve. Lines with crosses depict the original coolant jacket. In particular the black curve represents a single branch, while the blue one the whole circuit. The latter is obtained from the first, doubling flow rate for a given gH.

As pressure drops of Geom. 2a and 2b are very similar, differences in terms of flow rate are negligible. Therefore, for the sake of brevity, only characteristic of Geom. 2b is considered in the graph. As known, intersection point represents the actual operating point of the coolant circuit and, on x-axis, flow rate corresponding to such condition can be inferred. It is useful to point out that the characteristic curve of the pump reported in Figure 4.30 corresponds to a revving speed of 8000 rpm, since engine speed at peak-power condition is 10500 rpm and transmission ratio between crankshaft and pump is nearly 0.75. Moreover, such curve is valid for a jacket (relative) pressurization equal to 1 bar, corresponding to the actual one in the engine. As for the characteristic curve of the coolant circuit, it is obtained considering the simplified equation of a parabola passing through the origin and symmetric with respect to the y-axis ($y = ax^2$). The unique parameter (a) of the equation is obtained considering that point with coordinates (100 l/min; 1.25 bar) has to be part of the curve. In order to double check the accuracy of the obtained characteristic, further simulations of the circuit have been carried out with a reduced flow rate equal to 40 l/min and 80 l/min. As visible, the parabola is close to the points which means that it faithfully represents pressure drop along the circuit for the different flow rates. Intersection point is located at a flow rate of nearly 134 l/min.

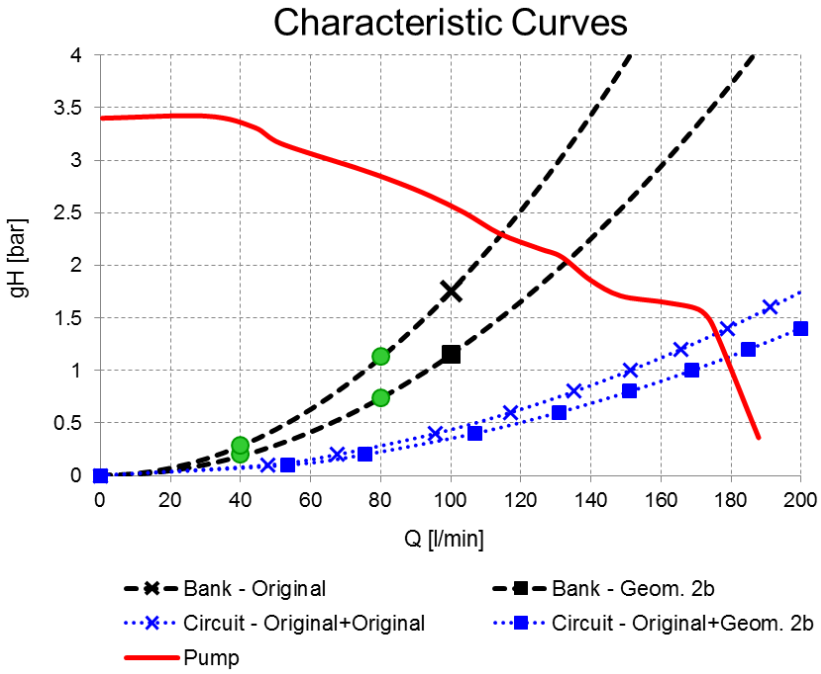

Figure 4.30. Characteristic curves of water circuit and pump.

Thanks to the estimated actual flow rate for Geom. 2b circuit, it has been possible to make some considerations on the heat removed by the coolant jacket. As reported in Figure 4.31, heat transfer between walls and coolant for Geom. 2a and 2b is similar, just a 5% gap is noticed. Nonetheless, looking at the local heat flux distribution reported in Figure 4.32, a non-negligible difference can be appreciated: double-inlet layout (Geom. 2b) is able to provide a more uniform spatial distribution. This in turn will lead to a quite uniform temperature of the solid, i.e. of the EM housing, as shown in the following section. With reference to the efficiency of the electric motor, for a given average temperature of the stator, a more uniform distribution has to be preferred. For this reasons, Geom. 2b can be recognized as the best solution compared to other designs.

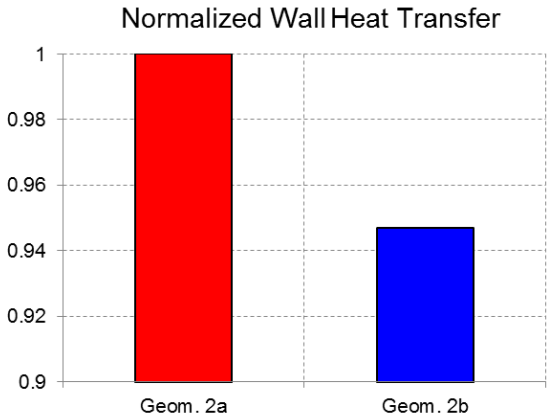

Figure 4.31. Normalized heat removed by the coolant circuit.

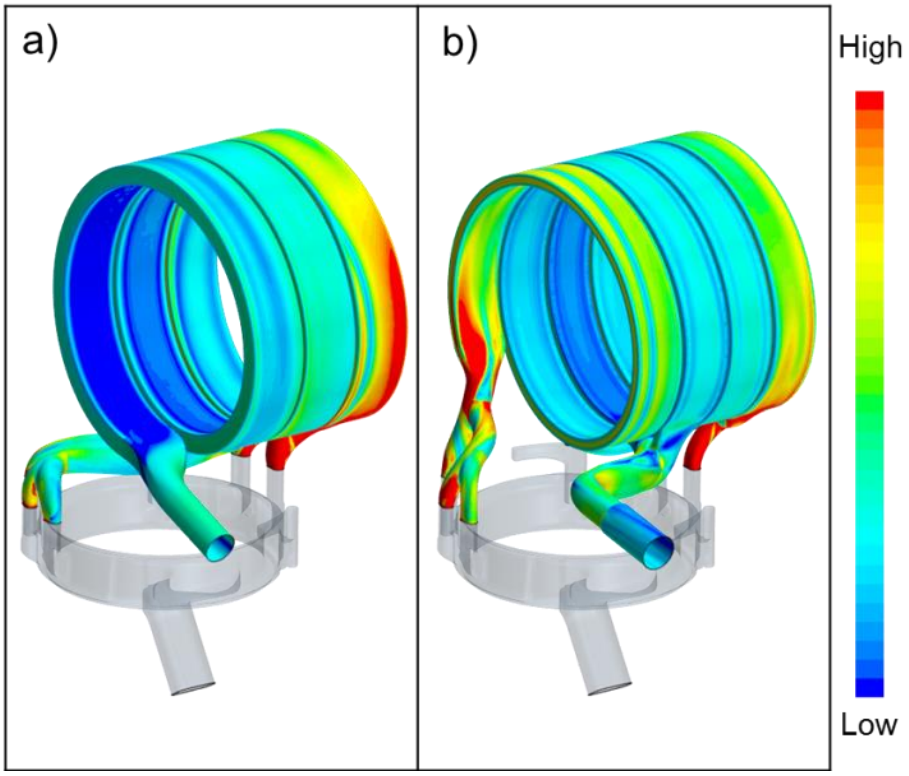

Figure 4.32. Local heat flux [W/m2] distribution through coolant jacket walls. a) Geom. 2a, b) Geom. 2b.

Last aspect to be investigated consists in the remaining difference, in terms of flow rate, between the original circuit and the selected one (Geom 2b). In fact, in Figure 4.30, the characteristic curve of the original coolant jacket of one bank (shown in Figure 4.28.a) is reported. The intersection with the pump curve provides the flow rate which is nearly 115 l/min. Therefore, as expected from the pressure drop analysis, Geom. 2b allows a higher flow rate (134 l/min), it being more permeable, compared to the Original one. This means that with respect to the original engine where, thanks to symmetry, flow rates (each one equal to 115 l/min) were perfectly balanced between the two banks, with the introduction of the EM and its respective coolant jacket (Geom. 2b) flow rates to the banks are not equal anymore.

Therefore, in order to reduce flow rate in Geom. 2b and restore balancing between banks, a redesign of the gasket holes was carried out. To save design time, an equal reduction of all the passages was considered. For the sake of brevity, only the optimized configuration is shown hereafter in Figure 4.33. For a flow rate of 100 l/min, the difference in terms of pressure drop between Original geometry and Geom. 2b with calibrated orifices is reduced to 1%, as visible in Figure 4.34.

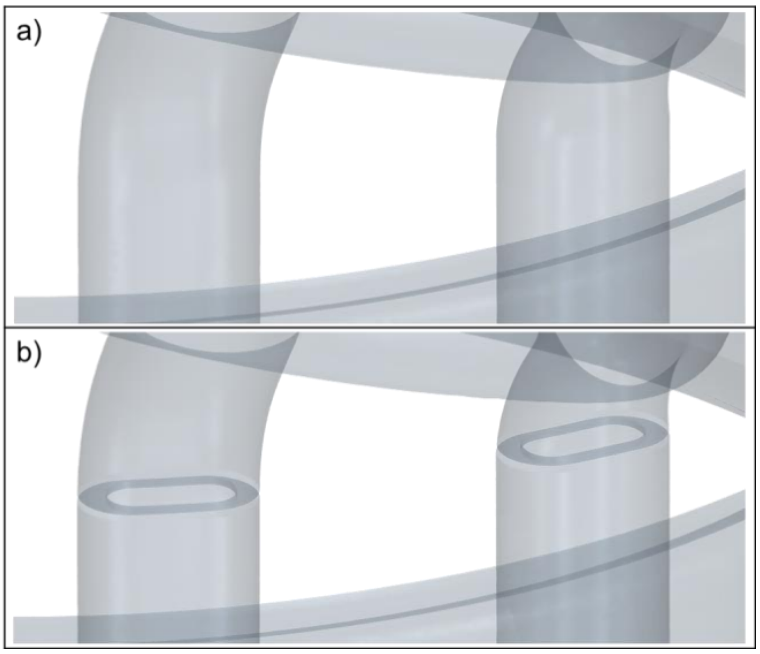

Figure 4.33. Gasket water passages of Geom. 2b. a) Starting configuration (fully-open passages), b) redesigned geometry (reduced orifices).

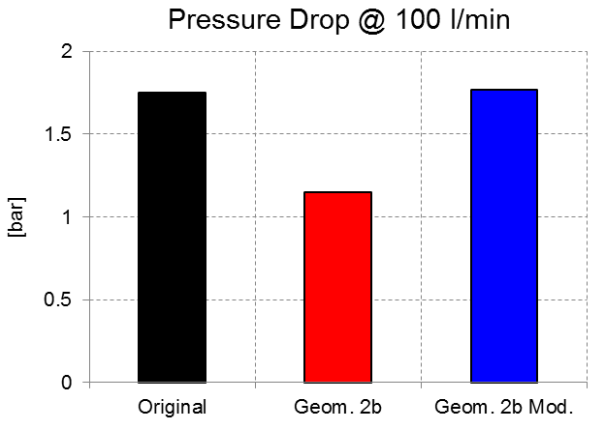

Figure 4.34. Pressure drops for different geometries with a mass flow rate of 100 l/min. Mod. stands for modified, i.e. gasket with calibrated water passages.

However, gasket optimization remained just a pure numerical exercise. In fact, despite the unbalance among the flow rates leads to a reduction of the pump efficiency, practically the initial layout without calibrated holes (Geom. 2b) was preferred in order to save costs and to promote efficiency of the EM. In particular, in Figure 4.29 characteristic curves of the entire circuits are reported with blue colour: crosses represent the original cooling circuit while squares the combined layout (original cooling jacket for ICE and Geom. 2b for the EM). As visible, this last configuration guarantees an intersection with the characteristic of the pump which takes place at a higher flow rate. The only drawback consists in the fact that moving towards higher flow rates, the efficiency of the pump decreases, i.e. off-design conditions are expected. That said, since the increase in terms of flow rate is moderate, the efficiency reduction is almost negligible. On the other hand, as anticipated above, tolerating a higher flow rate means costs reduction and increase of EM

efficiency. In fact, on the EM side, a higher mass flow leads to an improved cooling and, hence, to a higher efficiency. Finally, a cost reduction is ensured as gasket of Geom. 2b can be easily obtained from the original one, simply enlarging existing holes. On the contrary, gasket designed with calibrated water passages should be purposely manufactured.

Before conclusions on the CFD analysis, some remarks on both velocity and Turbulent Kinetic Energy (TKE) fields of the final geometry (Geom. 2b) are presented. Figure 4.35 reports velocity distribution focusing separately on the remaining portion of the original circuit (block cooling jacket) and on the designed coolant circuit of the EM. Despite the shape of the inlet from pump promotes flow on the left branch (Figure 4.35.b), velocity field in the EM jacket is uniform along the motor axis (Figure 4.35.a). Regarding TKE distribution, Figure 4.36 shows higher values at EM circuit inlets compared to rest of the body. This explains the slightly higher wall heat fluxes at electric motor coolant jacket inlets shown in Figure 4.32.b, as TKE strictly affects heat transfer.

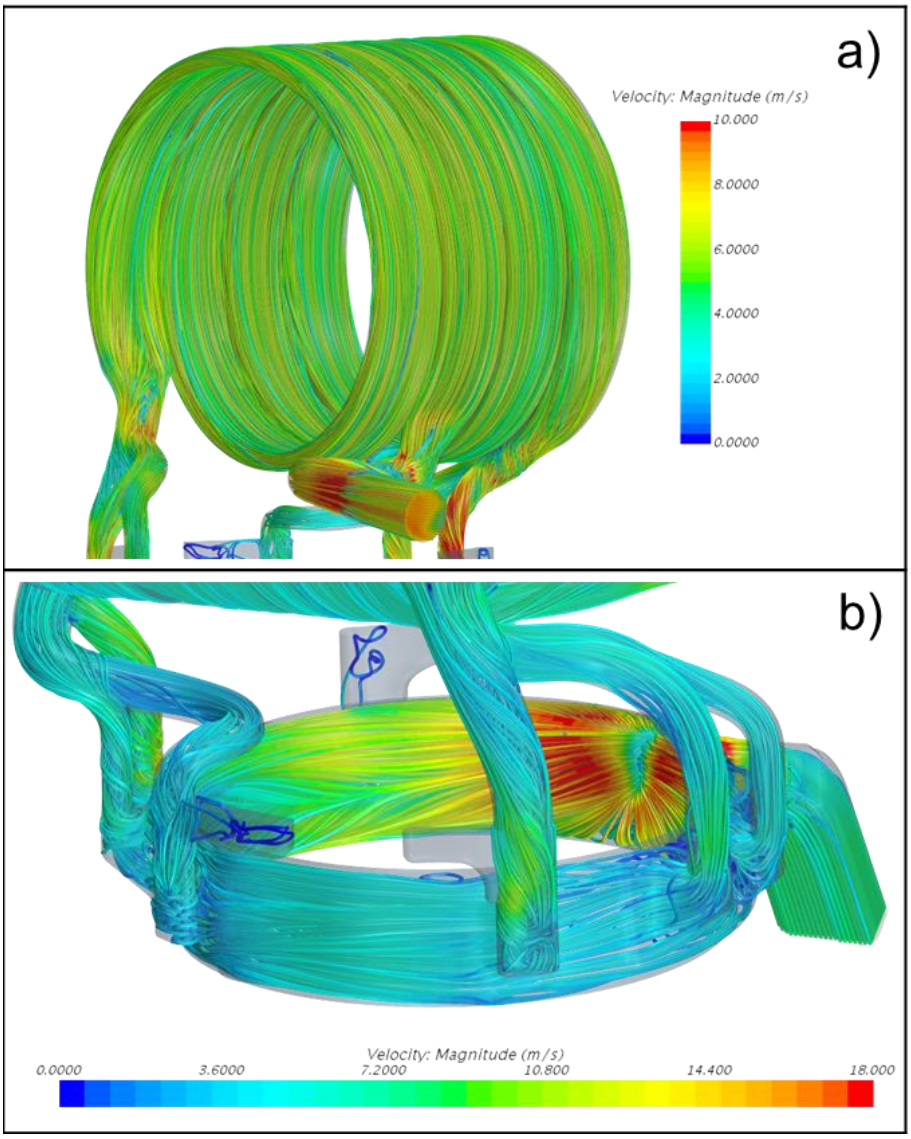

Figure 4.35. Velocity streamlines: a) engine block cooling jacket, b) electric motor cooling circuit.

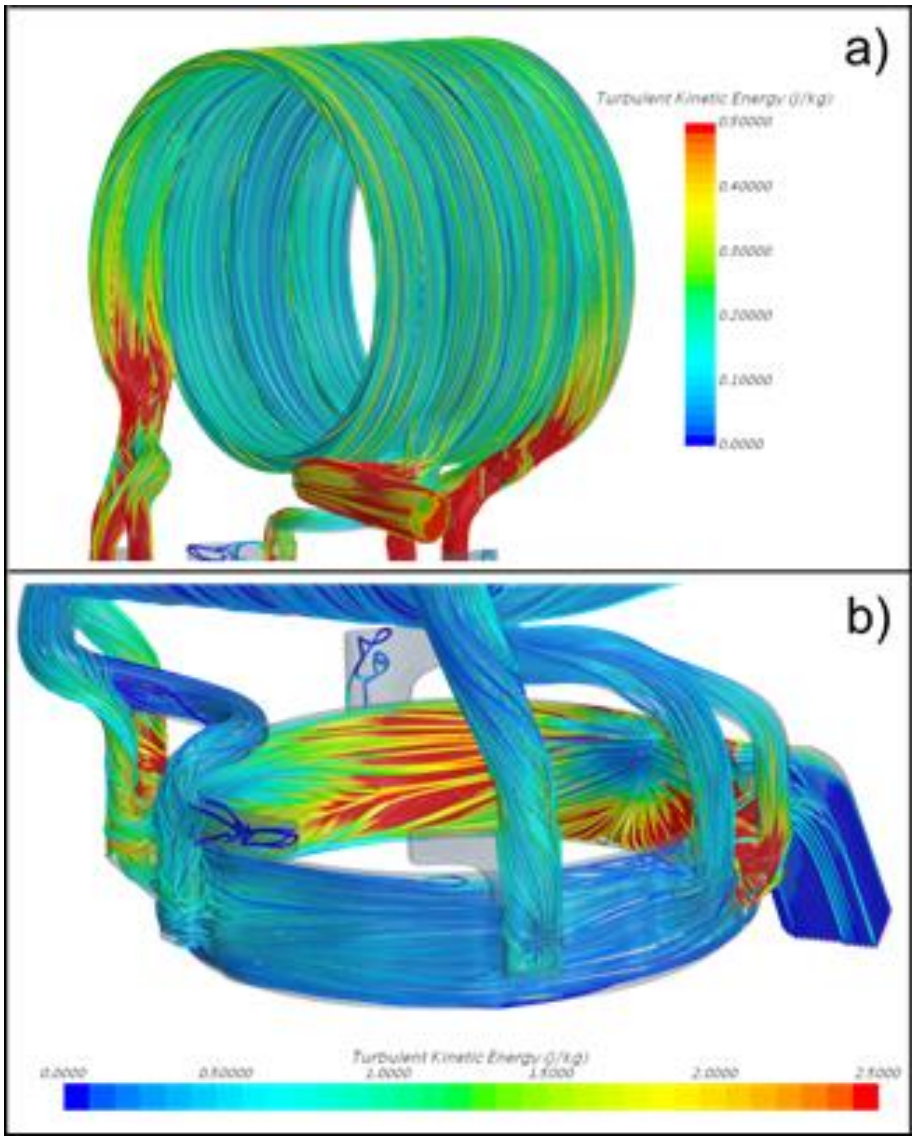

Figure 4.36. Turbulent Kinetic Energy (TKE) distribution: a) engine block cooling jacket, b) electric motor cooling circuit.

4.8 THERMO-STRUCTURAL ANALYSIS

This section focuses on the description of the FE model developed for the thermo-structural analysis of the EM case, Figure 4.37. In particular, first a thermal model has been prepared considering the EM case. In this model the HTCs derived from the previous described CFD simulations have been considered to compute a complete temperature field within the component. Then, these results have been set as a boundary condition in the mechanical model for the thermo-structural analysis.

In the following, the specific modelling parameters set for each different component are described:

1. *EM case*. This is the main component on which the analysis is focused on. It is made of aluminium, whose main characteristics are summarized in Table 5. The mesh of this component consists of about 316 thousand pentahedral elements (bilinear, 6 nodes, 6 Gaussian integration points) and 723 thousand tetrahedral elements (first order, 4 nodes, one Gaussian integration point). The average elements size is 2 mm while it is refined to 1 mm near the contact interaction zones. It is possible to identify several regions which are collected in different sets concerning each specific purpose. A first set is represented by the press fitting surface between the case and the stator. Similarly, the regions in correspondence of the bearing supports are collected as two different sets. The surface on the case base is also collected in a set useful to setup the contact between the engine deck and the case itself.

2. *EM shaft*. Actually, the shaft is not modelled but only the resulting loads have been considered. In particular, two forces corresponding to the chain reactions during the peak-torque transmission are applied in correspondence of the bearing supports.

3. *EM stator*. It is represented by a simplified bulk geometry. It has been considered as made of steel, Table 6. The mesh presents an average element size of 2 mm for a total of 130 thousand hexahedral elements (bilinear, 8 nodes, 8 Gaussian integration points).

4. *ICE block*. The original engine block consists of two banks while only the bank connected to the EM housing has been considered. To do so, the engine block has been cut sufficiently far from the area of interest in order to not affect the results. The mesh has an average element size of 4 mm while it is refined to 1 mm near the contact interaction zones for a total of 460 thousand tetrahedral elements. The surface in correspondence of the engine deck has been collected in a set, in order to setup the contact interaction between the EM case and the engine block.

5. *ICE liner*. Also the liner has been considered in the model because it affects the overall stiffness of the assembly. The mesh presents an average element size of 2 mm for a total of 70 thousand hexahedral elements and the material considered is a generic aluminium, Table 6. The regions collected in specific sets are the upper surface in contact with the EM case and the circumferential surfaces in correspondence of the interference fit with the engine block.

6. *Bolts*. The bolted connections have been taken into account to analyse the effect of the bolt tightening on the assembly. Eight bolts have been discretized for a total of 42 thousand hexahedral elements with an average size of 2 mm. The material employed is a generic steel, Table 6.

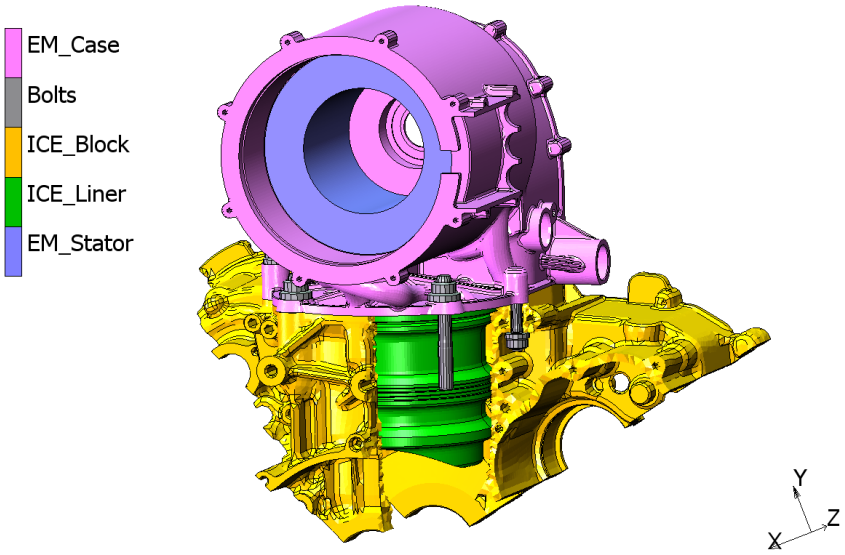

Figure 4.37. Finite Element model.

Steel	
Young modulus	210000MPa
Density	7.8 kg/dm^3
Poisson's ratio	0.3
Thermal conductivity	0.039 W/mmK
Thermal expansion	$1.21 \cdot 10^{-5}$ 1/K
Aluminum	
Young modulus	77000MPa
Density	2.8 kg/dm^3
Poisson's ratio	0.33
Thermal conductivity	0.17 W/mmK
Thermal expansion	$2.1 \cdot 10^{-5}$ 1/K

Table 6. Material data.

4.8.1 Thermal model

The thermal analysis described in the following focuses on the geometry of the EM case and takes into account the thermal flux entering from the EM stator. Consequently, different boundary conditions are applied in the model (Table 7), in particular:

1. Proper HTCs are applied to the external surfaces of the assembly in order to take into account the heat exchange between the case and the surrounding air.

2. The inner surface of the chain room and of the piston chamber are modelled in a similar manner. In fact, centrifuged oil mist is considered in both the chain room and piston chamber where the oil is splashed by the piston motion [74].

3. In the oil circuit the coefficients related to the specific oil flow are applied.

4. The cooling circuit incorporated in the case is flowed by the cooling water. Hence, proper HTCs are applied to the surfaces of the cooling circuit, based on 3D-CFD simulations presented in the previous section.

5. The main source of heat has been considered to be the one generated by the electric losses due to the specific EM efficiency and exchanged through the stator/case interaction. Then, the corresponding thermal heat flux has been applied to the inner surface of the EM case in correspondence of the interference fit interface.

External surface heat transfer	0.000015 $W/mm^2/K$
Splashed oil heat transfer	0.0003 $W/mm^2/K$ @120°C
Oil circuit heat transfer	0.0005 $W/mm^2/K$ @120°C
Water jacket heat transfer	HTC by 3D-CFD @ 90°C
Stator heat flux	0.0502 W/mm^2

Table 7. Thermal model boundary conditions.

Results

Figure 4.38 shows the resulting temperature field derived from the thermal model. A maximum temperature of about 115°C has been registered in correspondence of the chain room. This result is strictly influenced by the HTC and the corresponding reference temperature of the splashing oil. The temperature field of the cylindrical part of the case around the stator is nearly uniform, ranging from 90°C to 95°C, thus demonstrating that the water jacket efficiently absorbs the heat flux entering at the interface between the case and the stator.

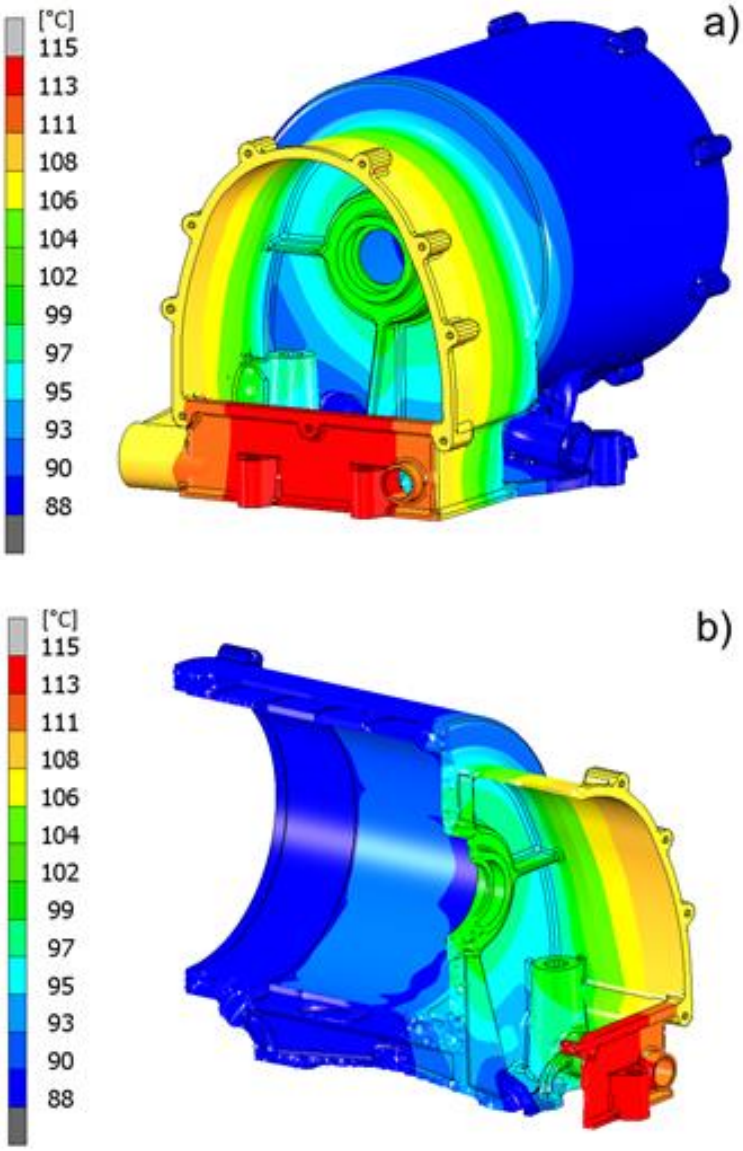

Figure 4.38. EM case temperature contour plot: a) chain room maximum temperature, b) EM housing inner temperature.

4.8.2 Thermo-structural model

Once the thermal analysis has been completed, a thermo-structural model has been prepared in order to assess the final strength of the EM housing. To do so, all the assembly components have been considered with the relative contact interactions.

The boundary conditions applied (Table 8) are described in the following:

1. The contact interaction between the stator and the EM case has been modelled taking into account a diametrical interference fit of 0.07 mm.

2. The EM torque is balanced by the stator and transmitted to the case thanks to the press fitting itself. Hence, the maximum EM torque is applied directly to the stator.

3. On the other side, the torque is balanced by the reaction of the chain which acts on both shaft supports. These forces have been evaluated considering the shaft as a simple beam with two supports, see Figure 4.39.

4. The EM case is coupled with the engine block through the original head studs. The contact interaction on the deck interface has been modelled considering the in-service stud tightening.

EM Stator - diametrical interference fit	0.07 mm
Maximum EM torque	102750 Nmm
Support 1 - external force	4000 N
Support 2 - external force	1000 N
Stud tightening	40 kN

Table 8. Thermo-structural model boundary conditions.

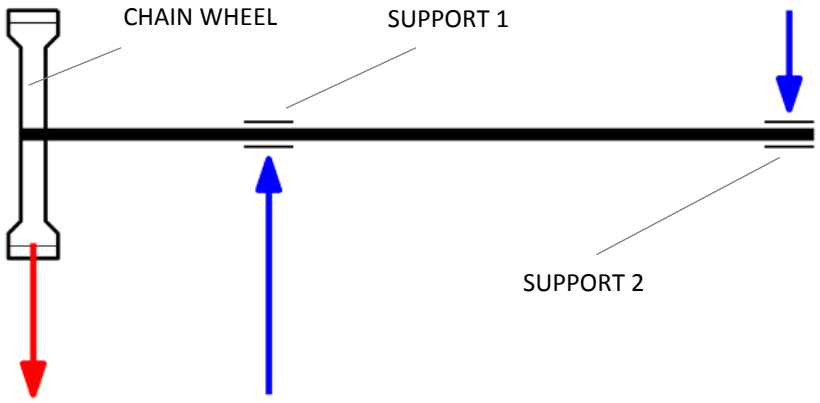

Figure 4.39. EM shaft loads.

Results

Figure 4.40 shows the von Mises stress contour plot of a longitudinal section of EM case. The maximum value of 135 MPa is registered on the bolt bosses. This value is below the yield strength limit of the material employed for the case manufacturing (205 MPa). High values of von Mises stress are also registered at the fillet radii between the vertical ribs of the motor cooling circuit and the inner surface of the EM case, and at the indenting extremities of the press-fit interface between the stator and the case, see Figure 4.40.b. These stress values are marginally influenced by the application of the motor torque and of the shaft reaction forces and they can be considered as nearly static stresses (related to stud tightening and stator press-fitting). As a consequence, since all the stresses are below yield strength limit of the material, the structural validation is fulfilled.

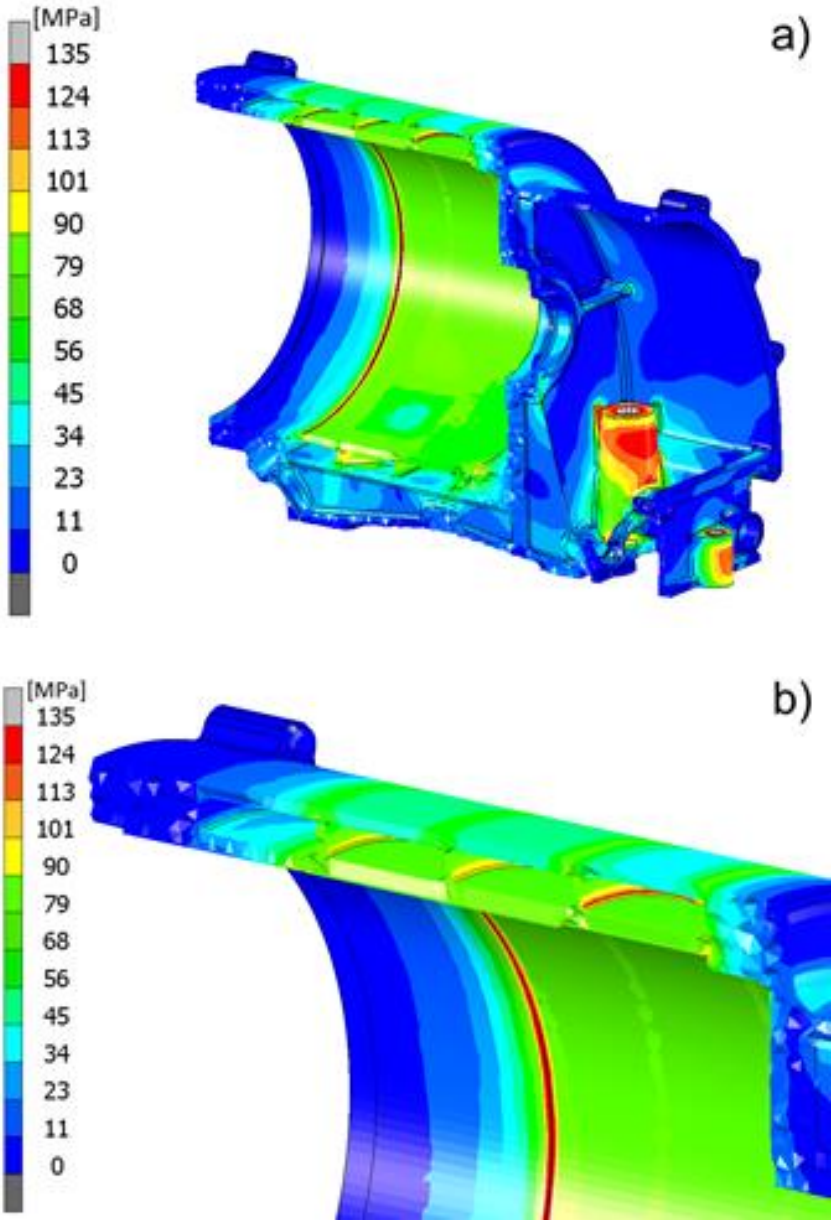

Figure 4.40. Von Mises stress contour plot: a) longitudinal section, b) cooling circuit and press fitting area detail.

4.8.3 Fatigue analysis

The previous results have been processed in order to evaluate the fatigue safety factors of the component. In particular, the *Dang Van* method has been considered based on a multi-axial criterion.

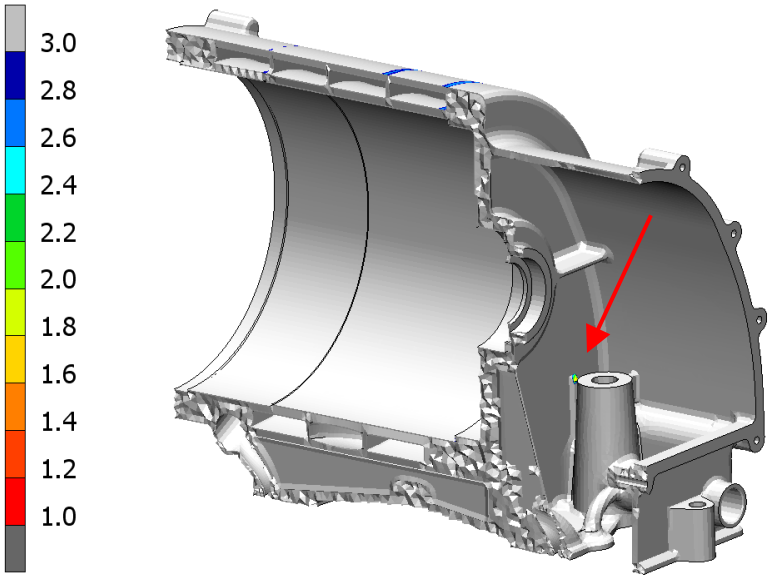

Figure 4.41. Fatigue safety factors contour plot.

Figure 4.41 shows the fatigue safety factors within the EM case. Globally, the component presents a fatigue safety factor greater than 3. However, a minimum value of about 1.8 is registered near the bolt bosses.

5 BALANCING SYSTEM

The problem of balancing the rotating and reciprocating components of the internal combustion engines has engaged the attention of engineers for many years with the result that a considerable literature is now available on this subject. Generally, the aim is to minimize external and internal forces in order to avoid excessive vibration of the engine and its surroundings as well as undesirable fluctuating loads on the engine and its mounting structure. Furthermore, an engine which is dynamically balanced is generally more silent and durable than one which is not [75].

The forces acting on the different components of the crank mechanism are usually divided in forces generated by the combustion of gases inside the combustion chamber (related to the instantaneous gas pressure value), and forces related to the inertia of the moving parts of the mechanism. The inertial forces can be subdivided in three categories related to the masses of the mechanism exhibiting:

- a purely reciprocating motion (*piston, piston pin and rings*);
- a purely rotating motion (*crankshaft*).
- a simultaneous reciprocating and rotating motion (*conrod*);

The reciprocating inertial forces exhibit a constant direction (cylinder axis) and an amplitude varying as a function of the crank angle (change in sign). The purely reciprocating masses, $\mathrm{m_{rec}}$, are the piston mass, piston pin mass and the elastic rings mass (compression rings and oil control rings). The reciprocating inertial force generated by these masses is equal to:

$$\mathrm{F_r}(\theta) = \mathrm{m_{rec}}\omega^2 \mathrm{r}\,(\cos\vartheta + \lambda\cos 2\vartheta) \qquad (5.1)$$

The crankshaft exhibits a pure rotating motion, so the rotating forces are constantly aligned with the crank throw direction. The rotating mass involved are the mass of the crank pin ($\mathrm{m_{cp}}$) and the mass of the counterweight ($\mathrm{m_{cw}}$). In particular, the centrifugal force is equal to:

$$\mathrm{F_c} = \omega^2 \mathrm{r}\,\mathrm{m_{cp}} + \omega^2 \mathrm{r_{cw}}\,2\mathrm{m_{cw}} \qquad (5.2)$$

where $\mathrm{r_{cw}}$ is the distance of the centre of gravity of the counterweight with respect to the crankshaft axis (Figure 5.1).

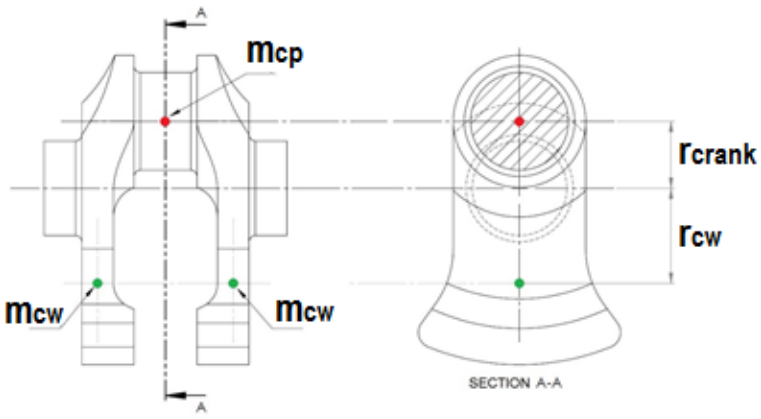

Figure 5.1. Crank throw rotating masses.

The connecting rod exhibits a simultaneous reciprocating/rotating motion. In fact, its upper portion (small end) is linked to the piston, thus possessing the same reciprocating motion. On the contrary, its lower part (big end) is linked to the crankpin, thus exhibiting a rotating motion. In order to evaluate forces related to the conrod motion a dynamically equivalent lumped parameter system of the conrod is usually derived [76,77], although other systems exist to separate the reciprocating mass and rotating mass of the conrod assembly [78]. In the particular case of the connecting rod (its motion is confined on a plane), the lumped parameter system is dynamically equivalent to the continuous body if the following three conditions are satisfied:

1. Conservation of mass conrod (m_c);
2. Conservation of the centre of gravity position (G_c);
3. Conservation of the moment of inertia aligned with the axis orthogonal to the conrod moving plane and passing through the centre of gravity (J_{Gz}).

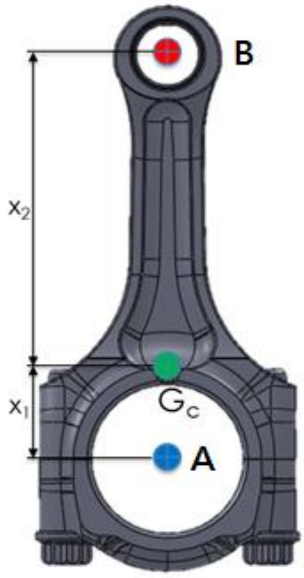

Figure 5.2. Dynamically equivalent lumped mass system of the conrod.

A system of equation can be defined in order to comply with these conditions:

$$\begin{cases} m_c = m_A + m_B + m_{Gc} \\ m_A x_1 = m_B x_2 \\ m_A {x_1}^2 + m_B {x_2}^2 = J_{Gz} \end{cases} \tag{5.3}$$

where m_A, m_B and m_{Gc} are the three lumped mass shown in the Figure 5.2. Unfortunately, only the kinematics of the points A and B are known. So, a different lumped parameter system can be defined by introducing a fictitious moment of inertia J'_{Gz}.

$$\begin{cases} m_c = m_A + m_B \\ m_A x_1 = m_B x_2 \\ m_A {x_1}^2 + m_B {x_2}^2 + J'_{Gz} = J_{Gz} \end{cases} \tag{5.4}$$

J'_{Gz} is necessary to guarantee the conservation of the actual moment of inertia of the original conrod and it has no physical meaning (it always has a negative value). Usually, reaction forces in A and B related to the fictitious moment of inertia J'_{Gz} are negligible with respect to the other inertial forces acting on the components of the crank mechanism. Therefore, the lumped parameter system can be approximated:

$$\begin{cases} m_A = \dfrac{m_c x_2}{x_1 + x_2} = \dfrac{m_c x_2}{L_c} \\ m_B = \dfrac{m_c x_1}{x_1 + x_2} = \dfrac{m_c x_1}{L_c} \end{cases} \tag{5.5}$$

For a typical conrod $x_1 < x_2$, as a consequence $m_A > m_B$. For the sake of clarity, m_A can be referred as the rotating portion of the conrod (m_{c_rot}) while m_B can be referred as the reciprocating portion of the conrod (m_{c_rec}). Definitely, it is possible to define the total reciprocating mass as the sum of the purely reciprocating mass and the reciprocating portion of the conrod:

$$m_{rec\_tot} = m_{rec} + m_{c\_rec} \tag{5.6}$$

Consequently, it is possible to evaluate the force related to the total reciprocating mass as follow:

$$F_{r\_tot}(\theta) = m_{rec\_tot}\omega^2 r(\cos\vartheta + \lambda\cos 2\vartheta) \tag{5.7}$$

where F_{r_tot} is the total reciprocating force. Similarly, the total centrifugal force depends on all the rotating masses, considering also the rotating portion if the conrod (m_{c_rot}):

$$F_{c\_tot} = \omega^2 r\, m_{cp} + \omega^2 r\, m_{c\_rot} + \omega^2 r_{cw}\, 2m_{cw} \tag{5.8}$$

In a single-cylinder piston engine, the balancing problem may be examined from two aspects: the purely rotating forces and the reciprocating forces. The rotating forces can be counteracted, providing space permits, by the introduction of balancing masses opposing the crank. The effects of the system of reciprocating forces on the global static balancing of an internal combustion

engine result more complicated to be determined. In fact, reciprocating forces exhibit a varying amplitude and a constant direction aligned with the cylinder axis (which is fixed while the crankshaft is rotating). As a consequence, they produce a system of forces which varies as a function of the crank angle (θ) and the evaluation of the existence of a natural global balancing is not straightforward (a different system of forces should be analysed for each single crank angle). In order to overcome this limit, each single reciprocating force is decomposed into an equivalent system of different centrifugal (counter rotating) forces which can be more easily analysed. In order to evaluate the global static balancing of the centrifugal forces in an internal combustion engine the so-called *forces star diagram* can be derived. In particular, a vector corresponding to each centrifugal force of each cylinder has to be drawn considering its proper direction. Then, all the vectors have to be collected at the same origin point (thus creating the star diagram) and the vector composition has to be performed. If the resultant vector is a null vector, a natural global static balancing exists.

Considering the reciprocating force related to a single crank mechanism and, in particular, considering the main harmonic contributions of first and second order:

It would be possible to decompose this force in the first two harmonic contribution:

$$F'_{r\_tot}(\theta) = m_{rec\_tot}\omega^2 r \cos\vartheta \tag{5.9}$$

$$F''_{r\_tot}(\theta) = m_{rec\_tot}\omega^2 r\lambda \cos 2\vartheta \tag{5.10}$$

Each single contribution (first and second order) can be decomposed in an equivalent system of counter rotating forces which can be immediately analysed in terms of global balancing in a similar manner as for the purely centrifugal forces. As an harmonic loading, the first (second) order contribution of the reciprocating force in crank mechanisms of an internal combustion engine is equivalent to the resultant force produced by two counter rotating (properly defined) masses, rotating with an angular velocity ω (2ω), at a certain distance to the rotation axis. For example, considering a mass distance from the rotation axis equal the crank radius (r) it is possible to derive an equivalent system as shown in Figure 5.3.

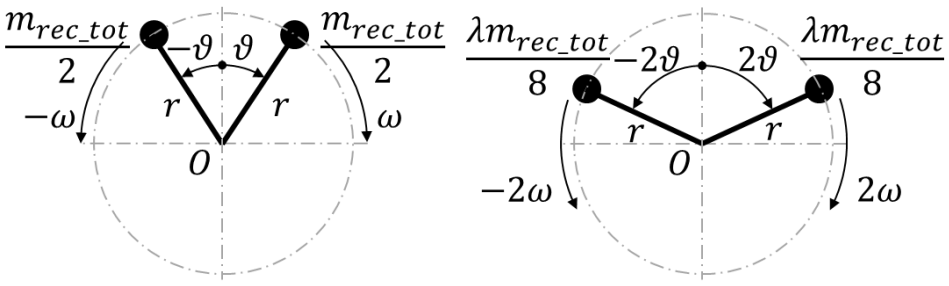

Figure 5.3. Equivalent system of masses rotating and counter rotating for the first (left) and the second order (right).

The *Ducati* engine subject of this study is a two-cylinder V-type engine, as described before. The resultant unbalance of the first order due to the reciprocating masses of the 90° V two-cylinder arrangement can be represented by a force, rotating in phase with the crank and in the same direction, and equal in magnitude to the maximum value of the inertia force of the first order due to the reciprocating masses of one cylinder. Therefore, it would be possible to balance the forces of the first order completely by attaching counterweights opposite the crank producing a force equal to that of the crank itself, the lower ends of the two connecting rods and the maximum value of the inertia force of the first order due to the reciprocating masses of one cylinder [79,80].

Once one of the engine heads has been removed, it has been necessary to restore the natural balance of the original engine. In fact, in a hybrid *powerunit* it is essential to minimize the sources of vibration [81] in order to not compromise the reliability of the different electric/electronic devices introduced [82]. Moreover, FSAE rules ask for the engine to be rigidly connected to the chassis thus amplifying the consequences of engine unbalancing [9].

5.1 UNCONVENTIONAL BALANCING SYSTEMS

Several unconventional balancing methods have been then investigated for the single cylinder engine balancing [83], capable to restore the balance of the first order reciprocating inertial forces. In the following different solutions found in the pertinent literature are described.

5.1.1 Yamaha T-max

The *Yamaha T-max* motorcycle is equipped with a two cylinder in-line engine with a total displacement of about 500 cc. This architecture presents the same balancing problems of a single cylinder engine, so it has been chosen as an example as well as because the overall dimension and weight are similar to the case of study of this treatise. Moreover, this engine presents a very particular balancing system. In fact, engine vibrations were offset not by a balance shaft but by reciprocating balancer, such as a third "*dummy*" piston driven from a central crankpin.

Figure 5.4. Yamaha T-max crank mechanism and balancing system.

The effectiveness of this solution is easy to understand. In fact, it consists of an additional crank mechanism of which the motion law is already known.

5.1.2 BMW F 800

This motorbike is equipped by a two cylinder in-line engine with a displacement of 798 cc. Also in this case the architecture is similar, concerning the small engines category and presenting the balancing problems of a single cylinder. In this case the reciprocating inertial forces are balanced by a particular mechanism, located in the middle of the crankshaft. In particular, it consists of an oscillating mass connected to the crankshaft by a specific conrod onto a dedicated crankpin. The kinematics of the mechanism make the balancing mass move in opposite direction with respect to the pistons.

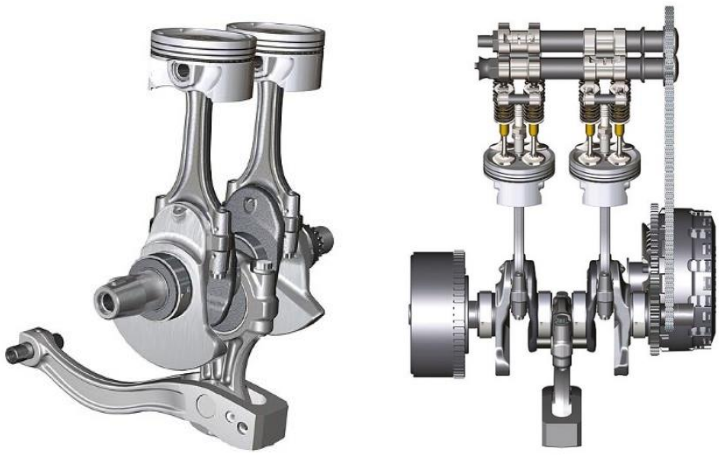

Figure 5.5. BMW F800 crank mechanism and balancing system.

The balancer mass is sized in order to generate an inertial force capable to balance the reciprocating inertial forces during the entire crank mechanism motion [84]. This solution guarantees low level of vibrations and above all it ensures low noise. In fact, no transmission devices are needed such as gears or chains, which usually determine characteristic noise (e.g. *rattle* and *whine* noise) [85,86].

5.1.3 Ducati SuperMono

The *Ducati Supermono* is ultra-rare and exclusive, thanks to its limited 67 model production run in the early 90s. Built for racing in the *Sound of Singles* series, the engine in the *Supermono* is a fuel-injected single-cylinder, Desmo DOHC, with the 550cc motor based off the cylinder head of the 888 model.

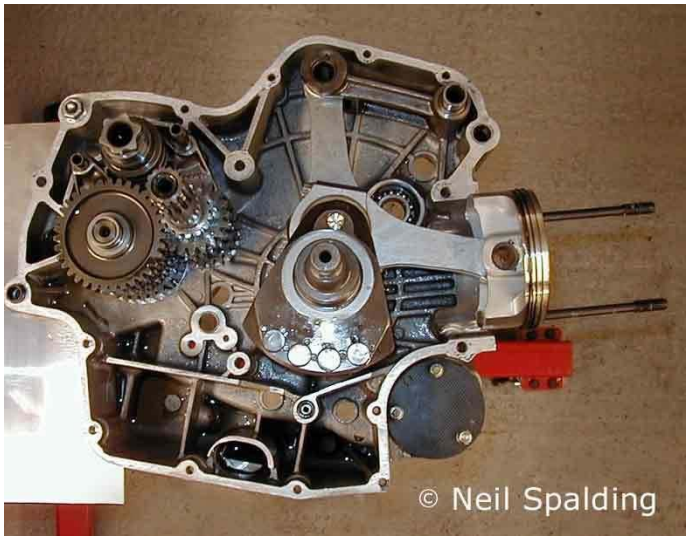

Figure 5.6. Ducati SuperMono crank mechanism and balancing system.

A dummy conrod has been left in place in order to balance the engine. It was attached to a weighted and pivoting bar, meaning that the *Supermono* presents perfect balance as the extra conrod moved up and down to overcome vibration issues, allowing the single cylinder engine to behave more like a twin cylinder engine at higher revs [87,88].

5.2 BALANCER ROD

After analysing several unconventional balancing systems, this section describes another particular configuration applied to the case of study of this project. In particular, the target is to restore the natural balancing of the original engine with respect to the first order inertial reciprocating forces. To do so, a balancing mechanism consisting of a balancer rod has been considered, similar to the *SuperMono* architecture. In particular, the piston has been replaced with a specific balancer rod, also named "*clapper"* for its oscillating motion.

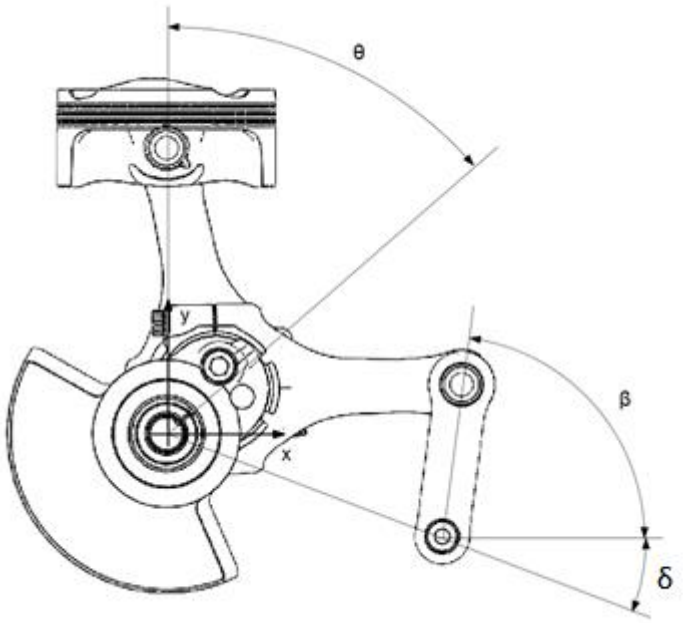

Figure 5.7. Crank mechanism and balancer rod.

Although this solution completely overturns the kinematics of the crank mechanism, actually the minimum number of components have been replaced, trying to obtain a *plu&go* solution. In fact, the same crankshaft and the same conrod are involved. Moreover, this solution allows to use also the same piston pin.

Firstly, it is necessary to define the kinematics of the mechanism obtained. The kinematics of the crank mechanism is already known (analysed previously in this section), while the other mechanism is composed by a planar articulated quadrilateral [89]. The members that compose the articulated quadrilateral are the crank throw (in green, Figure 5.8), the conrod (in red, Figure 5.8) and the balancer rod (in blue, Figure 5.8). The dimensions of the crank throw and the conrod are fixed because the components already exist. However, the geometry of the balancer rod has to be defined, as well as the position of the cylindrical joint axis with respect to the reference system (*O_bal* in Figure 5.8). The global reference system has the origin on the crankshaft axis, the x axis

oriented to the cylinder of the balancer rod and the y axis oriented to the cylinder of the crank mechanism (Figure 5.10).

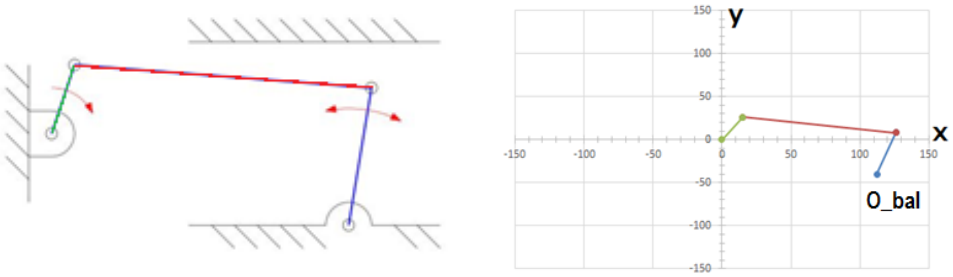

Figure 5.8. Articulated quadrilateral mechanism layout: crank throw in green; conrod in red; balancer rod in blue.

Definitely, the variables of the project are defined as follow:

- Position of the pivot with respect to the global reference system (x_{bal}, y_{bal} in Figure 5.10);
- Balancer rod length (L_{bal} in Figure 5.9);
- Balancer rod mass (m_{bal});
- Balancer rod inertia (J_{Gz_bal}), depending on the balancer shape;
- Centre of gravity position of the balancer rod with respect to a local reference system (g_{bal_x}, g_{bal_y} in Figure 5.9).

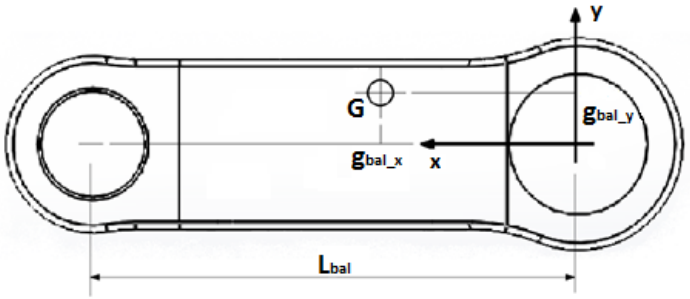

Figure 5.9. Balancer rod; generic position of the centre of gravity and length.

However, the balancer rod needs to be connected to the engine block by means of a pin constraint which represents the pivot of the rod, normally not provided in the engine block. Removing the piston, the liner is no longer involved in the motion operation. Consequently, it is possible to replace the liner introducing a custom component which allows the balancer rod mounting. However, the design space available for the balancer rod strictly depends on the liner dimensions because it composes part of the water jacket that must not be changed (see the cooling system analysis in section 4.6).

The Ducati company provides two different liner for the same engine block varying in the bore dimensions. In particular, the *Panigale 959* model (object of this study) is equipped with a liner of 100 mm bore, while the *Panigale 1299* model presents a liner of 116 mm bore in order to obtain the displacement of 1299cc. Definitely, considering the size of the balancer rod support, it is

possible to go up to 116 mm, which is another constraint that limits the position and the dimensions of the balancer rod (Figure 5.10).

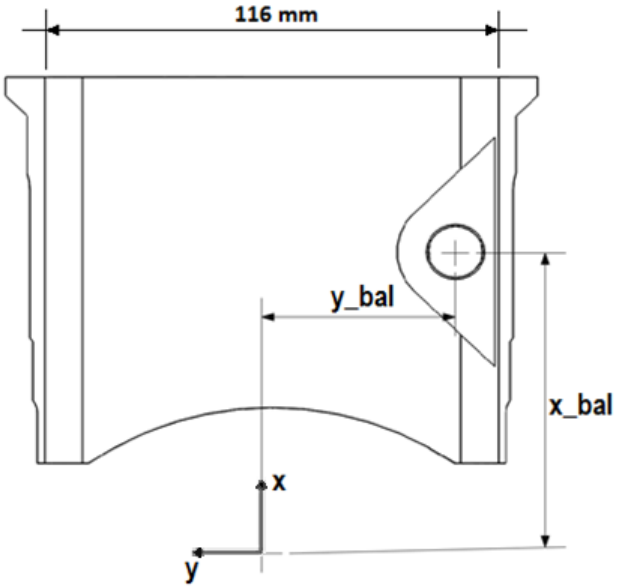

Figure 5.10. Custom liner with balancer rod mounting.

In particular, fixing the pivot centre, the maximum length of the balancer rod is automatically defined. However, the actual length (L_{bal}) has to be evaluated considering the kinematics of the mechanism. Similarly, the mass, the inertia and the position of the centre of gravity of the balancer rod have to be evaluated considering the dynamics of the mechanism [90]. To do so, a generic articulated quadrilateral mechanism has been considered in order to determine the specific motion law (Figure 5.11).

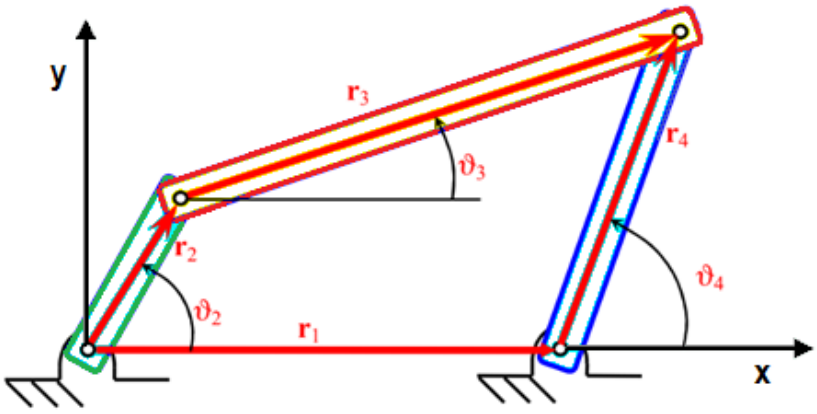

Figure 5.11. Generic articulated quadrilateral mechanism.

In Figure 5.11, the green member represents the crank throw, the red member represents the conrod while the blue member identifies the balancer rod, similarly to as shown in Figure 5.8. Each member can be identified by a vector passing through the cylindrical joint of each member. In particular, the vector r_1 is stationary during the motion because it represents the distance between the crankshaft axis and the pivot axis of the balancer rod.

Furthermore, the vectors r_2, r_3 and r_4 identify respectively the crank throw, the conrod and the balancer rod. The lengths of the vectors are known so the aim is to evaluate the angles and the position of the members 3 and 4. The four vectors form a closed loop, so it is possible to consider:

$$r_1 + r_4 = r_2 + r_3 \tag{5.11}$$

Then, it is possible to consider the components of each vector with respect to a local reference system with the origin on the crankshaft axis and the x axis passing through the balancer rod pivot:

$$\begin{cases} r_1 + r_4 \cos\theta_4 - r_2 \cos\theta_2 - r_3 \cos\theta_3 = 0 \\ r_4 \sin\theta_4 - r_2 \sin\theta_2 - r_3 \sin\theta_3 = 0 \end{cases} \tag{5.12}$$

where θ_i is the angle of each member as shown in Figure 5.11. Solving the equation:

$$\begin{aligned} 1 = \frac{1}{{r_3}^2} ({r_4}^2 \sin^2\theta_4 + {r_2}^2 \sin^2\theta_2 - 2r_2 r_4 \sin\theta_2 \sin\theta_4 + {r_1}^2 \\ + {r_4}^2 \cos^2\theta_4 + {r_2}^2 \cos^2\theta_2 + 2r_1 r_4 \cos\theta_4 \\ - 2r_1 r_2 \cos\theta_2 - 2r_2 r_4 \cos\theta_4 \cos\theta_2) \end{aligned} \tag{5.13}$$

from which:

$$\begin{aligned} (2r_2 r_4 \sin\theta_2)\sin\theta_4 + (2r_2 r_4 \cos\theta_2 - 2r_1 r_4)\cos\theta_4 \\ = {r_1}^2 + {r_2}^2 + {r_4}^2 - {r_3}^2 - 2r_1 r_2 \cos\theta_2 \end{aligned} \tag{5.14}$$

Formally, it is possible to consider:

$$A \sin\theta_4 + B \cos\theta_4 = C \tag{5.15}$$

So, the solution is:

$$\theta_4 = \pm \arccos\left(\frac{BC + A\sqrt{A^2 + B^2 - C^2}}{A^2 + B^2}\right) \tag{5.16}$$

which represents the angle of the balancer rod function of the crank angle, θ_2 (also referred to as θ in the standard crank mechanism). θ_4 is considered positive rotating in counter-clockwise direction starting from the x axis [91].

However, θ_4 is referred to the local reference system of the generic articulated quadrilateral. The actual balancer angle (β in Figure 5.7) with respect to the global reference system is defined as:

$$\beta = \theta_4 - \delta \tag{5.17}$$

where δ is the angle between the local and the global reference system.

At this point it is possible to evaluate the angular velocity of the balancer rod deriving β with respect to the time:

$$\dot{\beta} = \frac{d\beta}{dt} = \frac{d\beta}{d\theta}\frac{d\theta}{dt} = \frac{d\beta}{d\theta}\omega \tag{5.18}$$

where ω is the angular velocity of the crankshaft (engine speed). Similarly, it is possible to evaluate the angular acceleration of the balancer rod deriving $\dot{\beta}$ with respect to the time:

$$\ddot{\beta} = \frac{d\dot{\beta}}{dt} = \frac{d\dot{\beta}}{d\theta}\frac{d\theta}{dt} = \frac{d^2\beta}{d\theta^2}\omega^2 \tag{5.19}$$

The conrod motion in this mechanism is slightly different with respect to the standard crank mechanism. In fact, the conrod small end no longer presents a pure reciprocating motion, but it presents a rotating motion depending on the balancer rod. Consequently, it has been necessary to evaluate the angle of the conrod with respect to the cylinder axis:

$$\gamma = -\arctan\left(\frac{r\cos\theta - y_{bal} - L_{bal}\sin\beta}{x_{bal} + L_{bal}\cos\beta - r\sin\theta}\right) \tag{5.20}$$

where γ is the conrod angle considered positive in clockwise direction, θ is the crank angle and r is the crank radius. Similarly as described for the balancer, it is possible to evaluate the angular velocity deriving the conrod angle with respect to the time:

$$\dot{\gamma} = \frac{d\gamma}{dt} = \frac{d\gamma}{d\theta}\frac{d\theta}{dt} = \frac{d\gamma}{d\theta}\omega \tag{5.21}$$

and also the angular acceleration:

$$\ddot{\gamma} = \frac{d\dot{\gamma}}{dt} = \frac{d\dot{\gamma}}{d\theta}\frac{d\theta}{dt} = \frac{d^2\gamma}{d\theta^2}\omega^2 \tag{5.22}$$

Once the kinematics of the mechanism with the balancer rod has been defined, it is possible to consider the dynamics of the mechanism. In particular, an equivalent lumped parameter system of the conrod has been considered as described for the standard crank mechanism. However, also the moment of inertia of the conrod has been considered, which is no longer negligible with respect to the other inertial forces.

A generic geometry of the balancer rod has been considered because its definition depends on the dynamic analysis itself. In particular, a generic position of the centre of gravity has been considered on the motion plane, defined with respect to the local reference system. The motion of the centre of gravity is a rotating motion around the pivot of the balancer rod (point C in Figure 5.12).

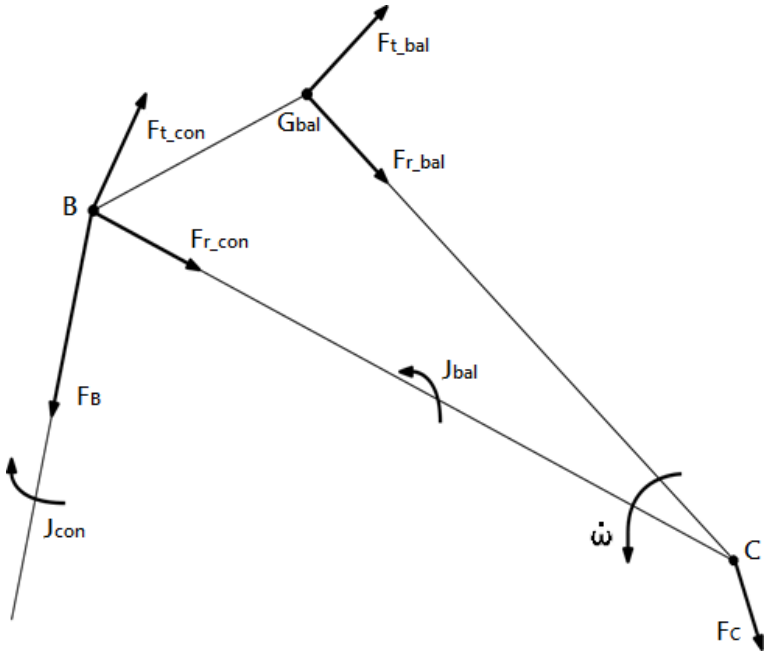

Figure 5.12. Forces acting on the balancer rod.

So, it is possible to decompose the inertial forces with respect to a tangential direction and a radial direction with respect to the circular path of the balancer rod. In particular, F_{t_bal} and F_{r_bal} are the inertial forces acting on the centre of gravity in tangential and radial direction respectively, depending on the mass of the balancer rod. Similarly, F_{t_con} and F_{r_con} are the inertial forces due to the reciprocating portion of the conrod ($\mathrm{m}_{\mathrm{c\_rec}} = \mathrm{m}_{\mathrm{B}}$ in Figure 5.2).

F_B represents the reaction of the conrod on the balancer rod while F_C represents the reaction of the support represented by the cylindrical joint.

Definitely, performing a dynamic balance of the system described it is possible to evaluate the forces F_B and F_C. Note that the direction of the force F_B is known, because the conrod can only react with a force directed along its axis. Then, the force F_B has been decomposed in the tangential and radial direction with respect to the crank throw, as well as for the standard crank mechanism.

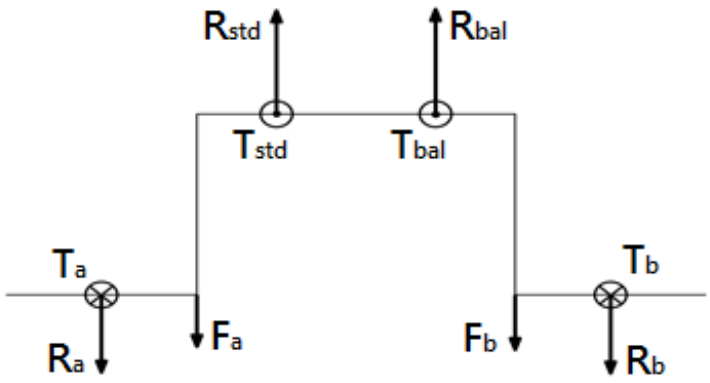

Figure 5.13. Force of the crank throw acting on the main journals.

The tangential component (T_{bal} in Figure 5.13) contributes to the portion of the torque of the crankshaft due to the inertial forces, together with the tangential component of the standard crank mechanism (T_{std} in Figure 5.13). Otherwise, the radial components (R_{bal} and R_{std} in Figure 5.13) determines the forces on the main journals, together with the radial force due to the mass of the crank pin (m_{cp}) and the radial force generated by the mass of the rotating portion of the conrod (m_{c_rec}). Finally, R_a and R_b represent the reaction forces of the main journals due to both crank mechanisms.

All these forces have been evaluated redacting a spreadsheet and the results are shown later in this section. Basically, these reactions need to be minimized working on the geometry and on the mass of the balancer rod. Several attempts have been made considering different balancer rod dimensions, as well as different position of the cylindrical joint support. However, the investigation of the best solution requires a more rigorous method able to optimize each variable of the problem.

To do so, a detailed model of the specific crank mechanism has been prepared using the software *GT-SUITE*, and in particular, the tool *GT-CRANK*. The software includes comprehensive tools for *Design of Experiments* (DOE) creation, analysis, and optimization. A *Design of Experiments* is an organized and structured method to determinate the relationships between dependent and independent variables. A DOE can be set up in order to determine the effect of one or more input parameters (factors) on various quantities of result (responses). After executing the DOE, it is possible to use the post-processor to analyse the results and perform optimization activities [92].

The model includes standard object as the *piston*, the *conrod*, the *crank pin,* the *web* and the *journal* which are used in order to represent the crankshaft and the standard crank mechanism (Figure 5.14).

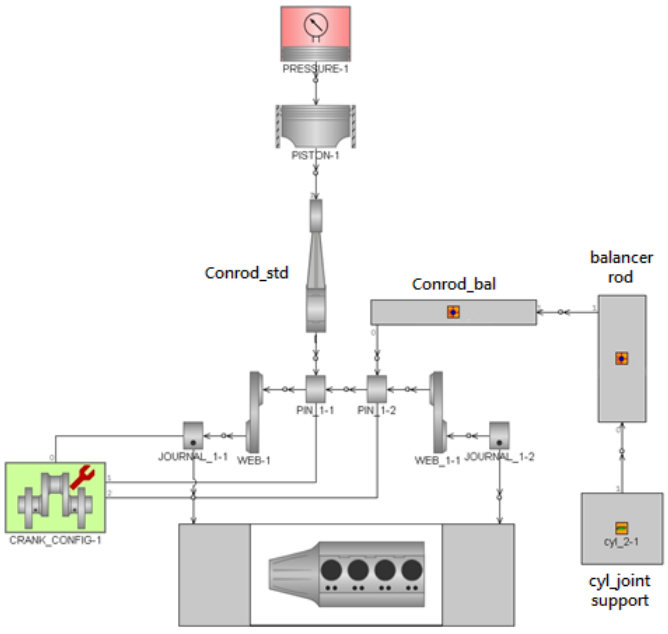

Figure 5.14. Schematic of the GT-CRANK model.

However, the balancer rod represents an unconventional device for an internal combustion engine, thus it has not been possible to use a pre-set object. It has been necessary to represent the balancer rod using a generic object setting information about dimensions, geometry, mass and moment of inertia. Similarly, also the conrod connected to the balancing rod has been represented using a generic object because it presents standard dimensions and mass but a significantly different kinematics and dynamics behaviour.

The outputs of this model have been compared with the spreadsheet in order to check the results and the correctness of the models (Figure 5.17 and Figure 5.18).

The aim of this study is to balance the crank mechanism reducing as much as possible the oscillations of the forces acting on the engine supports. To do so, an optimization of the design variables regarding the balancer rod has been performed. In particular, the design variables have been already described and here summarized: x_{bal}, y_{bal}, L_{bal}, m_{bal}, J_{Gz_bal}, g_{bal_x}, g_{bal_y}.

It has been important to identify the variables that significantly affect the results because the optimization of all these variables may requires too many resources. In particular, several considerations have been introduced in order to simplify the optimization process reducing the number of variables.

y_{bal} identifies the distance of the balancer rod pivot with respect to the cylinder axis. Ideally, a pure reciprocating motion ensure to restore the natural balancing of the two-cylinder V-type engine. Consequently, the distance y_{bal} must be chosen as greater as possible. However, this variable is limited by the liner dimensions and by the water circuit, as discussed previously in this section. So, y_{bal} has been fixed and not considered in the optimization process.

The moment of inertia of the balancer rod with respect to its centre of gravity, J_{Gz_bal}, depends on the mass and the shape of the component. However, the geometry of the balancer rod is rather defined because the design space is very limited (Figure 5.9). In fact, it is possible to assume that the J_{Gz_bal} depends only on the mass and the length of the balancer rod, neglecting the influence from the overall shape.

Similarly, another simplification has been introduced considering the position of the centre of gravity (g_{bal_x}, g_{bal_y}) depending only on the length of the balancer rod (L_{bal}). Also in this case, the influence of the overall shape has been neglected.

Finally, the variables x_{bal} , L_{bal} and m_{bal} have been considered as independent variables, while the others have been considered as dependent variables.

The target of the optimization process is the minimization of three forces: the reaction forces on both main journals and the reaction force on the balancer rod support (F_C). Moreover, a specific range has been defined for each variable considering the specific constraint. A short range has been defined for the

variables x_{bal} and L_{bal} because they are affected by the limited design space. Conversely, a wider range has been considered for the mass variable (m_{bal}).

The Figure 5.15 shows the *Design of Experiment* settings including the definition of the range for each variable and the number of steps in which subdivide the range.

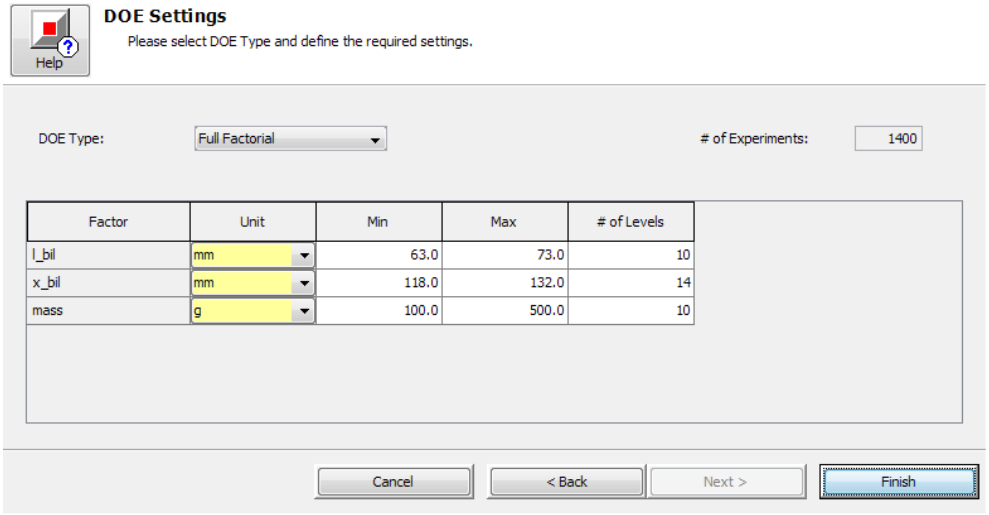

Figure 5.15. Design of Experiment settings and variables range definition.

The DOE optimization leads to the following parameters:

- $L_{bal} = 69.7\ mm$
- $x_{bal} = 124.5\ mm$
- $m_{bal} = 475\ g$

The Figure 5.16 shows the final geometry of the balancer rod considering the DOE optimization parameters.

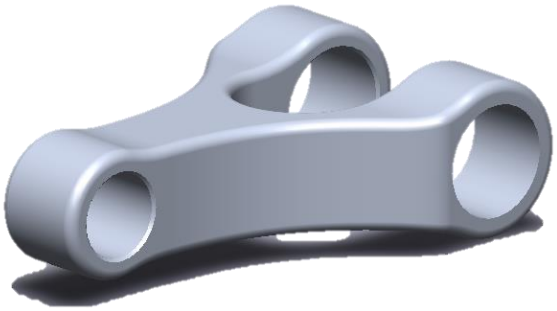

Figure 5.16. Final geometry of the balancer rod derived from the DOE optimization.

The results show the trend of each output force considering the geometrical dimensions and the mass derived from the optimization process. The same parameters have been included in the spreadsheet and the results have been compared in the graphs shown in the Figure 5.17 and Figure 5.18. In particular, the Figure 5.17 shows the forces on the main journal *"a"*, the one close to the

standard crank mechanism, while the Figure 5.18 shows the forces acting on the main journal *"b"*, the one close to the balancer rod mechanism.

It is possible to observe that both the spreadsheet and the GT-SUITE software lead to the same results, in fact, the curves are perfectly overlapped.

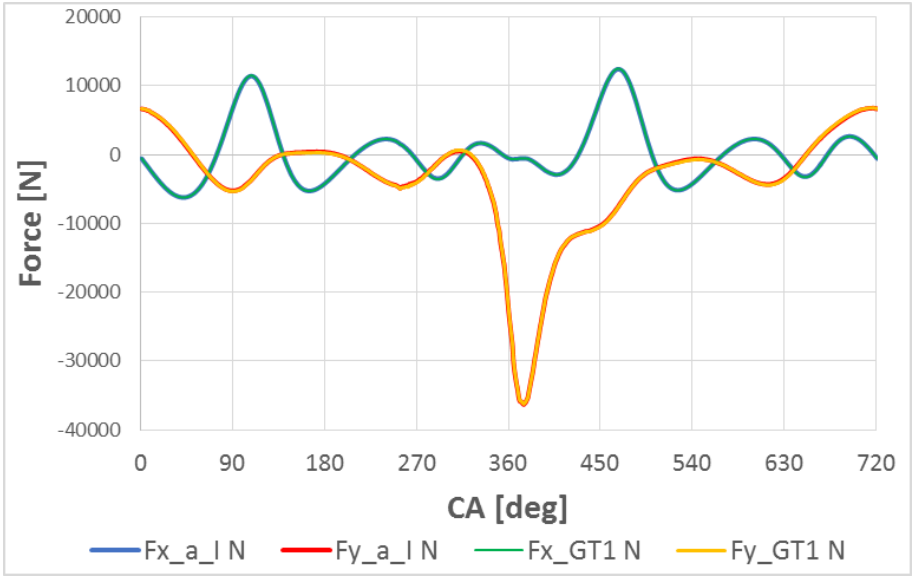

Figure 5.17. Forces on the main journal "a" decomposed along x and y: comparison between the spreadsheet and GT-SUITE.

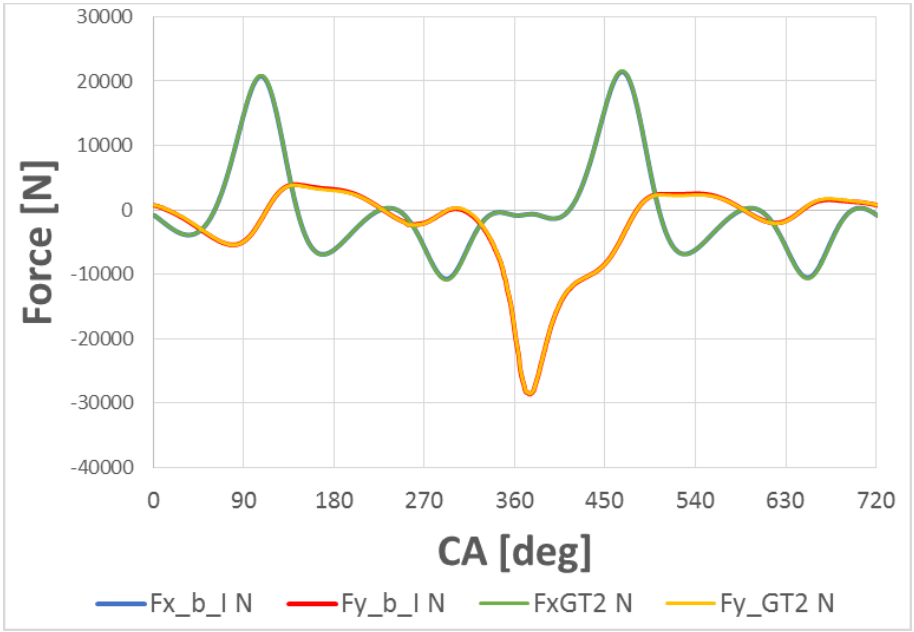

Figure 5.18. Forces on the main journal "b" decomposed along x and y: comparison between the spreadsheet and GT-SUITE.

It is possible to observe that the maximum force acting on the main journal *"b"* is almost twice the maximum force acting on the main journal *"a"*. This means that the balancer rod generates forces too different with respect to the standard crank mechanism, even though the geometry of the balancer rod derives from the DOE optimization. Consequently, the proposed mechanism is

not able to restore the natural balance of the original engine, considering this specific geometry. The main limits of the optimization are the range considered for each variable depending on the design space available.

Moreover, the introduction of the balancer rod causes the arising of an additional force on the engine block (F_C). In fact, the standard crank mechanism causes a normal force on the liner (constant in direction) generated by the lateral force of the piston, while the force (F_C) generated by the balancer rod results to be higher in modulus and varying in direction.

In conclusion, it has been not possible to reach the target imposed because the balancer causes a motion too different with respect to the reciprocating motion of the standard crank mechanism. Ideally, the length of the balancer rod should be slightly longer than the current dimension decreasing the amplitude of the balancer rod oscillation. In addition, a longer balancer rod also limits the amplitude of the force F_C.

6 STRUCTURAL ANALYSIS OF THE TRANSMISSION CHAIN

In the following section the dynamic behaviour of the timing chain of the original engine is investigated [93,94]. The aim is to assess the possibility of the use of the OEM timing chain as a transmission element for the EM. In fact, the differences introduced by the hybridization process change the loads acting on the chain. The torque that the chain has to manage is now determined by the interaction with the electric machine as the *valvetrain* is not present anymore. In particular, the actual chain load depends on the maximum torque deliverable by the EM and also on the inertia of the rotor and all the rotating components of the EM.

The torque of the EM is positive during the power delivery and negative during the energy recovery phase, so also the chain fatigue behaviour has to be investigated.

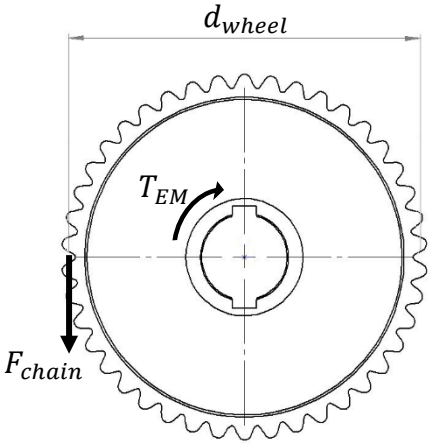

Figure 6.1. Chain upper wheel forces scheme.

However, the first check concerns to verify that the peak torque generated by the EM should not stress the chain above the tensile fatigue limit, F_{lim}:

$$\mathrm{F_{chain}} = \frac{\mathrm{T_{EM}}}{\frac{\mathrm{d_{wheel}}}{2}} = \frac{36.5\ [\mathrm{Nm}]}{\frac{0.0648}{2}[\mathrm{m}]} = 1125.96\ [\mathrm{N}]\ < \mathrm{F_{lim}} \qquad (6.1)$$

where T_{EM} is the peak torque of the EM, F_{chain} is the force transmitted to the chain and d_{wheel} is the base diameter of the wheel (Figure 6.1). F_{chain} results lower than the chain fatigue limit and this margin can be employed to properly set the pre-tension value ensured by the hydraulic tensioner (Figure 4.11) [95,96].

However, in the calculation above the EM torque has been considered as a constant value. Actually, also the rotating inertia has to be considered which varies during the engine cycle. Consequently, a more detailed dynamic analysis has to be developed. To do so, a *multibody* dynamic model has been prepared considering the entire drivetrain system.

6.1 DYNAMIC ANALYSIS

Engine efficiency and optimization are key aspects for automotive manufacturers which have particular attention for reduction of time to market, building up a synergic approach for new component's development using simulation. In particular to reach the best results in the shortest time it is used, in the preliminary stage of development, a massive support of simulation analysis. This type of approach is used to support the development of better chain timing drives focusing on improving durability, lower friction, less noise and reduced cost in less time than conventional trial and processes [97].

Multibody tools have an important role in order to predict the impact forces between the chain and different components of the system, as well as the evaluation of the loads acting on the chain itself considering the dynamic behaviour of the system [98]. In particular, *multibody* dynamic models of timing chain trains are developed to examine chain link connection force and contact force with sprocket, forces applied on tensioner, angular velocity fluctuation and chain trains operation loads during crankshaft speed fluctuation [99].

The first model presented hereafter refers to the original *desmodromic valvetrain* configuration, similar as found in literature [100,101]. The results of this model determine the behaviour of the chain to set as a reference. Subsequently, the modifications due to EM adding have been considered in a second model. The results have been then compared to the original configuration in order to assess in detail the choice of the drive layout and to check that component load limits are not exceeded.

The software employed is *AVL Excite Timing Drive* which is a *multibody* program for the study of dynamic behaviour for all components of the timing drive. Four configurations are available: Belt and Chain Dynamics (BCD), Gear Train Dynamics (GTD), Total Timing Drive (TTD), Single Valve Train (SVT). Obviously, the first case has been chosen in order to study the force between two chain-link, during some engine operating conditions. In particular, three operative conditions have been considered, referred to different engine speeds:

- Idle speed @ 3000 rpm;
- Maximum torque @ 8000 rpm;
- Maximum power @ 10000 rpm.

The real system is divided into a series of elements: single mass or connection elements, which can be called *generic elements,* and *specific elements*, which are specialized for standard timing drive applications. There are two types of *generic elements*: rigid bodies and connections. The rigid body elements contain information about the mass properties and some optional geometrical data. The connecting elements describe the forces acting between the rigid body elements. These elements are described in a generic way, thus they can also be used for more applications that are general and for more detailed

modelling of timing drive systems. In addition, *specific elements* contain mass and connection information, such as stiffness and damping.

For reliable results in an acceptable calculation time, the prepared model describes all relevant parameters of the real system using only a minimum of elements. Because timing drive systems contain a lot of non-linear elements (elements with variable stiffness, variable rocker arm ratios, gaps between components), the calculation method must be adjusted to these types of problems. Moreover, due to the non-linear characteristics of the considered systems their dynamic behaviour is calculated in time domain and a second order *Predictor/Corrector* method is used for these calculations [102–104]. An automatic adaptation of the calculation step width has been used, in order to achieve a good compromise between calculation accuracy and calculation time.

The Figure 6.2 shows all the elements that represent the model. Special specific elements have been adopted in the model in order to gain more flexibility.

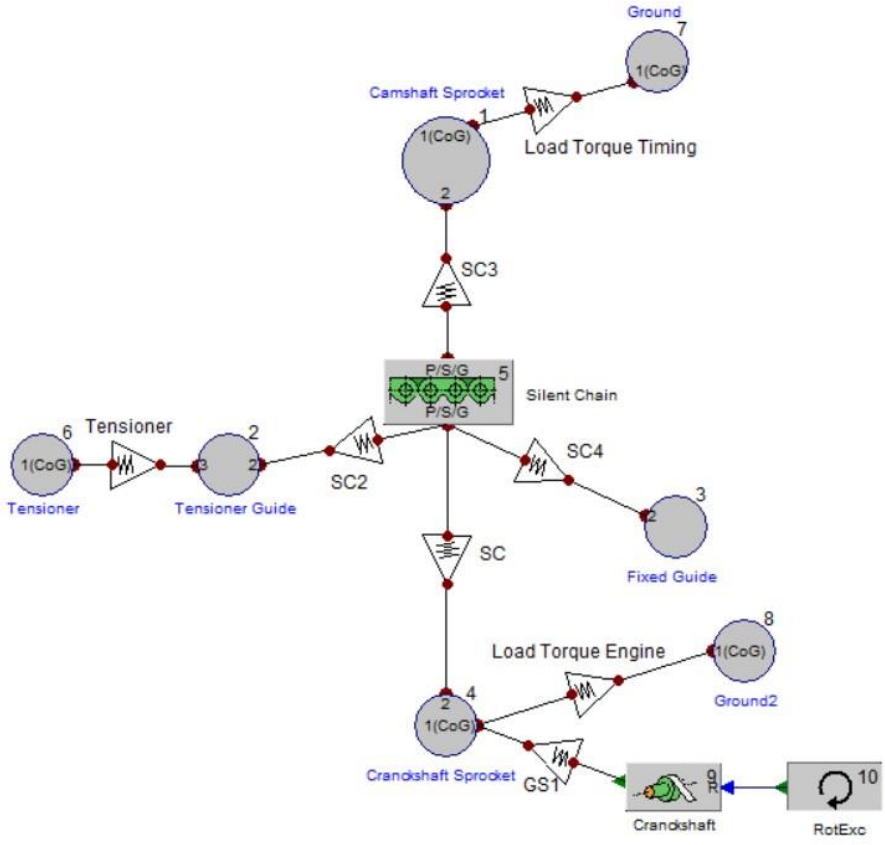

Figure 6.2. Excite Timing Drive model view.

In particular, it is possible to observe the object referred to the definition of the chain. This element contains all the information about the chain, including geometry, stiffness and dumping of each chain link. It has been necessary to define the geometric characteristics of the chain, so the nominal pitch, the number of chain link and the preload, which guarantees the correct movement

of the chain during its operation. All these parameters are shown in the Figure 6.3.

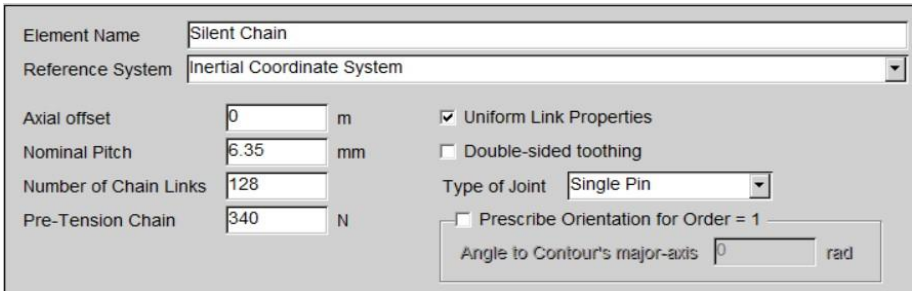

Figure 6.3. Geometric parameters of the chain.

Then, it has been necessary to define the geometry of the single chain link, considering separately the backside and the lower side of the link. To do so, the CAD model of each component has been analysed, identifying several points on the contour of the part. The coordinates of these points, with respect to the centre of gravity of the component, have been written into a txt file. The coordinates of these points are plotted in Figure 6.4.

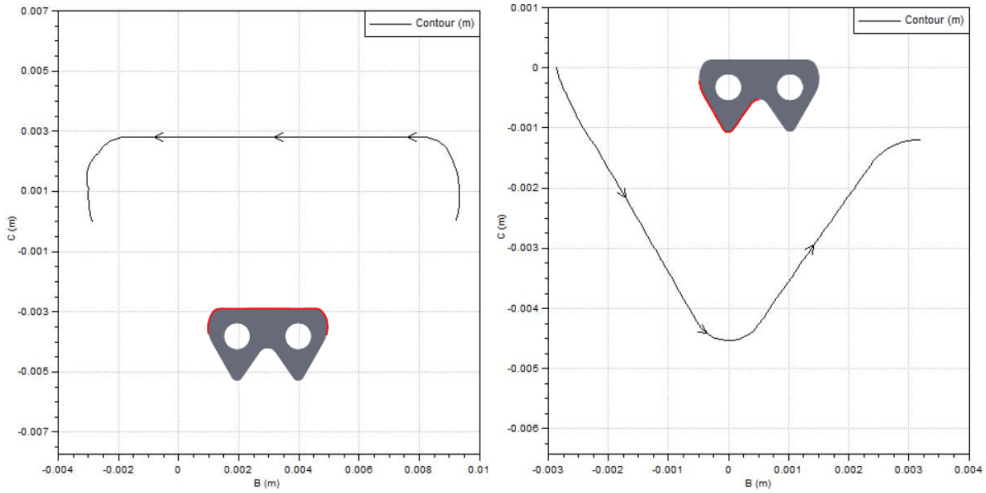

Figure 6.4. Contour data of the backside link (left) and lower link (right).

The chain link geometry is finally defined as shown in the Figure 6.5, where it is possible to identify also the information about the mass and the moment of inertia of the single link derived from the CAD model. The pin joint is defined by the pin diameter and the bore of the chain link with which it is touching to (Figure 6.6).

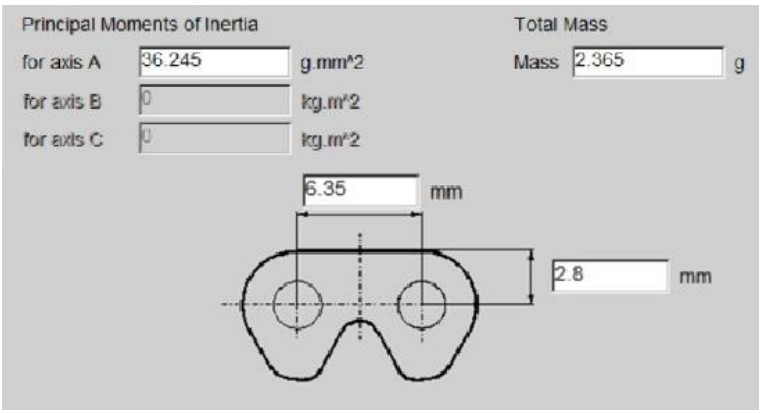

Figure 6.5. Single chain link geometry and mass properties.

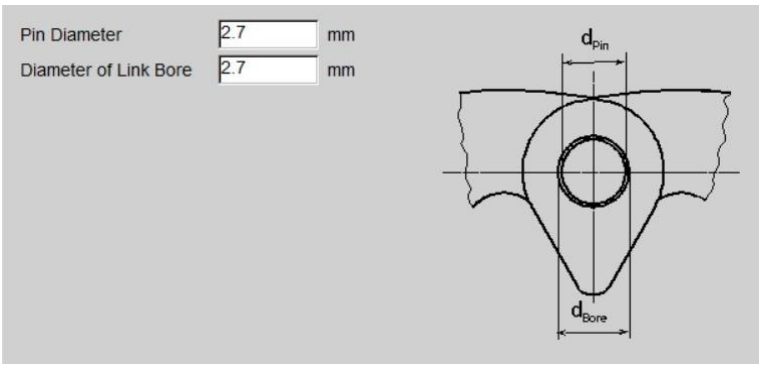

Figure 6.6. Chain pin joint geometry properties.

For the link connections, it is necessary to define the stiffness, the damping and the friction between each chain link.

The stiffness of the chain link has been evaluated performing a Finite Element Analysis considering the single module as shown in Figure 6.7. In particular, the module has been modelled considering half of the outer link, half of the inner link and the pin. Moreover, it has been possible to consider the symmetry of the single module, taking the advantages of the reduction of the number of elements, thus considering the proper constraints. In the model, a fixed displacement has been imposed and the reaction force has been evaluated. Definitely, the value of the stiffness of the single chain link derived from the model is equal to 74160 N/mm.

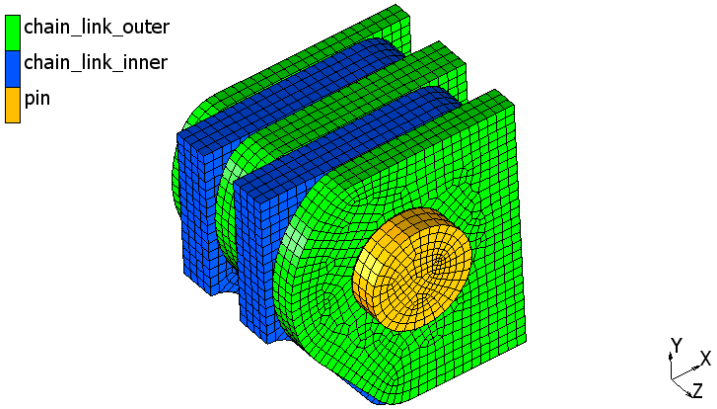

Figure 6.7. Chain link Finite Element Analysis.

For the damping in normal direction a pure viscous behaviour is assumed. The applied damping coefficient is obtained by using common estimations for the relative damping (*Lehr's damping*) [105,106]. To obtain a reasonable value for the damping at the link-connection the following procedure is applied. For a span with the length of 277.8 mm (Figure 6.10) a relative damping coefficient of 2.5 up to 6 % can be used [107]. For one single link the relative damping is about 44 times higher (277.8mm span/6.35mm pitch). Assuming a relative damping coefficient of 5% for 277.8 mm span this gives a relative damping of about 220% for one chain link (44 x 5%). In particular, using the *Lehr*'s equation:

$$d = 2 \cdot D \cdot \sqrt{m_{link} \cdot K_{link}} \qquad (6.2)$$

where D is the relative damping coefficient, m_{link} [kg] is the mass of the chain link and K_{link} [N/m] is the stiffness of the chain link derived from the Finite Element model. This equation leads to an absolute damping value *(d)* of about 1840 Ns/m.

The friction element of the outer-inner link connection serves to consider the friction moment, which is acting between the pin and bushing, assumed equal to 0.05 as a first approximation.

Moreover, for each element of the model connected to the silent chain, it has been necessary to define the contour of the real component which the element refers to, as well as described for the chain link. The components involved in the contact interaction with the chain result to be the upper and lower sprocket, engaged respectively with the camshaft and the crankshaft. The Figure 6.8 shows the contour data of the both camshaft and crankshaft sprocket tooth.

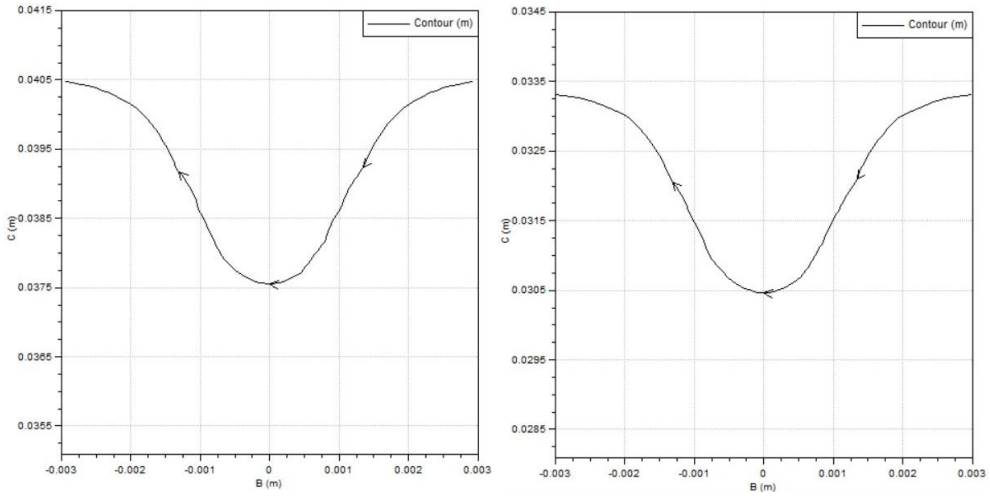

Figure 6.8. Camshaft (left) and crankshaft (right) sprocket tooth contour data.

In addition, also the guide rails are in touching onto the outer edge of the chain. So, the profiles of both fixed and floating guide rails are defined and plotted in Figure 6.9.

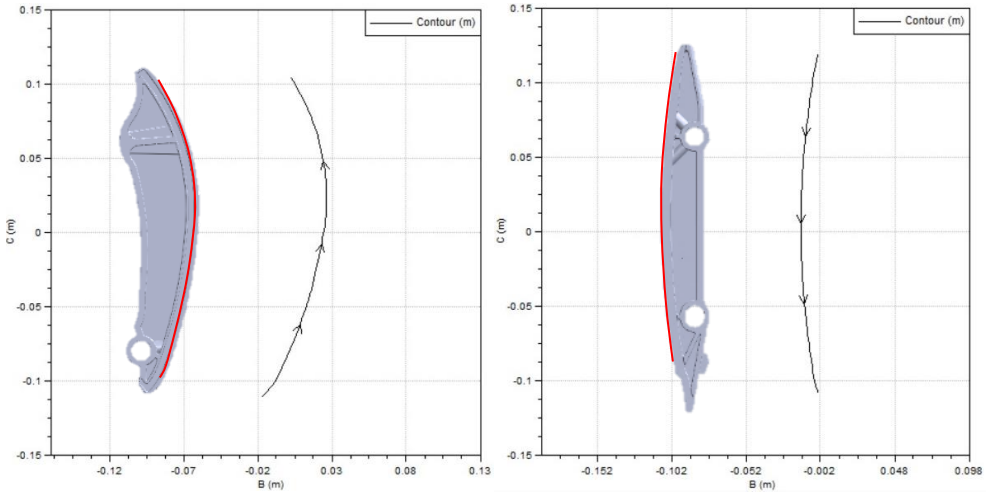

Figure 6.9. Floating (left) and fixed (right) guide rail contour data.

The complete assembly of the valvetrain is also shown in Figure 4.11, where it is possible to recognize the chain, the crankshaft sprocket (in the bottom), the camshaft sprocket (wheel A) and both guide rails.

Each element of the model has to be positioned with respect to the reference system. In particular, the crankshaft axis has been considered as the origin of the reference system. Moreover, for each component the proper degrees of freedom (DOFs) have been defined: the sprockets can rotate around their own axis; the floating guide rail can rotate around its pivot and its motion is controlled by the tensioner; the position of the fixed guide is finally locked in the space.

The final representation of the chain is show in Figure 6.10. Once the total length of the chain is known – function of the total number of links and pitch –

the course is automatically defined depending by the sprockets position and by the guide rails shape.

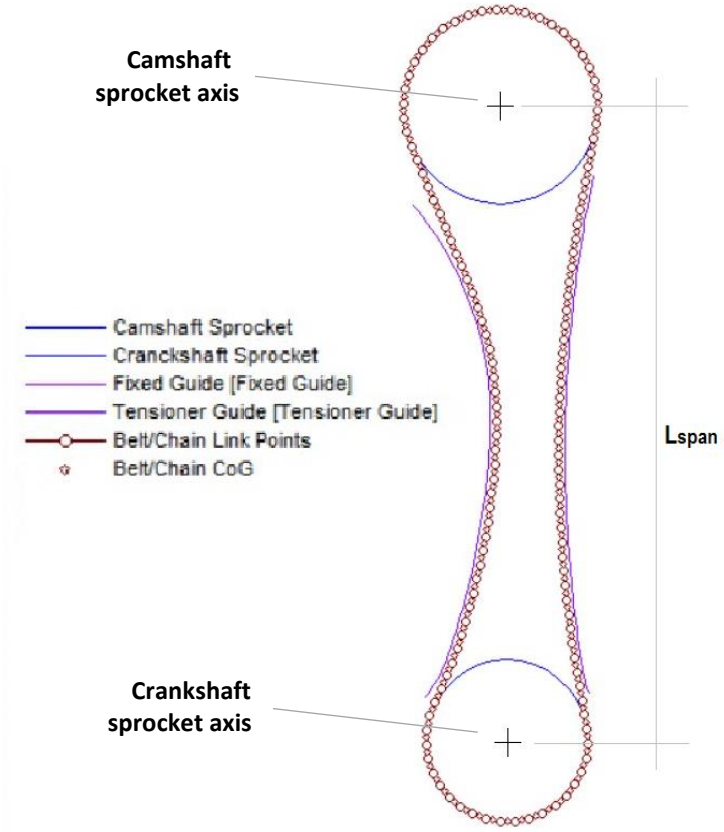

Figure 6.10. Chain course representation.

The model as it exists now represents only the "*naked*" chain drive. After the definition of the geometrical, mass and inertia properties of the entire chain system, information about crankshaft excitation, load and chain-tensioner are needed.

The whole crank mechanism can be analysed as a flywheel system considered as a concentrated inertia [108]. The equivalent inertia, $J_{cm,eq}$, is the composition of three different contributions:

- The mean contribution of the total reciprocating masses of the crank mechanism, $\bar{J}_{rec\_tot}$;
- Contribution of the rotating portion of the conrod, J_{c_rot};
- Contribution of the purely rotating masses, J_{rot}.

The equivalent inertia related to the total reciprocating masses actually varies with the crank angle, θ, and it can be evaluated via the energetic equation:

$$\frac{1}{2}J_{rec\_tot}(\theta)\omega^2 = \frac{1}{2}\left(m_{rec} + m_{c\_rec}\right)v(\theta)^2 \qquad (6.3)$$

Noting that $v(\theta) \approx \omega r(\sin(\theta) + \frac{\lambda}{2}\sin(2\theta))$ and neglecting the higher-order terms:

$$J_{rec\_tot}(\theta) \approx \left(m_{rec} + m_{c\_rec}\right) r^2 \sin^2(\theta) \tag{6.4}$$

Then, integrating on the cycle, the mean equivalent value is obtained:

$$\bar{J}_{rec\_tot} = \frac{1}{2}\left(m_{rec} + m_{c\_rec}\right) r^2 \tag{6.5}$$

where, m_{rec} [g] is the reciprocating mass (piston, rings and gudgeon pin), m_{c_rec} [g] is the conrod reciprocating mass, m_{c_rot} [g] is the conrod rotating mass and r [mm] is the crank radius.

The contribution of the rotating portion of the conrod can be estimated as:

$$J_{c\_rot} = m_{c\_rot} \cdot r^2 \tag{6.6}$$

While the inertia of the purely rotating masses (J_{rot}) can be directly evaluated considering the 3D model of the crankshaft, including the crankshaft sprocket inertia, the flywheel and the clutch bell engaged to the crankshaft.

The sum of these contributions represents the total equivalent inertia of the crank mechanism ($J_{cm,eq}$) with respect to crankshaft axis.

$$J_{cm,eq} = \bar{J}_{rec\_tot} + J_{c\_rot} + J_{rot} \tag{6.7}$$

Moreover, the crankshaft excitation due to the torque oscillation has been considered. To do so, a specific spreadsheet has been prepared starting from the kinematic and dynamic of the crank mechanism and considering the pressure of the combustion gases. In particular, the contribution of the inertial forces and the contribution of the gas forces have been considered separately. The Figure 6.11 shows these contributions referred to the single crank mechanism.

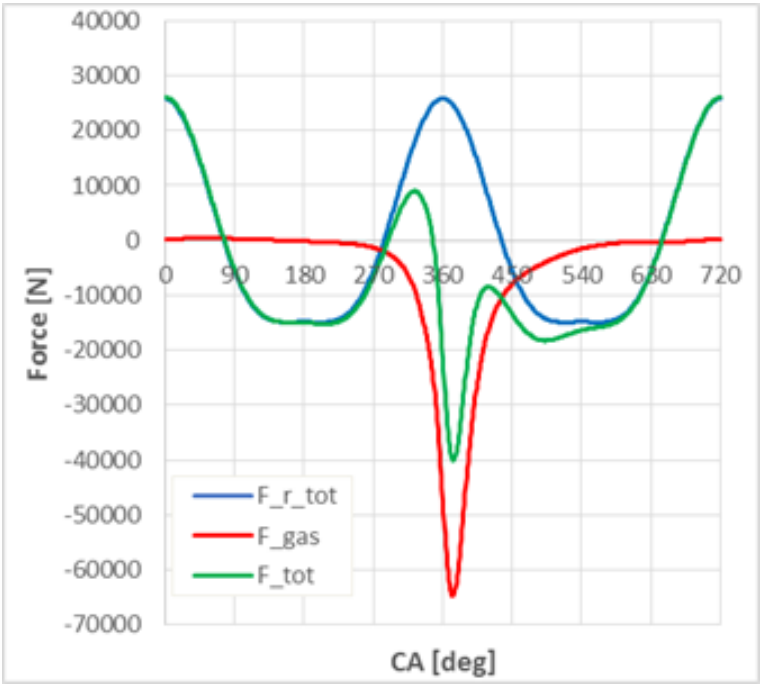

Figure 6.11. Combustion gas forces (red) and inertial forces (blue).

The forces generated by the combustion gases (F_g) have been evaluated considering the real pressure trace measured during the experimental tests at the dynamometer bench.

The total force acting on the upper part of the crank mechanism (F_{tot}) is the composition of the instantaneous total reciprocating inertial force (F_{r_tot}) and the instantaneous gas force (F_g). F_{tot} is always directed along the cylinder axis. Considering that the conrod only resists to a force aligned with its axis, the conrod force is amplified when it tilts:

$$F_{con} = \frac{F_{tot}}{\cos\varphi} \tag{6.8}$$

where F_{con} is the force along the conrod axis and φ is the conrod angle with respect to the cylinder axis.

In order to evaluate the crankshaft torque (T_{tot}), the conrod force (F_{con}) has to be decomposed in F_{con_t}, circumferentially directed and F_{con_r}, radially directed with respect to the crank throw direction. In particular, the crankshaft torque is calculated considering F_{con_t}:

$$F_{con\_t} = F_{con}\sin(\vartheta + \varphi) = F_{tot}\frac{\sin(\vartheta + \varphi)}{\cos\varphi} \tag{6.9}$$

So, the torque can be evaluated considering the different contributions of the reciprocating forces and the gas forces multiplied to the crank throw (r):

$$T_{in} = F_{in}\frac{\sin(\vartheta + \varphi)}{\cos\varphi}r \tag{6.10}$$

$$T_g = F_g\frac{\sin(\vartheta + \varphi)}{\cos\varphi}r \tag{6.11}$$

$$T_{tot} = T_{in} + T_g \tag{6.12}$$

These values have been considered for both crank mechanism and composed considering the Vee angle between the two banks (90 degree).

The Figure 6.12 shows the torque curves due respectively to the inertial loads (in blue) and to the gas forces (in red). Finally, the green curve identifies the total torque which represents the values considered as the excitation of the crankshaft in the dynamic model.

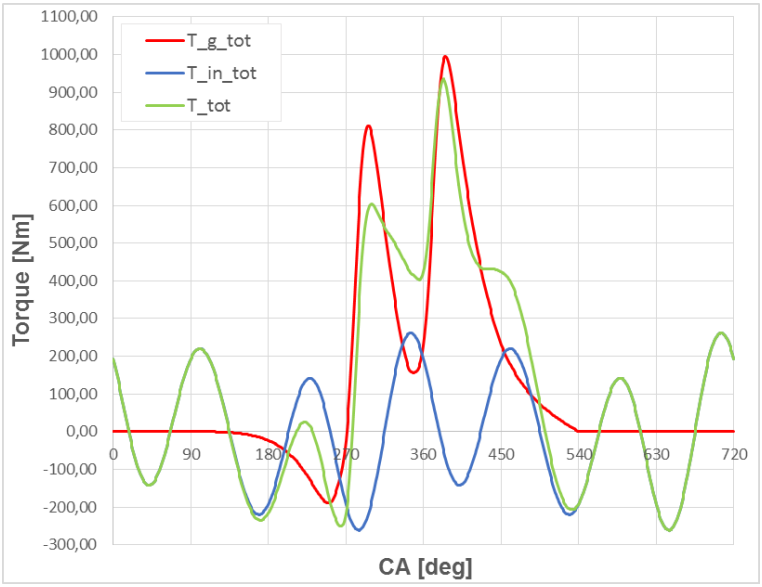

Figure 6.12. Crankshaft torque curves: inertial (blue), combustion gases (red) and total.

Once the equivalent moment of inertia and the engine total torque have been evaluated it is possible to determine the engine speed irregularity. The cyclic *irregularity index* of a crank mechanism has an important role and it is defined as:

$$\delta = \frac{\omega_{max} - \omega_{min}}{\omega} \tag{6.13}$$

where ω_{max}, ω_{min} *and* ω are respectively the maximum, minimum and average angular velocity within the engine cycle. In fact, even if the average torque balances the external resistant torque, the angular velocity of the engine is not constant. In particular, when the instantaneous torque overcomes the external torque, the exceeding work is accumulated as kinetic energy and the instantaneous angular velocity increases. Conversely, when the instantaneous torque is lower than the external torque, the required work is provided by the accumulated kinetic energy and the instantaneous angular velocity decreases. Considering $W(\vartheta)$ as the *effective engine work* due to the combustion gas torque and the inertial torque, it results:

$$W(\vartheta) = \int_0^{\vartheta} T_{tot}(\vartheta)\, d\vartheta \tag{6.14}$$

Obviously, the work within the engine cycle due to the inertial forces results to be null and only the work of the combustion forces remains. Denoting W_d as the *dissipated work* of the external torque, the exceeding work is equal to:

$$\Delta L = W(\vartheta) - W_d = \Delta E_k \tag{6.15}$$

So, the exceeding work is equal to the kinetic energy variation of the rotating masses, defined as:

$$\Delta E_k = \frac{1}{2} J_{cm,eq} \omega_{ist}{}^2 - \frac{1}{2} J_{cm,eq} \omega^2 \tag{6.16}$$

where $J_{cm,eq}$ is the equivalent inertia of the crank mechanism evaluated in the Equation (6.7). From the Equation (6.16) it is possible to obtain the value of the instantaneous angular velocity, ω_{ist}, represented in Figure 6.13 for the case of maximum power (at 10000rpm), due to the engine irregularity. The same procedure has been performed for the other two operating conditions, at 8000 rpm and 3000 rpm, as well as for the hybrid configurations. In fact, in each case the engine torque varies and consequently the engine irregularity results to be different.

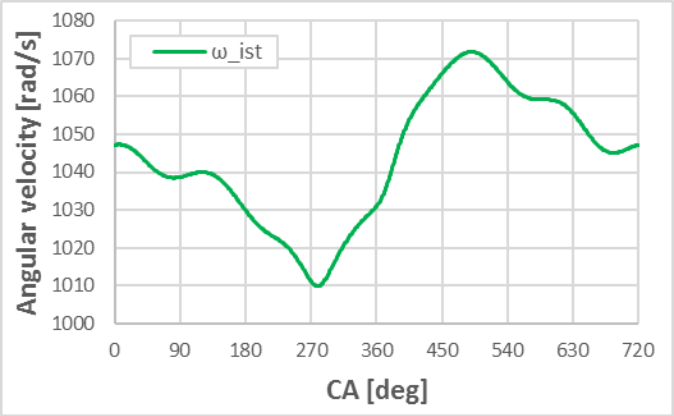

Figure 6.13. Instantaneous angular velocity at 10000 rpm (expressed in rad/s).

These values of angular velocity are then considered in the model as excitation input on the crankshaft.

Next, a very simple representation of the chain-tensioner is introduced, considering a preloaded spring-damper connection. The position of tensioner is determined with respect to the centre of gravity of crankshaft sprocket and the parameters needed to fully determine its behaviour are the stiffness of the spring, introducing a preload, and the damping.

Another excitation to be considered is the load to apply to the camshaft sprocket. However, it depends on the specific case of study. In fact, from this point forward two separated model are considered, discerning the case of the original *valvetrain* and the case of the electric motor connection.

6.1.1 Valvetrain model

In this case the original *valvetrain* system has been considered. In particular, the timing system is composed by a *desmodromic* actuation, which is a mechanism with positive-drive cams and presents different dynamic behaviour [109], in comparison with the widely used trains having a closing spring [110,111].

The *desmodromic* actuator system considered is shown in Figure 6.14 which identifies the CAD model of both intake and exhaust valves system. In particular, it is possible to identify the opening cam (in blue), the closing cam (in yellow), the opening finger (in green) and the closing finger (in red).

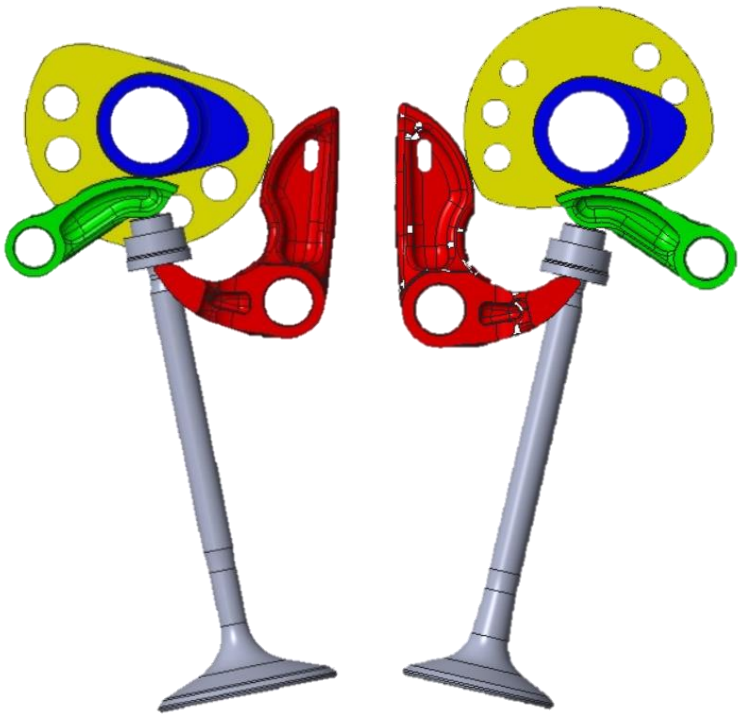

Figure 6.14. Intake and exhaust desmodromic valve actuator system.

For each component an equivalent moment of inertia has been evaluated. The moment of inertia of valve and fingers has been evaluated considering an energetic balance, because they present a non-rotational motion. Moreover, these values are not constant and vary with the camshaft angle, so the mean value has been considered. In particular, the valve presents a translational motion along its axis, so:

$$\bar{J}_v = m_v \int_0^{\theta_c} h^2(\theta_c)\, d\theta_c \qquad (6.17)$$

where h is the valve lift, θ_c is the cam angle and m_v is the mass of the valve. Similarly, it is possible to evaluate the mean value of the moment of inertia of the finger with respect to the camshaft axis as follow:

$$\bar{J}_f = J_{f_0} \int_0^{\theta_c} \left[\frac{d\beta(\theta_c)}{d\theta_c}\right]^2 d\theta_c \qquad (6.18)$$

where J_{f_0} is the moment of inertia with respect to the finger pin axis and β is the finger oscillation angle.

The same operation has been performed for each valve (intake and exhaust) and for each finger (closing and opening).

For the camshaft, which presents a rotating motion, the moment of inertia has been calculated with respect to its axis and summarized to $\bar{J}_v$ and $\bar{J}_f$, because now referred to the same axis.

Then, the total equivalent moment of inertia of the camshaft (J_{tot_eq}) has been reduced ($J_{tot\_eq\_red}$) to the camshaft sprocket axis (Figure 6.10), considering an energetic balance, in particular:

$$\frac{1}{2} J_{tot\_eq} \omega_{cam}{}^2 = \frac{1}{2} J_{tot\_eq\_red} \omega_{cam\_sprocket}{}^2 \quad (6.19)$$

where ω_{cam} is the angular velocity of the camshaft and $\omega_{cam\_sprocket}$ is the angular velocity of the camshaft sprocket. Considering:

$$\frac{\omega_{cam\_sprocket}}{\omega_{cam}} = \tau_{gear} \quad (6.20)$$

as the transmission ratio between the gear B and C (see Equation (4.1)), then:

$$J_{tot\_eq\_red} = \frac{J_{tot\_eq}}{\tau_{gear}{}^2} \quad (6.21)$$

Definitely, this value represents the total equivalent moment of inertia of the *desmodromic* valve system with respect to the camshaft sprocket axis.

The torque needed to actuate this mechanism depends on the acceleration profile due to the valve motion, as well as on the mass of the valve itself. The determination of the camshaft torque has been evaluated by a kinematic/dynamic analysis using the software *PTC Creo*.

The opening/closing fingers have been constrained using a pin constraint that allows the rotation around its axis, while a cylindrical constraint has been applied to the valve that determines the translation along its axis. The coupling cam-fingers and fingers-valve has been realized by a cam coupling, enabling the detachment between cams and fingers, allowing to lose the relative contact.

The intake and the exhaust valve systems have been considered separately. So, the actuation torque curves evaluated by the dynamic analysis for the intake and the exhaust camshaft have been combined considering the proper phase between the two actuators. The Figure 6.15 shows the results of the total actuation torque. Some discontinuity can be noticed due to the uncertain clearance between cams, fingers and tappets.

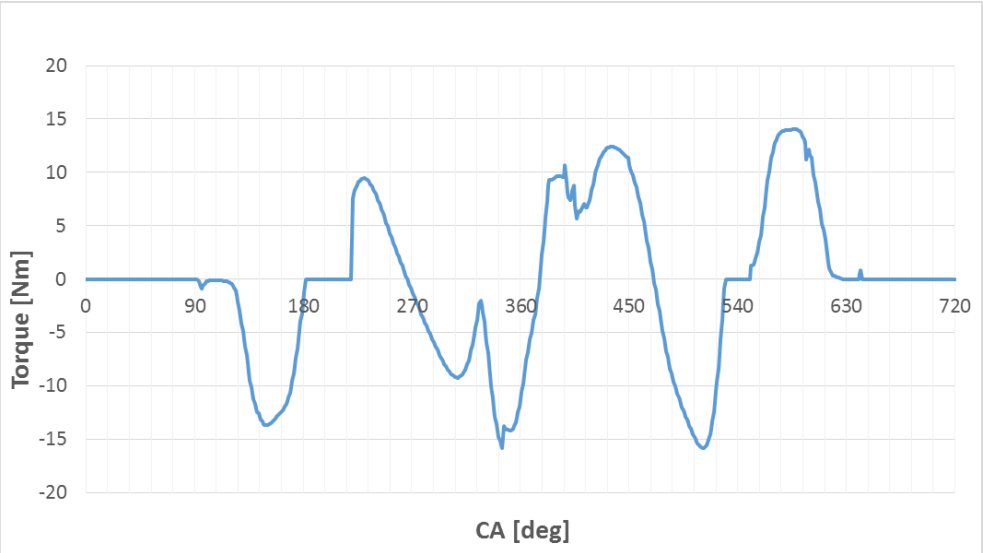

Figure 6.15. Total torque applied to the camshaft sprocket to actuate intake and exhaust system.

Then, these values have been reduced to the camshaft sprocket axis (Figure 6.10) in order to apply this load as excitation in the model. To do so, the transmission ratio between the gear B and C (Figure 4.11) has been considered, in particular:

$$T_{cam\_sprocket} = \frac{T_{cam\_int\_exh}}{\tau_{gear}} \tag{6.22}$$

where $T_{cam\_int\_exh}$ is the combination of the torque of both intake and exhaust system and τ_{gear} is the transmission ratio between the gear B and C (see Equation (4.1)).

Definitely, $T_{cam\_sprocket}$ represents the torque required for the valves actuation, applied on the camshaft sprocket. So, it has been applied to the model as the torsional excitation induced by the camshafts [112].

6.1.2 Electric Motor transmission model

As discussed in the previous sections, one of the engine head has been removed and replaced with the electric motor. Moreover, the crank mechanism has been kept in the original configuration for balancing reasons (see section 4), so the equivalent inertia of the crankshaft is the same of the previous model. However, removing the engine head, one of the cylinder results to be *"dead"* so the torque provided is more similar to a single cylinder engine. In this model the excitation of the crankshaft has been modified considering the combustion source of just one cylinder, while the inertial loads are the same (Figure 6.16). Consequently, the engine irregularity results to be different and the actual instantaneous angular velocity of the crankshaft has been evaluated again, as discussed before.

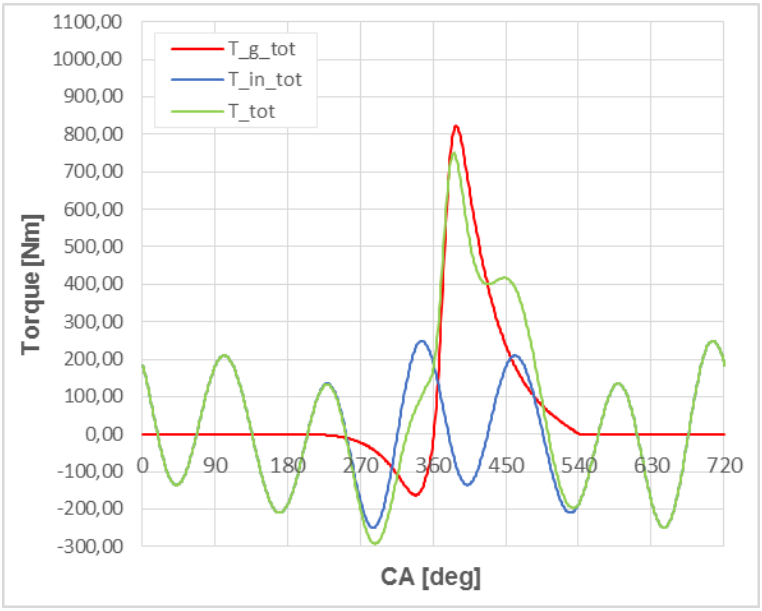

Figure 6.16. Crankshaft torque curves: inertial (blue), combustion gases (red) and total.

In addition, removing the engine head also the camshaft has been removed, so the total inertia with respect to the upper sprocket has to be revaluated. The electric motor is connected directly to the sprocket which is properly modified in order to ensure the torque transmission (Figure 4.12 and Figure 4.16).

In this case the total inertia depends directly on the EM shaft, the EM rotor, the keyways and the sprocket itself (see Figure 4.13). In fact, all these components represent the rotating parts of the electric motor.

Definitely, the total moment of inertia can be directly evaluated considering the CAD model of each component with respect to the rotation axis.

Similarly, the excitation no more depends on the actuation torque of the *valvetrain* but depends on the torque delivered by the electric motor. The EM can provide positive torque during the acceleration request, while it can deliver negative torque during braking, recovering energy [113]. Definitely, two different cases have been considered referred to the positive and negative peak torque of the EM. Actually, one additional case has been considered referred to the EM motored. In this case, no torque delivering is provided, so only the moment of inertia of the EM has been considered.

6.1.3 Results

In this section the results of the different configurations are presented. In particular, the cases considered are summarized as follow:

- Original valvetrain configuration (as reference);
- Electric Motor transmission (motored);
- Electric Motor transmission (negative torque delivering);
- Electric Motor transmission (negative torque delivering).

For each case three different engine speed has been considered as described at the beginning of this section. The speeds considered are 3000 rpm, 8000 rpm and 10000 rpm respectively referred to the idle speed, maximum torque speed and maximum power speed of the internal combustion engine.

The tension of the chain has been analysed during a complete cycle for each case and configuration. A chain cycle has not to be confused with an engine cycle. In fact, a single chain link has been considered during a complete turn of the chain. The duration of the cycle strictly depends on the engine speed and on the chain length, as well on the radius of the transmission wheels. From the engine speed is possible to determine the tangential velocity:

$$v = \omega r_w \tag{6.23}$$

where r_w is the radius of the lower transmission wheel and ω is the engine speed. Then, the time to finish a round is:

$$t_{chain} = \frac{L_{chain}}{v} \tag{6.24}$$

where L_{chain} represents the total length of the chain. Substantially, t_{chain} represents the time that takes the single chain link to go back to the same starting point. This time has been evaluated for each case related to the specific engine speed. In particular, one chain cycle is considered to be about two engine cycle, so the following results are referred to a crank angle sweep of 1440 degrees.

The load on the single chain link is determined by the relative oscillation between the upper sprocket and the crankshaft sprocket to which the instantaneous engine speed has been applied as excitation.

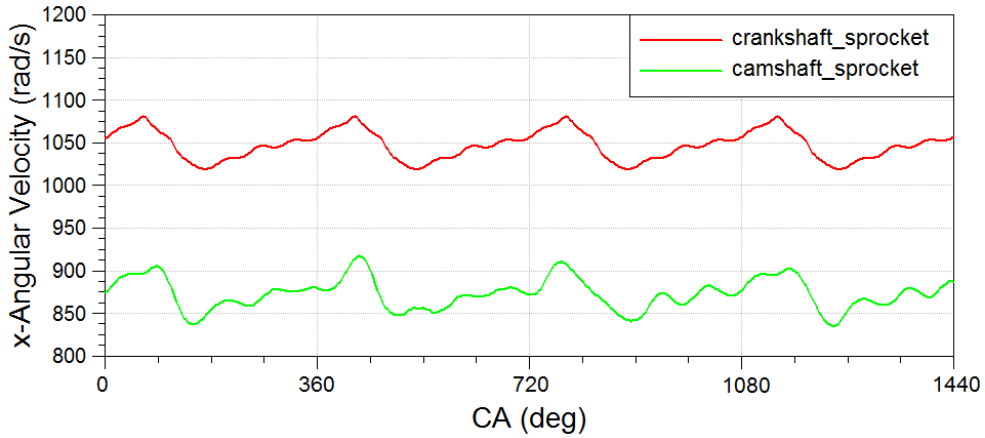

Figure 6.17. Instantaneous angular velocity of crankshaft and camshaft sprocket.

Figure 6.17 shows the instantaneous speed of both sprockets at 10000 rpm during the chain cycle, depending on dynamic behaviour of the system. The lower mean angular velocity of the camshaft sprocket is due to the chain transmission ratio, equal to 1.2.

Starting from the original configuration, consisting of the valvetrain system, the results are shown in Figure 6.18, comparing the three operating conditions analysed. The tension on the single chain link is shown during the chain cycle.

In this case the load trend of the valvetrain case vary depending on the speed. This is mainly due to the arising of the inertial phenomena of the valvetrain system that cause the fluctuations visible in Figure 6.18. In particular, at high speeds the valve has to be suddenly accelerated and decelerated within the cycle requiring higher actuating torque.

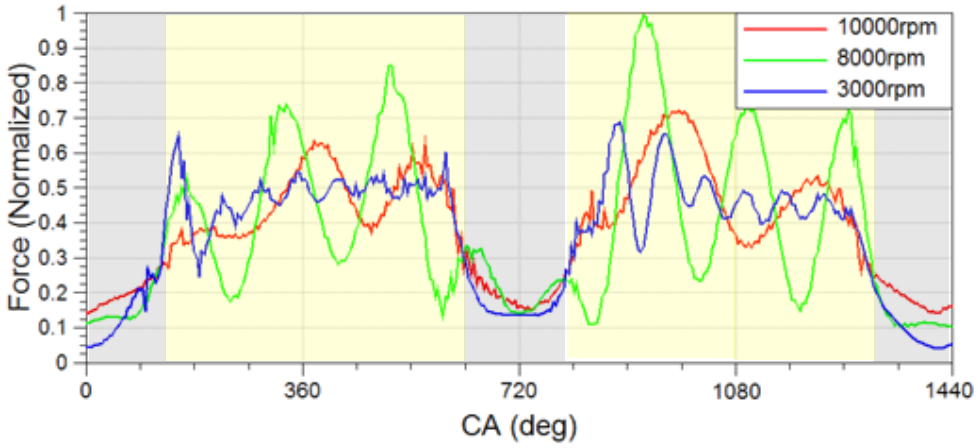

Figure 6.18. Chain link tension in the hybrid configuration at 3000 rpm, 8000 rpm and 10000 rpm.

The load on the chain link has been normalized to the maximum force registered in this configuration. The three curves present a similar trend even though the green curve identifies a maximum value greater than the other cases. In fact, the green curve refers to the maximum engine torque at 8000 rpm where the higher engine irregularity occurs. Moreover, in Figure 6.18 it is possible to identify also the minimum load on the chain link (grey sectors), similar in each condition, where the tension never drops to zero because a minimum preload of the chain has been considered. Conversely, the single chain link is mainly loaded when it is on the tensioned side of the chain (orange sectors).

An example of the generic situation of the chain is shown in Figure 6.19 considering the case that causes the maximum load (8000 rpm) in the *valvetrain* configuration during the instant of maximum load. In this case, the maximum value has been considered as the reference maximum force (F_{max}) in order to compare the results of the hybrid configurations.

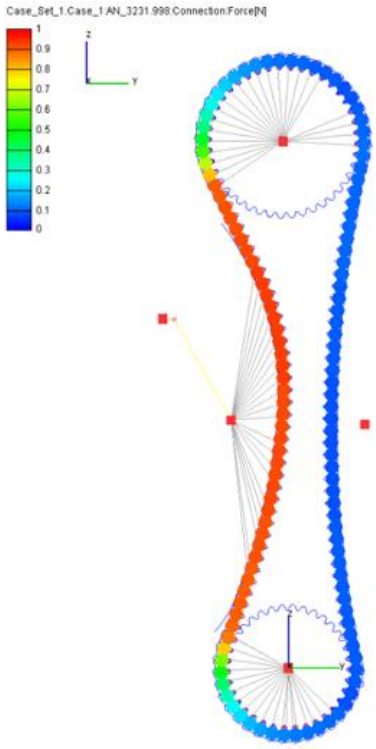

Figure 6.19. Chain tension force distribution on each link at 8000 rpm.

In the next model the electric motor is connected to the chain replacing the valvetrain system, as described in the previous sections. The results have been normalized to the maximum load of the previous configuration, F_{max}.

Figure 6.20 refers to the electric motor delivering a null torque, so only its inertia is considered. In particular, the maximum load is registered at 10000 rpm corresponding to the engine maximum power speed. In this model the single cylinder engine torque is considered to evaluate the instantaneous engine angular velocity (ω_{ist}).

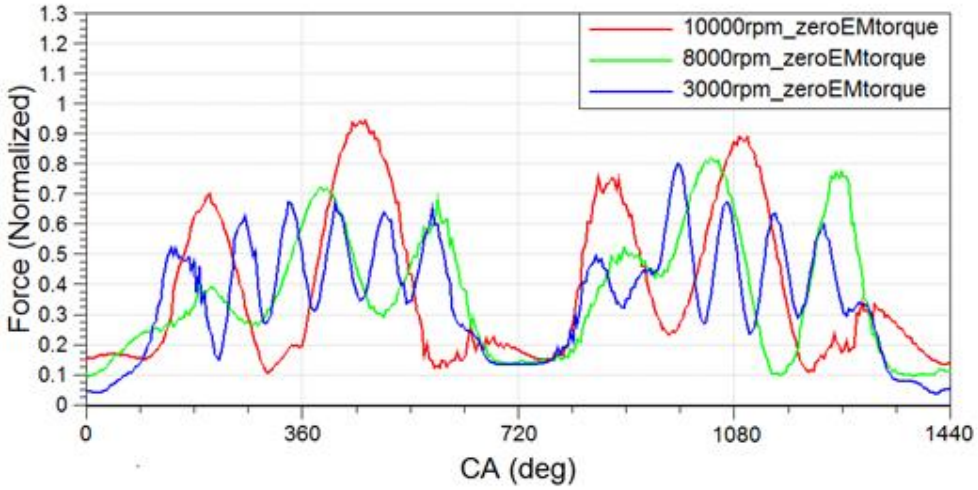

Figure 6.20. Chain link tension in the hybrid configuration (EM null torque) at 3000 rpm, 8000 rpm and 10000 rpm.

In the following, the speed of 10000 rpm has been selected to compare the hybrid configurations considering the electric motor delivering positive, negative and null torque (Figure 6.21). In particular, during the energy recovery phase the EM works as a generator and a negative torque is considered; conversely, a positive torque is considered when the EM provides a boost.

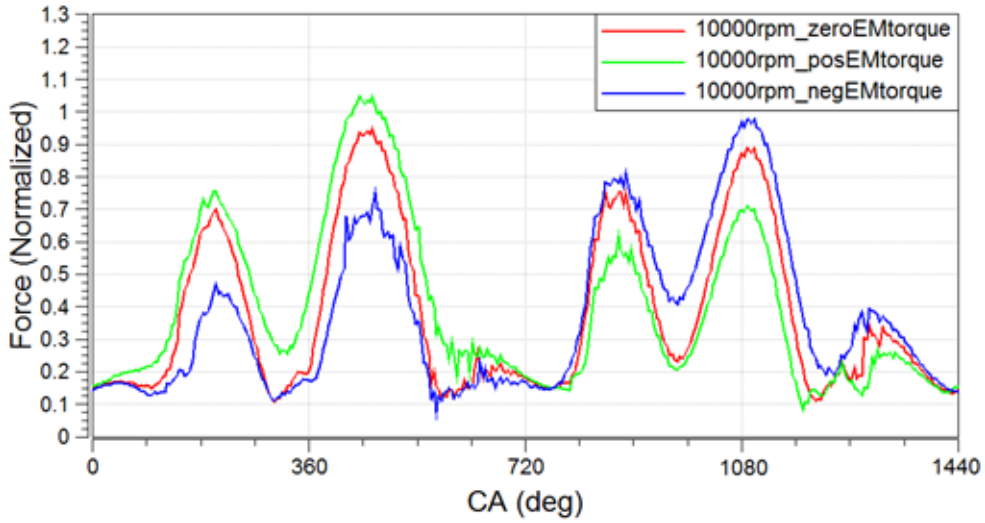

Figure 6.21. Chain link tension in the hybrid configuration at 10000 rpm referred to positive, negative and null EM torque.

The red curve in Figure 6.21 represents an intermediate case of load while higher loads can be identified for both positive and negative EM torque. In fact, in the same chain cycle, the negative torque determines a higher load with respect to the null torque (green curve over the red curve in Figure 6.21) but subsequently the situation is reversed (blue curve over the red curve in Figure 6.21).

In this case, the tensile force on the chain link reaches the maximum value of about $1.03 \cdot F_{max}$ applying the maximum torque of the electric motor in overload conditions (36.5 Nm). The EM can provide a value of torque greater than the actuation torque of the *valvetrain* system. However, this torque is not frequently delivered during standard operating conditions.

Definitely, the configuration with the electric motor connected to the chain causes not significant additional tensile load on the chain link. It determines values of the tensile force on the chain link comparable to the maximum value registered in the original *valvetrain* configuration (green curve in Figure 6.18).

However, the configuration with the EM led to different loading cycles. Consequently, a fatigue analysis has been carried out in order to investigate the fatigue behaviour of the chain.

6.2 FATIGUE ANALYSIS

A Finite Element model has been prepared in order to evaluate the fatigue safety factors referred to each configuration. A detailed fatigue analysis based on *Dang Van criterion* has been performed, which is a stress-based multi-axial criterion employed to evaluate a fatigue safety factor by taking into account the specific load cycles [114,115].

The same Finite Element model described in the previous sections has been considered, as shown in Figure 6.7, adding an RBE2 link in order to apply the specific loads.

Also in this case, the original valvetrain configuration has been taking into account as reference. In particular, a fictitious fatigue limit has been evaluated considering the valvetrain configuration loading cycle. In this way, the resulting fatigue safety factor for this configuration is equal to 1, named s_f. To do so, a dedicated *Fortran* subroutine has been used, already developed for similar fatigue issues [74,116].

The Dang Van safety factor contour plot for the hybrid configuration is shown in Figure 6.22. The loading cycle considered refers to the EM positive torque delivering, but similar results have been obtained considering the EM negative torque.

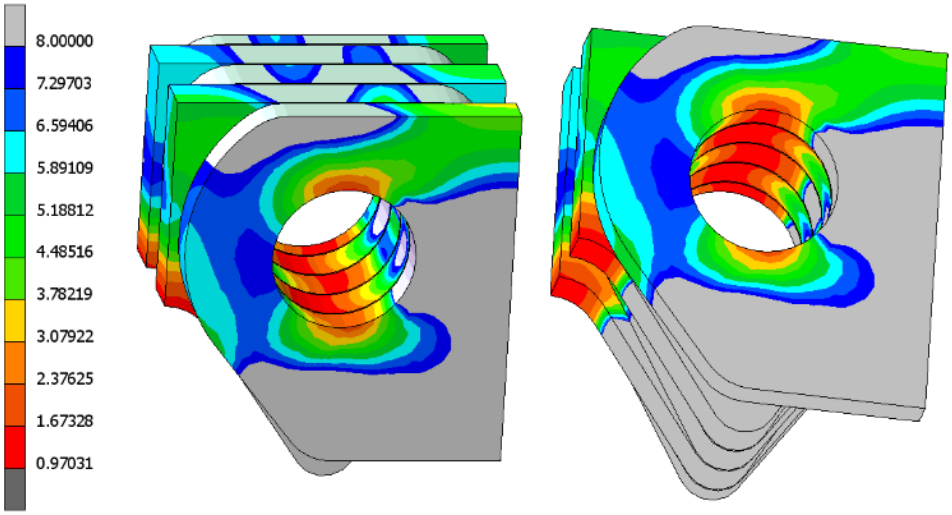

Figure 6.22. Fatigue safety factor contour plot on the chain link.

The whole component presents a minimum relative fatigue safety factor of about $0.97 \cdot s_f$, thus comparable to the original configuration. The most critical areas are restricted to the pin bore and on the tooth fillet of the chain link.

7 ENERGY MANAGEMENT OF THE HYBRID POWERUNIT

The presence of more sources of energy gives hybrid vehicles the freedom to choose, at each time, what the share of the propulsion power among the sources is. This freedom can well be exploited to reach some optimal operation, normally in terms of fuel consumption or emissions [117].

In this section a description of the reference car is introduced because it strictly affects the performance and the energy management of the hybrid *powerunit* [118]. For the considerations made in the introduction section on the positive and negative aspects of simple series and parallel hybrid architectures, it is clear that for a high-performance vehicle it is necessary to make more sophisticated and complex powertrain in order to reach the standards required [119,120]. However, the architecture presented results to be simpler because of the different constraints considered. In fact, the hybridization process consists of an electric motor blended to the internal combustion engine leading to a parallel architecture *P0*. The main reason of this choice was to obtain a *plu&go* solution replacing the minimum number of components, as better described in the section 4.

In a parallel HEV, the power required for propulsion is provided as mechanical power from the internal combustion engine (ICE) and torque from the electric motor (EM) [121,122]. The hybridization factor (HF) defines the portion of the power provided by the EM and the ICE, and it is shown as follow [123]:

$$HF = \frac{P_{EM}}{P_{EM} + P_{ICE}} = \frac{P_{EM}}{P_{tot}} \tag{7.1}$$

where P_{EM} is the power of the electric motor while P_{ICE} is the power of the internal combustion engine.

Numerically, this factor takes values in the range [0; 1], it is close to 0 for an ICE vehicle and close to 1 in a purely electric vehicle. Of course, for a hybrid vehicle it assumes an intermediate value and the closer it gets to 1, the greater is the potential of the hybrid powertrain [124].

The hybridization factor provides important indications for the best size of the vehicle as it binds the power outputs from the two engines and is completely independent from the performance of each source.

It is possible to summarize in a table some example of hybridization factor of the last high-performance hybrid vehicle:

	ICE Power [kW]	**EM Power [kW]**	**HF**
Ferrari LaFerrari	588	120	0.17
Mercedes Project One	558	450	0.47
Porsche 918 Spyder	447	210	0.32
M181-H	46	19.5	0.30

Table 9. Hybrid Supercars hybridization factor.

If in the past the powertrains of *supercars* and *hypercars* were characterized by a single thermal engine capable to deliver high power and torque, nowadays the research aims to downsize the internal combustion engine (smaller displacement) trying to not compromise the power delivered [125]. Consequently, it is possible to use spaces, weights and powers for the possible electric units to be added as a propulsion source.

Moreover, it is important to find the right balance between thermal and electric motorization as well as a correct battery layout in order to increase the overall performance of the car [126,127]. An electric motor capable to deliver high power requires a high input power and therefore an oversizing of the capacity of the batteries and the nominal voltage must also be sized differently. Moreover, a very powerful electric motor involve in higher production costs that could reduce the competitiveness of the entire car [128,129].

7.1 VEHICLE DESCRIPTION

The vehicle considered as reference for the development of the energy management strategy is the *Formula SAE* car of the University of Modena and Reggio Emilia. The project consists in a real hybridization exercise of the existing combustion *Formula SAE* car.

The car is an open wheel *Formula-style* prototype [130] with a wheelbase of 1540 mm, a front track of 1260 mm and a rear track of 1210 mm wide. The rims are 10” on the diameter using 7.5” wide tyres. The suspension system is composed by a *double wishbone* layout made of carbon fibre tubes. A pull-rod arrangement has been selected for the front suspension, while a push-rod solution is adopted for the rear suspension. The braking is ensured by 190 mm diameter floating disks made from hardened steel, chosen and dimensioned to be packed in the 10’’ rims. Aluminium brake calipers has been adopted and equipped with 4 and 2 pistons, front and rear respectively. A brake bias, mechanically adjustable from the cockpit, has been developed to manually adjust the brake balance.

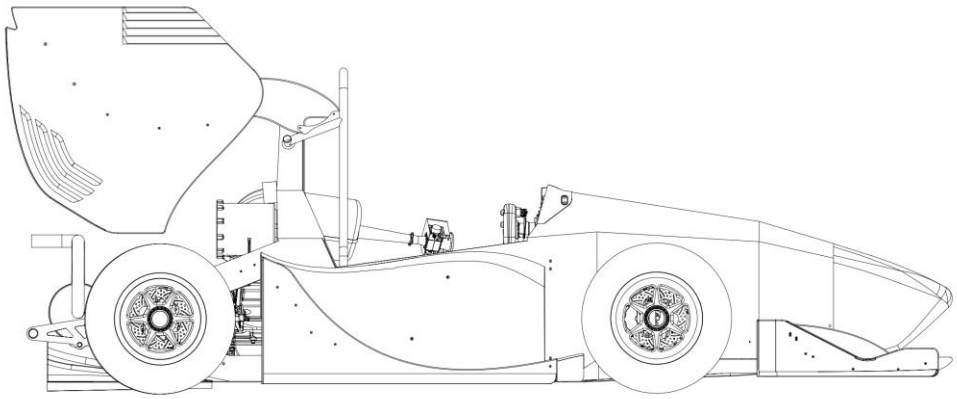

Figure 7.1. Hybrid Formula SAE car named M181-H

Moreover, the car is equipped with an aerodynamic package consisting of front wing, rear wing, undertray and sidepods. The complete aerodynamic package is capable to produce a downforce of about 430 N at 50 km/h. All these data are useful to describe the dynamic/aerodynamic model of the vehicle. Actually, only the longitudinal behaviour of the vehicle has been considered.

Just to summarize the features of the *powerunit*, the engine is assisted by a custom-developed, PMSM electric motor (30 kW), powered by a Li-Ion battery pack. The *powerunit* is mounted longitudinally in order to reduce the wheelbase and to increase the overall chassis stiffness, a property that can be exploited for improving car handling. This layout required the design of a specific bevel gear which determines a final transmission ratio of 3.3.

7.1.1 Hybrid operating modes

In the hybrid powertrain presented the engine is the primary source of power while the electric machine assists it providing extra torque when requested and serving as a generator for both braking energy recuperation and for converting fuel energy to electric to recharge the batteries. A strategy which optimize the power split [131] between the engine and electric machine has been developed in order to meet the following energy management objectives:

- Minimization of fuel consumption;
- Good driveability;
- Performance comparable to the reference vehicle;
- Battery state of charge management.

Due to limited flexibility of engine operation, it is not easy to improve the fuel economy of a parallel hybrid electric vehicles with a single electric machine from control perspective only. However, from design perspective, it is possible to recognize multiple operating modes on a powertrain system to achieve better fuel economy [132,133] and improve performance. The control strategy has to determine the power distribution between the sources at any time and for any vehicle speed.

Another important objective of the control strategy is to ensure acceptable drivability of the vehicle. Several metrics exist to quantify the driveability of a hybrid vehicle [134,135]. The vast majority of these driveability metrics focus on achieving smooth gear shifting and minimizing excessive driveline vibrations [136].

The operating modes considered are substantially four: pure thermal, power split, battery charging and regenerative braking. It is possible to define a *power-split ratio (PSR)* in order to quantify the positive power flows in the powertrain:

$$PSR = \frac{P_{ICE}}{P_{req}} \tag{7.2}$$

where P_{req} is the power request from the driver. In particular, depending on the specific operating mode, it is obtained $0 < PSR < 1$ for the power-assist

mode, $PSR = 1$ for the ICE-only mode, and $PSR > 1$ during the recharging mode [137].

Pure thermal mode

In this mode only the internal combustion engine provides energy for the traction (ICE-only). This mode is used when the thermal engine is working in a high-yield zone. So, the power delivered by the *powertrain* (PT) are:

$$\begin{aligned} P_{PT} &= P_{ICE}\,\eta_{GB}\,\eta_{BG} \\ P_{EM} &= 0 \\ P_B &= 0 \end{aligned} \tag{7.3}$$

where η_{GB} represents the efficiency of the of the gearbox depending on the gear selected and η_{BG} is the efficiency of the bevel gear transmission. The power of the electric motor (P_{EM}) and the power requested to the battery (P_B) are equal to zero in this operating mode. Actually, a minimum amount of energy is requested to get an electric motor torque close to zero, thus both P_{EM} and P_B will never be exactly null [138,139].

Power-split mode

In this mode both the electric power and thermal power are combined in order to provide the power request for propulsion. The power demands to the individual sources are:

$$\begin{aligned} P_{PT,ICE} &= P_{ICE}\,\eta_{GB}\,\eta_{BG}\,PSR \\ P_{PT,EM} &= P_{EM}\,\eta_{ch}\,\eta_{GB}\,\eta_{BG}\,(1 - PSR) \\ P_B &= \frac{P_{EM}}{\eta_e} \end{aligned} \tag{7.4}$$

where η_{ch} is the mechanical efficiency of transmission chain which connects the electric motor to the engine and η_e represents the electric efficiency of the energy conversion between the batteries and the electric motor including the efficiency of the battery itself [140]. The total power of the *powertrain* is defined as the sum of the contribute of the ICE power and the one due to the EM power:

$$P_{PT} = P_{PT,ICE} + P_{PT,EM} \tag{7.5}$$

Battery charging

In this case the power delivered by the internal combustion engine exceed the power request. Therefore, the power surplus is absorbed by the electric motor and converted in electric power. Hence, in this case the EM operates as a generator recharging the batteries. Similarly, the power subdivision to each source is described as follow:

$$P_{PT,ICE} = P_{ICE}\,\eta_{GB}\,\eta_{BG}\,PSR$$

$$P_{EM} = P_{ICE}\,\eta_{ch}\,(1 - PSR) \tag{7.6}$$

$$P_B = P_{EM}\,\eta_e$$

Note that in this operating mode the *power-spit ratio* is greater than one ($PSR > 1$). Then, the P_{EM} results to be negative because the electric motor is absorbing energy. In this case P_B represents the power delivered to the batteries and not the power requested. Actually, these values strictly depend on the state of charge (SOC) of the battery. In fact, if the SOC results to be above a certain threshold, it is not possible to deliver additional energy to the battery [141,142].

Regenerative braking

In this mode, which is used whenever it is necessary to slow down the vehicle, the electric motor operates as a generator absorbing the necessary power for braking by effectively slowing down the vehicle without using the brakes. The maximum braking power corresponds to the maximum power of the electric motor (without considering efficiency) [143]. Below is the power of each source:

$$P_{ICE} = 0$$

$$P_{EM} = P_{BRAKE}\,\eta_{GB}\,\eta_{BG}\,\eta_{ch} \tag{7.7}$$

$$P_B = P_{EM}\,\eta_e$$

where P_{BRAKE} is the power needed to brake the vehicle. When the required braking power exceeds the maximum power of the EM the brakes will be activated in order to provide the power lack. However, sometimes it is not possible to brake the vehicle using only the electric motor for many reasons: regulation restriction, safety reasons or simply because the SOC is above a certain threshold during the braking not allowing the energy storage [144]. Consequently, the effective power delivered to the EM depends on the mechanical brake power. In fact, most parallel hybrid electric vehicles employ both a hydraulic braking system and a regenerative braking system in order to improve braking performance and energy regeneration. The control of both systems has to meet the requirements of the vehicle longitudinal braking performance and gets more regenerative energy charge back to the battery. In addition, several modern strategies are developed in order to assist the driver during an emergency breaking providing an *Anti-lock Braking System* (ABS) implemented by the cooperation of both systems [145,146]. Moreover, an aspect not to ignore is about learning what drivers need to feel confident during braking events [147,148].

7.2 EQUIVALENT CONSUMPTION MINIMIZATION STRATEGY (ECMS)

The theory behind ECMS is well known in the energy management for hybrid electric vehicle. It was proposed a few years ago as a possible approach to optimize the energy flowing through the vehicle. Different works in literature discussed and further developed this method [149], and in the following a particular ECMS formulation called *A-ECMS* (*Adaptive-ECMS*) is described [150,151]. The main idea of ECMS is to minimize a function that takes into account both the energy coming from the fuel and from the battery, formulated as follows:

$$\begin{aligned} \dot{m}_{eq}(t) &= \dot{m}_f(t) + \dot{m}_{bat}(t) = \\ &= \dot{m}_f(t) + \frac{s}{Q_{LHV}} P_{bat}(t) \end{aligned} \tag{7.8}$$

where $\dot{m}_f$ is the instantaneous fuel consumption of the engine, $\dot{m}_{bat}$ is the fuel consumption equivalent to the used electrical power, P_{bat} is the electrical power demanded at a certain instant, Q_{LHV} is the fuel lower heating value (energy content for mass unit) and s is the equivalent factor, which is used to convert the electrical power from the battery into equivalent fuel consumption [152]. The power requested to the battery can be either positive or negative and, consequently, the equivalent fuel consumption can be higher or lower than the real one.

Defining SOC as the State Of Charge of the battery it is possible to write:

$$\dot{SOC}(t) = f(SOC, u, t) = -\frac{I_{bat}(SOC, u, t)}{Q_{bat}} \tag{7.9}$$

where u is the control action, I_{bat} is the battery current and Q_{bat} is the capacity of the battery. Then, it is possible to define the *Hamiltonian* of the optimal control problem, which has to be minimized:

$$H(SOC, u, \lambda, t) = -\lambda(t) * f(SOC, u, t) + \dot{m}_f(u, t) \tag{7.10}$$

The co-state variable $\lambda(t)$ is the solution of:

$$\dot{\lambda}(t) = -\lambda(t) \frac{\partial f(SOC, u, t)}{\partial SOC} \tag{7.11}$$

In other words, the *Hamiltonian* is the total equivalent fuel consumption including the electric energy. To better understand the meaning of $\lambda(t)$, an auxiliary variable can be introduced, the equivalent factor $s(t)$, formulated as follow:

$$s(t) = -\lambda(t) \frac{Q_{LHV}}{P_{bat}(t)} \tag{7.12}$$

here $P_{bat}(t)$ is the power request to the battery and Q_{LHV} is the lower heating value of the fuel. Finally, the instantaneous equivalent fuel consumption is:

$$H(SOC,u,\lambda,t) = \dot{m}_{eq}(SOC,u,s,t) = \\ = -s(t)\frac{P_{bat}(t)}{Q_{LHV}} f(SOC,u,t) \ldots + \dot{m}_f(u,t) \tag{7.13}$$

The optimal control action is the one that satisfies:

$$u^*(t) = argmin_u\, H(SOC,u,\lambda,t) \tag{7.14}$$

The optimal control depends on the value of $s(t)$, but this is unknown a priori and this makes the strategy sub-optimal.

Equivalent factor

Physically, the equivalent factor represents the "*cost*" of the energy stored in the battery, so if it has a high value, then it is preferable to use the engine and recharge, while if it is low, it's better to use electrical traction [153].

In this work, an *A-ECMS* approach has been adopted, with adaptation on feedback values. The formulation of $s(t)$ has two contributions:

- adaptive term, which is related, in this case, to the feedback of the previous SOC (square brackets);
- penalty function that corrects the value of s when it is close to the maximum and minimum accepted values (first curly brackets).

It is defined as follows:

$$s(t) = \left\{1 - k_p\left[\frac{SOC(t) - \frac{SOC_{max}+SOC_{min}}{2}}{\frac{SOC_{max}-SOC_{min}}{2}}\right]^3\right\} \ldots \\ * \left[k_a\left(SOC_{ref} - SOC(t)\right) + \left(\frac{s_{k-1}+s_{k-2}}{2}\right)\right] \tag{7.15}$$

Mode	Split factor	ICE	EM
ICE only	$u^* = 0$	ON	OFF
Boosting	$0 < u^* < 1$	ON	ON
Battery Recharge	$u^* > 0$	ON	OFF
Regenerative Braking	$u^* = 1$	OFF	ON

Table 10. Split factor strategies.

where $SOC(t)$ is the actual state of charge, SOC_{max} and SOC_{max} are the *SOC* upper and lower limits defined by the developer, SOC_{ref} is the target value, s_{k-1} and s_{k-2} are the values of s used in two previous time intervals, between two adaptation steps. While, k_p and k_a are two gain parameters used to tune the strategy.

7.2.1 State Of Charge management strategy

The *State of Charge* management strategies are the diverse ways the controller has for planning the battery usage along the driving mission. To provide a common ground for comparison, all the ones that are presented and discussed in the following paragraphs have been obtained manipulating the expression of the mentioned equivalent factor s [154,155]. In this work two different SOC management strategies have been studied: *charge sustaining* and *charge blended*.

Charge Sustaining

A *Charge-Sustaining* (CS) management strategy consists of aiming to keep the SOC level around a target defined by the developer. This strategy is widely common for HEVs, since a minimum power is available every time.

ECMS controller used in this work was designed for HEVs and it sustains the charge around a SOC target (SOC_{ref}), as can be seen in the second term of formulation (Equation (7.15)). Therefore, CS strategy is already implemented in the controller and it is the default battery usage policy.

Charge blended

The last SOC management strategy is called *Charge-Blended* (CB) and has been studied in different works. Even this approach is designed for *Plug-in* HEVs and it basically has the same formulation as CS strategy, apart from the SOC target which decreases linearly with the driven distance, as clarified in the following expression:

$$SOC_{ref}(t) = SOC_i + \frac{x}{x_f}\left(SOC_f - SOC_i\right) \tag{7.16}$$

Where SOC_{ref} is the SOC reference, SOC_i is the initial SOC, SOC_f is the desired SOC at the end of the driving mission, x is the actual driven distance and x_f is the supposed trip distance [156].

A decreasing SOC reference value is suitable for example in a race condition because usually the batteries are fully charged at the beginning of the driving mission and aim to arrive with a low SOC level at the end.

7.3 SIMULINK MODEL

In this section a description of the Simulink model is introduced for the developing of the hybrid *powerunit*. With the improvement of the efficiency and flexibility of the code, this is becoming increasingly widely adopted for production systems, as well as being a tool for the design of integrated systems due to its flexibility and ability to quick iteration.

The templates for all the devices that constitute the powertrain is introduced, including: the HEV model functioning with the different operating modes; the thermal engine model to estimate fuel consumption; the model of the electric machine that cooperates with the propulsion; the battery model to estimate

the continuity in the state of charge and the efficiency of the choice of the hybridization factor. Finally, the transmission model that includes the torque divider, which is essential to implement parallel technology, gearbox and finally differential. There is also a dedicated section for longitudinal dynamics of the vehicle that leads to calculation of the traction forces considering all the frictions and aerodynamics resistance.

In the following the model layout is analysed starting from the upper system (main level) and going into the different subsystems, focusing on the different components set up.

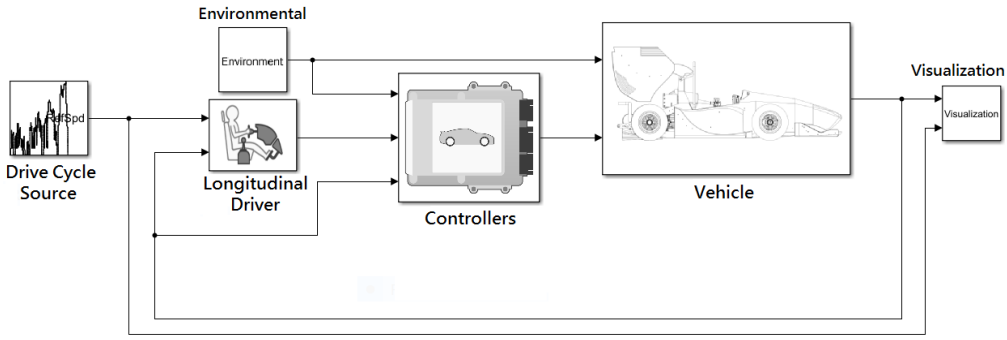

Figure 7.2. Simulink model main level layout.

In the Figure 7.2 are represented the main system block as follow:

- *Drive Cycle Source*: where is possible to set up the different Vehicle operation test speed, for example an homologation cycle, the track speed or a wide open throttle acceleration;
- *Longitudinal Driver*: it includes a PI controller, the idea is to impose a velocity profile and the PI regulator tries to follow it as much as possible, trying to reproduce the real driver behaviour;
- *Environment*: where all the parameters like the temperature, slope of the road, friction coefficient, wind velocity are set up;
- *Controllers*: this block is the core of the model, where are implemented the *Engine Control Module* (ECM), the *Hybrid Control Module* (HCM) and the *Transmission Control Module* (TCM);
- *Vehicle*: this part is formed by the *Engine*, the *Electric plant* and the *Drivetrain*;
- *Visualization*: this block was created to have a real time direct feedback of the most significant variables.

7.3.1 Drive Cycle Source

Drive cycles are graphical and numerical representations of the speed in function of the time. The purpose of this block is to provide a target velocity profile to the driver block, modelled by a PI controller.

Driving Cycles were introduced to provide a fast and unified way for car manufacturers to calculate consumption. They were designed to represent the

classic urban, suburban and combined routes [157,158]. For example, the reference European driving cycle for *light-duty* vehicle is the *WLTC* (Worldwide harmonized Light-duty vehicles Test Cycle).

However, the following simulation of the vehicle energy management are referred to a real circuit in order to measure and improve the performance of the entire vehicle. In particular, the Silverstone circuit has been taken in to account as a reference circuit. In fact, the Formula SAE (UK) event takes place on the Silverstone circuit located next to the Northamptonshire villages in UK. The Silverstone track is considered as the *'Temple of Motorsport'*. However, the circuit considered represents a variant of the main circuit. The *Formula SAE* race is held on a windy track mostly obtained on the *Copse* corner of the main circuit delimited with cones.

The circuit is long about 1 km and the race consists of 22 lap while the maximum speed reached is about 100km/h.

For the simulation of the lap time, reference is made to a set of telemetry data, recorded at high frequency (every 10 ms) on the reference Combustion Vehicle (CV), during a recent Endurance event (Figure 7.3). Among all these data (including vehicle speed, engine rotational speed and selected gear), one lap is taken as a reference. This calculation should not be intended as an accurate prediction of the actual total Endurance time, since it does not consider that the first laps of each driver are slower than the following ones, due to a number of practical reasons (the most important one is the driver's need of building up his confidence with the car and the track).

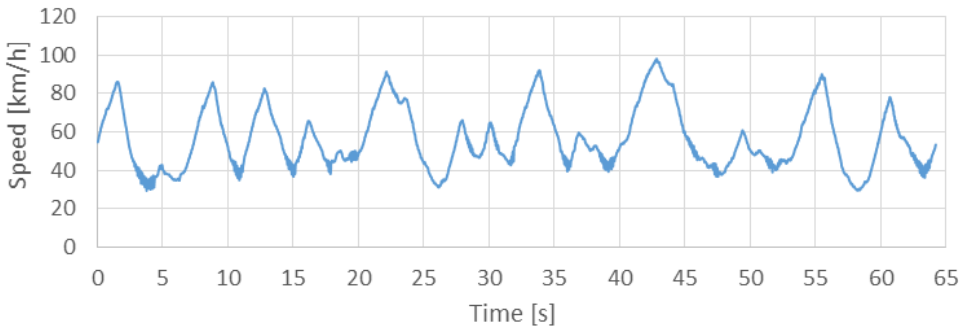

Figure 7.3. Telemetry speed of the reference vehicle on the Silverstone track.

However, considering an imposed velocity profile derived from the telemetry data, it leads to a fixed total time. Consequently, the reference lap may be split into three different types of parts: acceleration (highlighted in red, in Figure 7.4); braking (highlighted in blue, in Figure 7.4); low speed, or cornering (highlighted in yellow, in Figure 7.4). There are 13 acceleration and braking sectors, 12 low speed tracts.

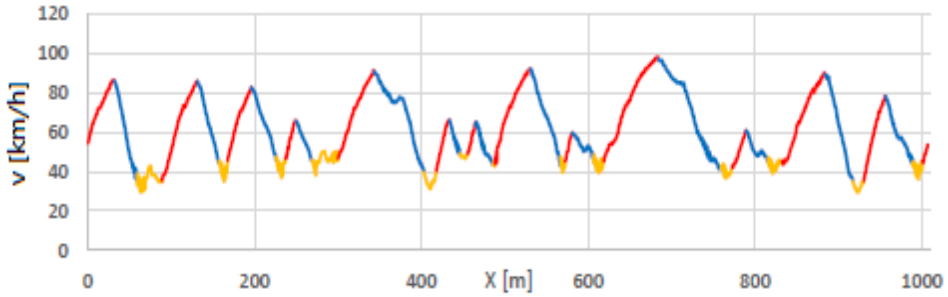

Figure 7.4. Telemetry speed of the rebuild circuit.

7.3.2 Longitudinal Driver

In this model the driver is modelled by a PI controller which takes into account the longitudinal velocity profile but not the lateral behaviour of the car.

In the Figure 7.5 it is possible recognize the most important signals generated towards the Controllers block such as the pedal acceleration and deceleration, which affects the *Engine Control Module* (ECM), the *Hybrid Control Module* (HCM) and the *Transmission Control Module* (TCM).

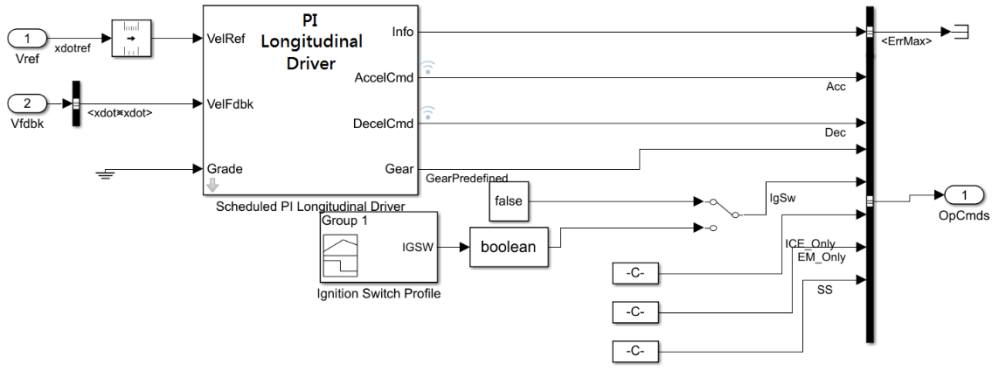

Figure 7.5. Longitudinal Driver subsystem layout.

7.3.3 Environment

This block defines the external conditions needed for the simulation such as ambient temperature, ambient pressure, slope of the road, friction coefficients and wind velocity. The *Environment* block is connected, so it directly affects the *Controllers* and *Vehicle* blocks.

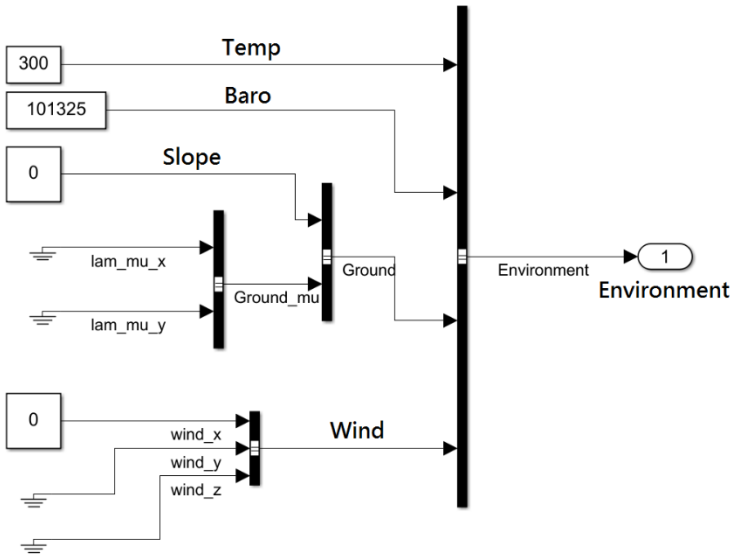

Figure 7.6. Environment subsystem layout.

7.3.4 Controllers

The *Controllers* system is the real core of the model, in fact it is composed by three different units: the *Engine Control Unit*, the *Hybrid Control Unit* and the *Transmission Control Unit*. The inputs channels come from the *Environment* block, the *Longitudinal Driver* block and the *Vehicle*. The latter includes the feedback signals, such as all the ICE and EM information (torque, speed, consumptions, SOC, etc.) and vehicle speed information. Among the outputs it is possible to identify the ICE and the EM torque demand.

The *Controllers* model structure is shown in the Figure 7.7 below, the interaction between the three subsystems is defined by the *Hybrid Control Module*.

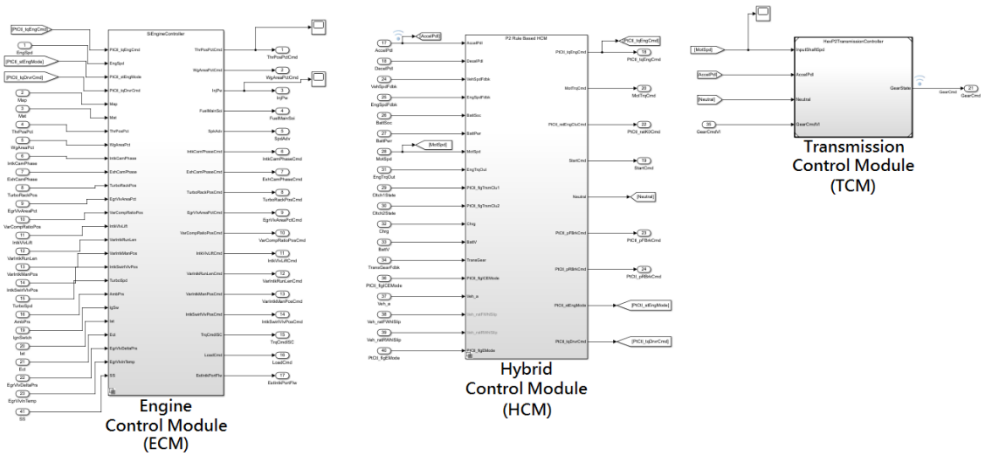

Figure 7.7. Powertrain controller modules: Engine Control Module (ECM) on the left, Hybrid Control Module (HCM) in the middle and Transmission Control Module (TCM) on the right.

The most interesting interaction is between the *Hybrid Control Module* and the *Engine Control Module*, in fact the variables in input in the *ECM* are coming out from the first part of the control iteration of the *HCM*.

In the following the different controller system is analysed, as the *Engine Control Module*, the *Transmission Control Module* and the *Hybrid Control Module*.

Engine Control Module (ECM)

The *Engine Control Module* delivers to the engine hardware the torque demand elaborating and modifying it after the first control step in the *Hybrid Control Module*, in particular in the A-ECMS part where torque split between the engine and the electric motor is decided.

For the engine controller modelling an interchangeable set of variables has been chosen, this is made for the easiness of changing different concepts of controller. The most significant variables in order to understand the nature of this control are:

- *EngSpd*: this variable reports the actual engine speed in order to have a better understanding of what the engine is capable to do in terms of acceleration and deceleration from a physical point of view;
- *PtCtl_stEngMode*: this variable arrives from the hybrid ECMS supervisory control and decides the engine modality, so to switch off/on the engine, to make it idling or to make it delivering torque;
- *PtCtl_tqEngCmd*: this variable is the most significant in terms of hybrid strategy because is the direct signal coming from the A-ECMS torque split logic and it is the real core of this model goal.

Transmission Control Module (TCM)

The Transmission Control Unit is designed for the necessity of having a direct action on the desired performance, also controlling *Gearbox* unit.

This block provides the gear selection considering the specific criteria adopted: maximise the acceleration of the vehicle or minimize the fuel consumption [159]. Moreover, the gear selection depends on vehicle and engine speed as well as depends on the hybrid operating mode. In particular, the strategy for the upshift and downshift logic is based on the input shaft speed, signal of the pedals, the neutral signal and the different operating modes.

The logic of the gear shifting is managed using a *Stateflow machine* tool normally used for coding purposes. It is possible to build different block collecting the conditions regarding the engine and electric motor functioning and connect these different blocks with conditions to be respect or not. An example could be the classic conditions in every type of codes: *if, do, undo, then, for*. The condition that determines the different *gear status* is a function defined as *Upshift* and *Downshift*. The *Upshift* function is designed like a speed threshold map that is defined by the transmission modelling. The thresholds are different depending on the shaft speed, pedal position (accelerator) and selected operating mode.

Hybrid Control Module

The *Hybrid Control Module* is the most important part of the whole model because it includes the real HEV modelling. The idea behind the energy management is the *split factor* according with the A-ECMS logic strategy. The A-ECMS calculation block is implemented with the same process and mathematics calculation shown in the section 7.2.

The decision of the engine intervention is governed by an optimal split factor between the ICE and the EM.

A dedicated subsystem is needed for the $s(t)$ calculation, considering the necessity of having different battery behaviour according with the different operating modes.

The $s(t)$ factor tuning is the real controller calibration goal in order to adapt the hybrid strategy for a better track application (in this case). This feature is added in the *cost factor* calculation by the SOC strategy block.

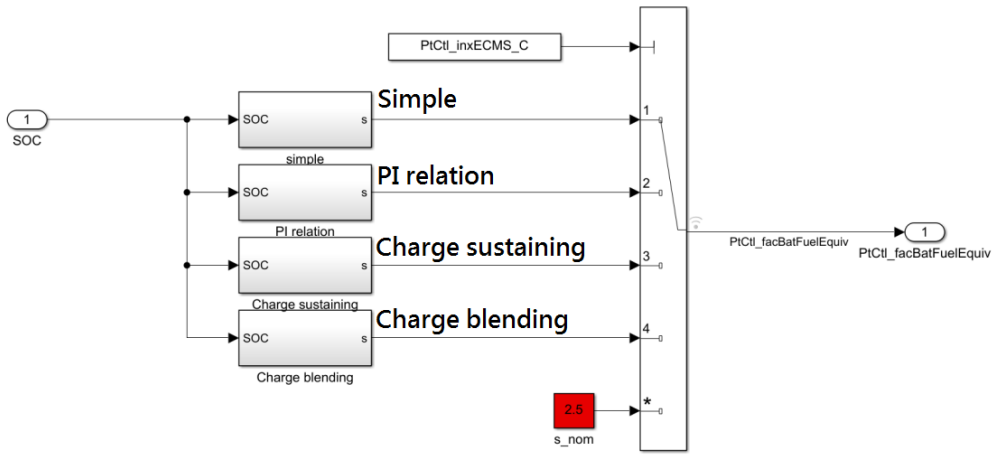

Figure 7.8. s(t) calculation strategy.

In the Figure 7.8 above are implemented the four options, the options are:

- *Simple mode*: an upper and lower limit are set for the SOC and two Charging and Discharging correction factors;
- *PI mode*: a PI regulator is set in order to define the $s(t)$ factor;
- *Charge sustaining mode*: the $s(t)$ factor is evaluated using the Equation (7.15).
- *Charge blended*: the $s(t)$ factor is evaluated using the same formula apart from the SOC target, which decreases linearly with the driven distance (equation (7.16)).

7.3.5 Vehicle

This block consists of the powertrain hardware system, starting from the engine and the electric motor to the wheels passing through the gearbox and the differential obtaining the whole vehicle model. In particular, the block is subdivided in three different subsystems: the first system is the Internal

Combustion Engine, the second is the Electric Plant and the third is the Transmission and Car block (Figure 7.9).

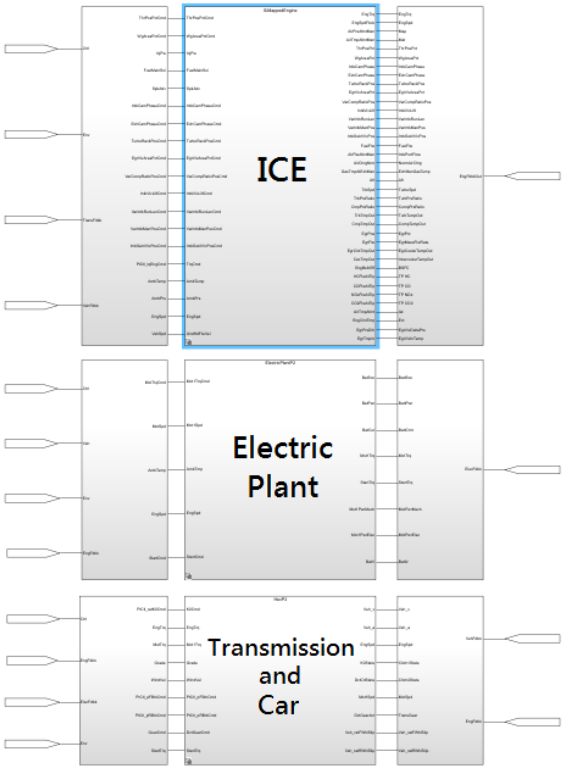

Figure 7.9. Vehicle system layout.

In the following each of these blocks are analysed, considering also the subsystems.

Internal Combustion Engine

The engine block is modelled using a mapped approach where the inputs are the engine speed (x axle) and the torque request (y axle), and the output is the torque that the engine effectively can deliver. Hence, the block contains the map of the torque deliverable in each condition as well as the map of the engine efficiency. For this specific application these maps have been obtained performing a dedicated experimental campaign at dynamometer bench.

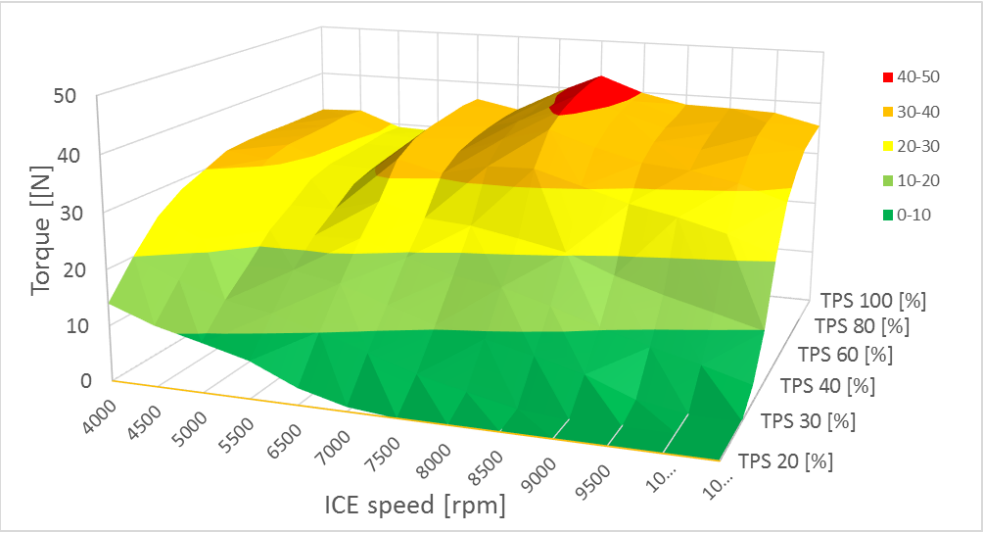

Figure 7.10. Experimental torque map of the Ducati engine.

Electric Plant

The *Electric Plant* system mainly consists of two components: the battery and the Electric Motor. The battery block is set up with a standard system tool but is also possible to use an alternative method based on experimental data (in order to have a feedback in the real world). In this moment the experimental measurements are ongoing, so a standard system tool is temporarily considered (Figure 7.11).

Battery

The battery is defined starting from the number of series and parallels that compose the battery pack, as described in the section **Errore. L'origine riferimento non è stata trovata.**. In the standard setup the battery is modelled as shown in the Figure 7.11, in which the inputs are the battery current and the battery temperature (constant in this case). Considering a mapped approach, the battery State of Charge and Voltage are instantaneously calculated.

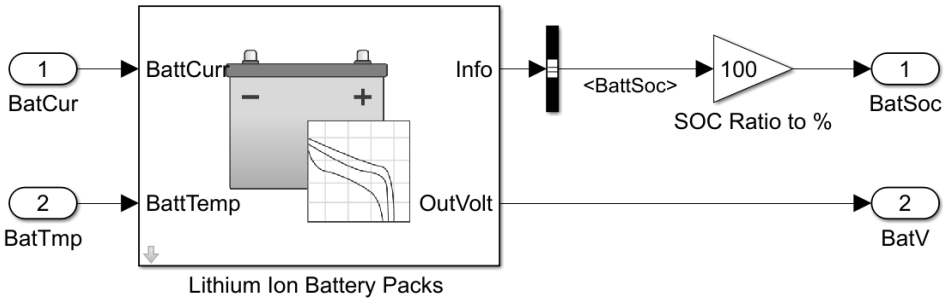

Figure 7.11. Battery standard tool model.

The important thing to focus on is the correlation between the State of Charge (%), the Peak and Continuous current value (A) and battery internal resistance (Ohm).

Electric Motor

Similarly to the ICE block, also for the *Electric Motor* a mapped approach has been considered. In particular, the inputs are the terminal voltage between the battery poles, the feedback EM speed and the EM torque request. Then, it is possible to evaluate through the maps the information regarding the losses, the actual battery current and the actual motor torque. In the Figure 7.12 the inputs and outputs layout is shown including the maps of the EM torque and EM efficiency.

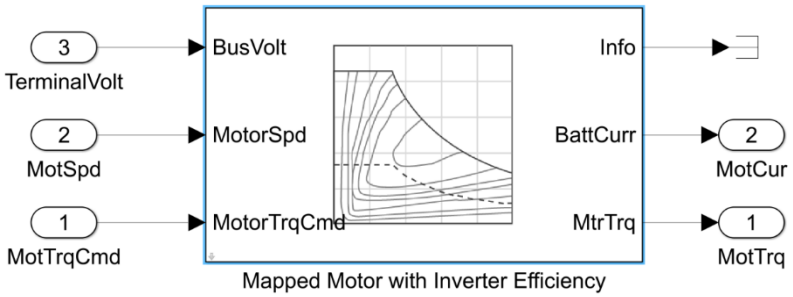

Figure 7.12. Mapped approach Electric Motor model.

Transmission and Car

In this block the hybrid drivetrain is modelled, including the gearbox, the differential, a wheels and brakes model and the vehicle model.

Gearbox

The gearbox architecture considered for this application is a four gears sequential transmission with an electro-pneumatic actuation derived from the Ducati motorcycle gearbox. It consists of two shaft which are the primary shaft connected to the ICE (and EM) and the secondary shaft connected to the bevel gear and differential.

This block has been obtained starting from a standard gearbox tool and subsequently adapted for this specific architecture.

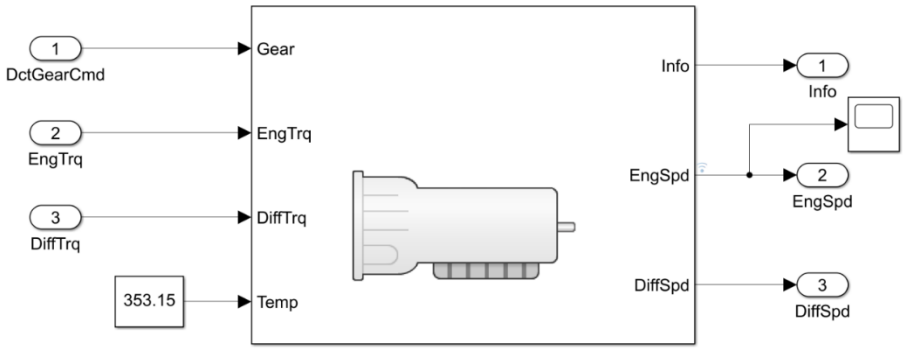

Figure 7.13. Gearbox unit subsystem.

The Figure 7.13 shows the inputs and the outputs layout. In particular, the inputs are the gear selected, the engine and the motor torque (summed) and

the differential torque (gearbox secondary shaft). While the outputs include the primary shaft speed and the secondary shaft speed.

Moreover, this block provides information about the transmission efficiency referred to each gear.

Differential

The differential block is used to represent the rear differential component which purpose is to split the torque between the right and the left wheel knowing the input shaft torque and speed. Actually, the block also includes the modelling of the *halfshaft* taking into account the axle compliance.

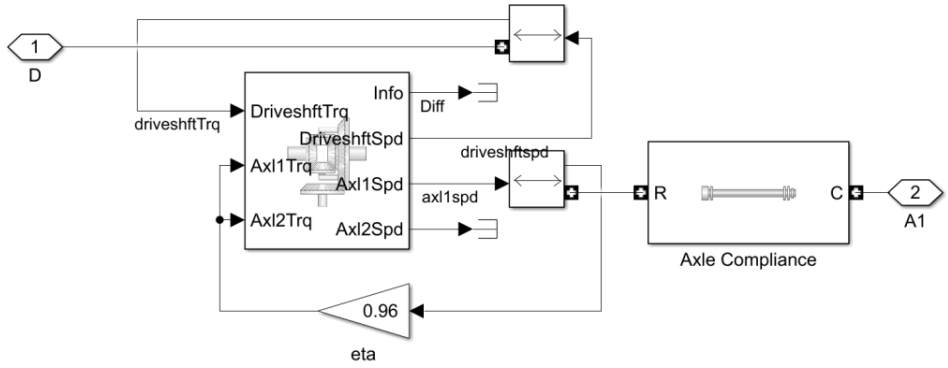

Figure 7.14. Differential and rear axle layout.

Wheels and Brakes

This block is dedicated to the wheels and brakes modelling, as shown in Figure where it is possible to recognize inputs and outputs. In particular, the inputs are the axle torque, the brake pressure, the velocity of the wheel centre and the normal force of the wheel on the ground. The outputs are the slipping factor, the longitudinal and the normal force of the wheel on the ground.

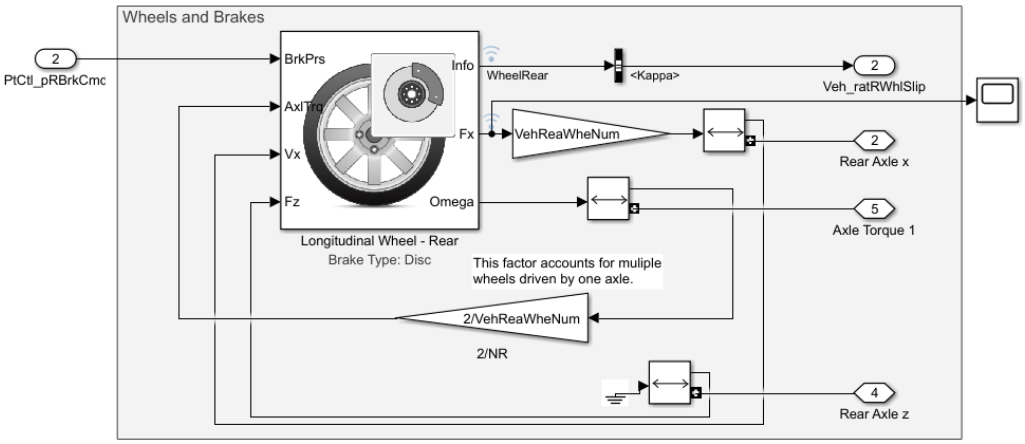

Figure 7.15. Wheels and Brakes layout.

The interaction between the wheel and the ground is modelled using the *Magic formula* by *Pacejka*, tunable by the *Bx, Cx, Dx, Ex* values [160].

The front wheels and brakes model is similar but no traction torque is considered because the vehicle is rear wheel drive.

Vehicle

In this block the dynamic behaviour of the vehicle is modelled in order to calculate the actual vehicle velocity and the feedback front and rear wheel normal forces. The inputs are the front and rear longitudinal and normal forces combined with the slope of the road and the wind velocity. In the Figure 7.16 is shown the vehicle block.

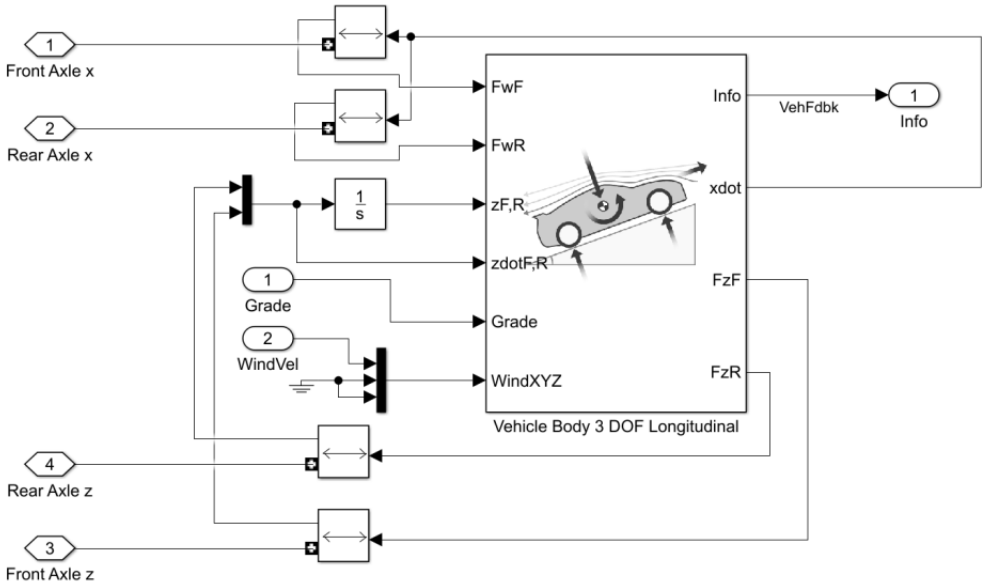

Figure 7.16. Vehicle dynamic system layout.

For simulation purposes the slope of the road and the wind velocity are set to 0, thus considering a simplified case.

7.3.6 Visualization

This block is set up for the visualization purposes and it is divided in two areas: the performance area and the emissions area.

In the performance area several information are analysed such as speeds, torques, current, State of Charge and fuel economy. In particular, the fuel economy has been estimated in two different ways: the first considering only the engine fuel consumption; the second combining the consumption between the L/100Km of the engine and the equivalent L/100Km coming from the battery energy, considering the fuel lower heating value and the fuel density [161].

Finally, in the emissions area the main pollutants are analysed including the NOx, CO, HC and CO2 mass coming from the mapped engine block system.

7.4 PERFORMANCE ANALYSIS

In this section an analysis of the hybrid vehicle performance has been carried out in terms of State of Charge of the battery and CO_2 emissions. Moreover, another important focus of this analysis consists on the performance in terms of lap time of the hybrid vehicle on the Silverstone circuit.

The lap time simulation compares two different types of vehicles: the first is the reference combustion car (referred to as CV); the second proposed hybrid car (referred to as HEV). The vehicles are identical, except for the powertrain. An additional weight due to the battery pack installed on the HEV is considered. By this way, the lap time depends only on the powertrain performance and on the overall weight of the vehicle.

The target velocity profile as a function of distance considered in the *Drive Cycle sources* is shown in Figure 7.17. In the acceleration sectors, the target velocity is very high: by this way, the *Longitudinal Driver* system tries to maximize the speed forcing the EM and the ICE to operate at maximum load, minimizing the lap time.

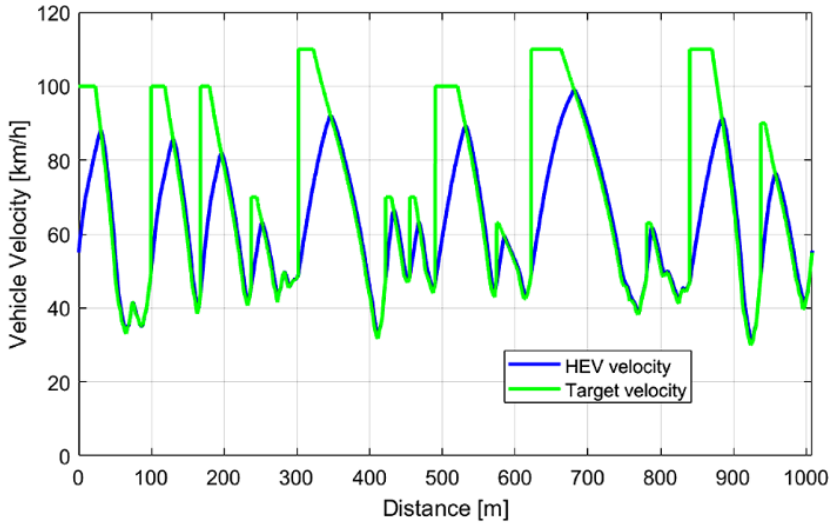

Figure 7.17. Comparison between Target velocity (highlighted in green) and HEV velocity (highlighted in blue).

During the braking phases a fraction of braking power is considered to be always provided by the mechanical brakes. As an example, approaching a low speed corner, the driver wishes to apply most of the braking moment to the front wheels, whose tyres have got a better grip, due to the load transfer during deceleration. Therefore, the braking power of the rear wheels, connected to the electric motor, is limited in order to guarantee the desired brake balance.

A further limit to the electric energy recovered by braking is the fact that the ICE cannot be decoupled from the electric motor (*P0* hybrid architecture), thus friction and pumping losses contribute to decelerate the vehicle, along with the other terms (vehicle resistance, mechanical and electrical braking). However, such high peaks of regenerative power are never available, due to the fact that

the vehicle cannot reach high speeds (the maximum length of the straights is 80 m), and at least 50% of the total power must be provided by the front brakes.

In the corners, the ICE may operate at a different load than that required by the driver: if load is higher, the additional energy can be sent to the battery; if load is lower, the EM must contribute to the traction.

Another important aspect is the comparison between the two vehicles of the emitted CO_2 during the single lap.

According to the SAE rules [9], CO_2 is calculated as:

$$CO_2[kg] = V_f[l] \cdot 2.31 + E[kWh] \cdot 0.65 \qquad (7.17)$$

where V_f is the volume of consumed fuel, in litres, and E is the net electric energy consumed by the battery, in kWh.

7.4.1 Results

The calculation of vehicle acceleration and velocity enables the prediction of the instantaneous vehicle position, calculated at each time step. From the comparison between CV and HEV velocity profiles (Figure 7.18), it can be noticed that the second vehicle is able to reach higher speeds at the end of each acceleration sector. Consequently, this result definitely involves in a decreased simulated lap time.

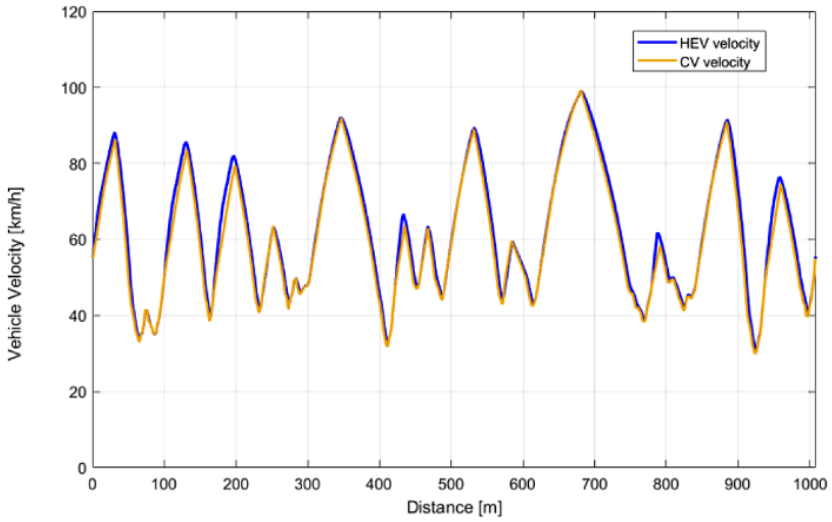

Figure 7.18. Comparison between HEV velocity (highlighted in blue) and CV velocity (highlighted in orange).

Table 11 reviews the main results of the lap time simulation. For both cases, CO_2 emissions are evaluated according to the SAE rules (Equation (7.17)). The simulation consists of the total race distance corresponding to 22 laps, about 22 km. The additional weight of HEV corresponds to the weight of the battery pack required to complete the whole race and it is sized as discussed in section **Errore. L'origine riferimento non è stata trovata.**.

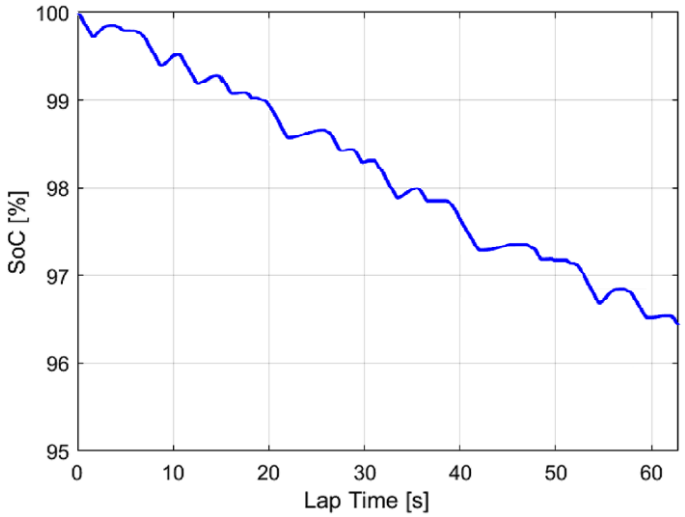

Figure 7.19. SoC trend during the lap time simulation.

The strategy considered for the battery management is the *charge blended*, described in section 7.2.1, considering a SOC_{ref} decreasing linearly during the race and reaching a value of about 20% at the end of the mission. In fact, this value represents the minimum SOC commonly accepted in order to preserve the battery life and also for safety reasons.

	CV	HEV
Reference car + driver mass [kg]	300	330
Maximum installed power [kW]	66.5	81
Maximum power / total weight [kW/kg]	0.222	0.245
Total lap time [s]	64.52	63.04
Lap time gap from CV	-	1.48
Electric Energy consumption – 22 laps [kWh]	-	3.57
Fuel consumption – 22laps [l]	3.329	2.289
CO_2 [kg]	7.690	7.608
Useful energy provided to car – 22 lap [kWh)	5.805	8.201
Specific CO_2 [kg/kWh]	1.325	0.928
Specific CO_2 [kg/kWh] (weight corrected)	1.140	0.928
Specific CO_2 reduction from CV [%]	-	20.4

Table 11. Overview of the lap simulation results for the Combustion Vehicle (CV) and Hybrid Electric Vehicle (HEV). Reference is made to a real lap of CV.

As expected, the 10.6% increase of power to weight ratio of HEV yields a relevant reduction of lap time, in comparison to CV: -1.48 s. In terms of CO_2 emissions, the reduction is less outstanding, if the absolute values are taken (-0.08 kg). However, it is observed that the useful energy provided by the powertrain to the vehicle is higher in the hybrid car, therefore the specific value of CO_2 (mass of CO_2 divided by the useful energy provided to the vehicle) should be used to get a fair comparison among the cars. The useful energy provided to

the vehicle is calculated as the time integral of the power delivered by the powertrain during accelerations and in the low speed sectors.

For this estimation, the CV useful energy is corrected, in order to consider the lower weight (300 versus 330 kg). The final result is that specific CO_2 emissions are reduced by 20.4% with HEV.

Finally, Figure 7.20 shows the operating points on the ICE efficiency map. It may be noticed that the ICE rotational speed never falls below 4000 rpm, a limit imposed by the need of a fast transient response.

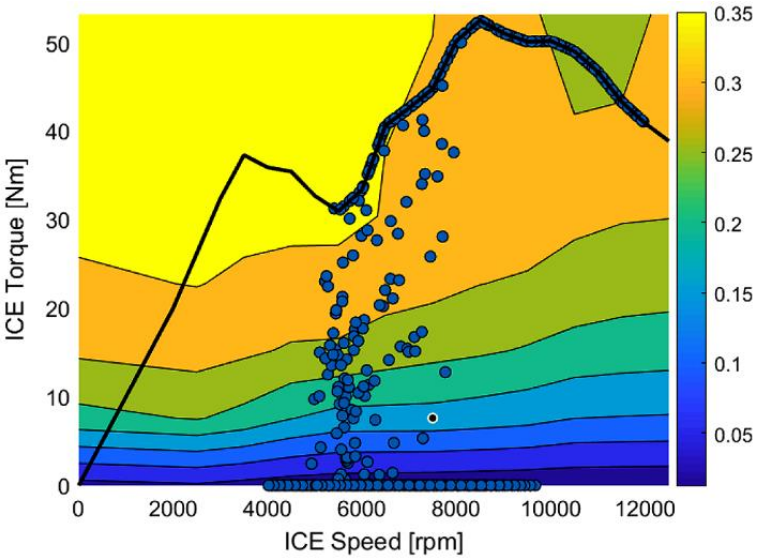

Figure 7.20. ICE operating conditions in terms of speed, torque and efficiency.

Similarly, Figure 7.21 shows the distribution of the operating points on the efficiency map of the electric machine. Due to the direct coupling between ICE and EM, the lower limit on engine speed corresponds to a minimum speed of about 3300 rpm for the EM.

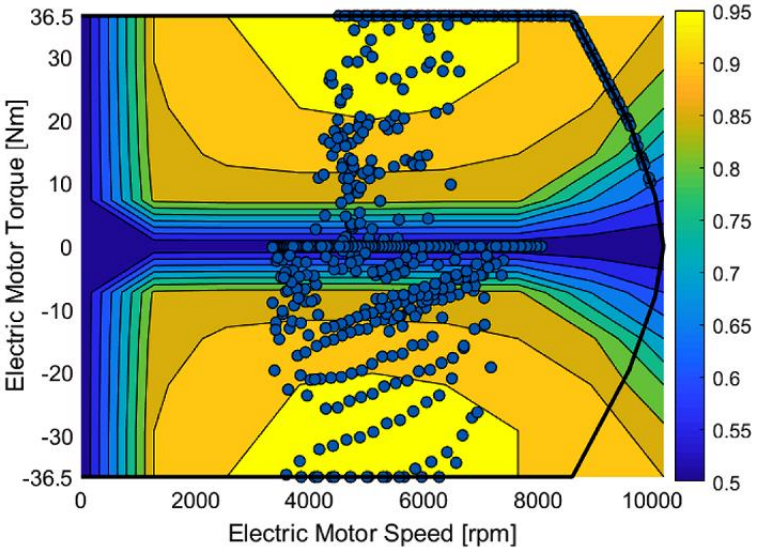

Figure 7.21. EM operating conditions in terms of EM speed, torque and efficiency.

8 CONCLUSIONS

This project focused on the design of a hybrid power unit for a small vehicle application. In particular, an unconventional hybridization solution has been presented, based on a V90 2-cylinders motorcycle engine. The proposal could even represent a real conversion kit possibly suitable for the actual motorbike itself. In fact, the design choices have been motivated in order to achieve a *plug&go* solution. The EM results to be well integrated with the ICE layout not exciding the design space of the original powertrain.

Although different solutions have been investigated, finally, it has been decided to keep the original V90 architecture of the crank mechanism (with the sole modification of the passive piston geometry in order to annul its compression capabilities) because of its natural balancing with respect to the first order inertial reciprocating forces. In fact, other balancing systems showed a comparable weight, but presented higher costs and possible reliability problems.

The dynamic behaviour of the valvetrain chain has been investigated validating the possibility of the use of the OEM timing chain as a transmission element for the EM. In fact, the differences introduced by the hybridization process change the loads acting on the chain. The torque that the chain has to manage is now determined by the interaction with the electric machine. The comparison between the new drive layout model and the *valvetrain* reference model is encouraging because the resulting maximum loads are comparable. However, the configuration with the EM led to different loading cycles. Consequently, a complete fatigue analysis should be carried out in order to obtain more detailed results that showed an acceptable minimum fatigue safety factor.

A particular focus regards the electric motor case which represents the most complicated component introduced with this project. In fact, a specific electric motor case has been designed and manufactured via Additive Manufacturing technology, in order to include the chain housing, the electric motor cooling system and the lubricating system.

A 3D-CFD analysis on the coolant circuit has been carried out to define the best design of the EM case. Among the different attempts, the layout providing a pressure drop as close as possible to the original geometry has been identified. For this selected coolant jacket, the version with two inlets to the EM cooling circuit has been preferred, to ensure a more uniform temperature of the EM housing. Finally, despite a new gasket has been designed with optimized water passages to recover the original flow rate of the circuit, the final geometry has been provided with fully-open holes, to promote EM efficiency and reduce cost and time to entry into service. The CFD simulations asserted the possibility of use the same cooling system for both EM and the ICE. This choice represents a compromise between the absolute cooling efficiency and the simplicity of realization, which further involves a compact solution.

A detailed Finite Element model has been developed in order to assess the EM case strength via a thermo-structural analysis. Results showed maximum stresses below the yield stress of the material thus ensuring a suitable mechanical behaviour of the assembly.

A Simulink model has been developed in order to assess the performance of the hybrid *powerunit*, and reference is made to a recorded lap of the Combustion Vehicle (CV). In particular, the results showed a relevant reduction of the lap time, in comparison to CV (-1.48 s), mostly due to the 10.6% increase of the power to weight ratio of HEV. Moreover, this solution also led to a reduction of the specific CO_2 emissions of about 20.4% with respect to the CV.

ABBREVIATIONS

ICE	internal combustion engine
EM	electric motor
ZEV	zero emission vehicle
BEV	battery electric vehicle
ICEV	internal combustion engine vehicle
HEV	hybrid electric vehicle
LDV	light-duty vehicle
CFD	computational fluid dynamic
HTC	heat transfer coefficient
VSI	voltage source inverter
ESS	energy storage system
SLI	starting-lighting-ignition
LCO	lithium cobalt oxide
LMO	lithium manganese oxide
NMC	(lithium) nickel manganese cobalt
NCA	(lithium) nickel cobalt aluminium
LFP	lithium ferro phosphate
LTO	lithium titanium oxide
BMS	battery management system
IM	induction motor
PMSM	permanent magnet synchronous motor
SRM	switched reluctance motor
VVVF	variable-voltage variable-frequency
PCV	positive crankcase ventilation
TKE	turbulent kinetic energy
AM	additive manufacturing
SLM	selective laser melting
DFM	design for manufacturing
FE	finite element
OEM	original equipment manufacturer
DOE	design of experiment
CAD	computer aided design

DOF	degree of freedom
HF	hybridization factor
PSR	power split ratio
ABS	anti-lock brake system
SOC	state of charge
ECMS	equivalent consumption minimization strategy
A-ECMS	adaptive - equivalent consumption minimization strategy
CS	charge sustaining
CB	charge blended
ECM	engine control module
HCM	hybrid control module
TCM	transmission control module

REFERENCES

1. Chapman, L., “Transport and climate change: a review,” *J. Transp. Geogr.* 15(5):354–367, 2007, doi:10.1016/j.jtrangeo.2006.11.008.
2. Saboori, B., Sapri, M., and Baba, M. bin, “Economic growth, energy consumption and CO2 emissions in OECD (Organization for Economic Co-operation and Development)’s transport sector: A fully modified bi-directional relationship approach,” *Energy* 66:150–161, 2014, doi:10.1016/j.energy.2013.12.048.
3. Fontaras, G., Zacharof, N.G., and Ciuffo, B., “Fuel consumption and CO2 emissions from passenger cars in Europe – Laboratory versus real-world emissions,” *Prog. Energy Combust. Sci.* 60:97–131, 2017, doi:10.1016/j.pecs.2016.12.004.
4. Hawkins, T.R., Gausen, O.M., and Strømman, A.H., “Environmental impacts of hybrid and electric vehicles-a review,” *Int. J. Life Cycle Assess.* 17(8):997–1014, 2012, doi:10.1007/s11367-012-0440-9.
5. Zdeněk, Č. and Pavel, M., “Electric, hybrid electric and combustion engine driven cars and their impact on environment,” *Proc. 2011 14th Eur. Conf. Power Electron. Appl. EPE 2011* 739–743, 2011.
6. González Palencia, J.C., Furubayashi, T., and Nakata, T., “Energy use and CO 2 emissions reduction potential in passenger car fleet using zero emission vehicles and lightweight materials,” *Energy* 48(1):548–565, 2012, doi:10.1016/j.energy.2012.09.041.
7. Kim, N. and Rousseau, A., “Assessment by Simulation of Benefits of New HEV Powertrain Configurations,” *Oil Gas Sci. Technol. – Rev. d’IFP Energies Nouv.* 68(1):79–93, 2013, doi:10.2516/ogst/2013107.
8. Weiss, M., Bonnel, P., Hummel, R., Provenza, A., and Manfredi, U., “On-road emissions of light-duty vehicles in Europe,” *Environ. Sci. Technol.* 45(19):8575–8581, 2011, doi:10.1021/es2008424.
9. IMechE website, http://www.imeche.org/events/formula-student/team-information/rules, Feb. 2019.
10. Sciarretta, A., Back, M., and Guzzella, L., “Control of Parallel Hybrid Electric Vehicles,” *IEEE Trans. Control Syst. Technol.* 12(3):352–363, 2004, doi:10.1109/TCST.2004.824312.
11. Chan, C.C., “The State of the Art of Electric, Hybrid, and Fuel Cell Vehicles With their superior fuel economy and performance, hybrid vehicles will likely increase in popularity in coming years; further development of control theory for hybrids is essential for their,” *Fellow IEEE* 95(4):704–718, 2007, doi:10.1109/JPROC.2007.892489.
12. Çağatay Bayindir, K., Gözüküçük, M.A., and Teke, A., “A comprehensive overview of hybrid electric vehicle: Powertrain configurations, powertrain control techniques and electronic control units,” *Energy*

Convers. Manag. 52(2):1305–1313, 2011, doi:10.1016/j.enconman.2010.09.028.

13. Lo, E.W.C., "Review on the configurations of hybrid electric vehicles," *2009 3rd Int. Conf. Power Electron. Syst. Appl. PESA 2009* 1–4, 2009.

14. Fellini, R., Michelena, N., Papalambros, P., and Sasena, M., "Optimal design of automotive hybrid powertrain systems," *Proc. - 1st Int. Symp. Environ. Conscious Des. Inverse Manuf. EcoDesign 1999* 400–405, 1999, doi:10.1109/ECODIM.1999.747645.

15. Chan, C.C., Bouscayrol, A., and Chen, K., "Electric, hybrid, and fuel-cell vehicles: Architectures and modeling," *IEEE Trans. Veh. Technol.* 59(2):589–598, 2010, doi:10.1109/TVT.2009.2033605.

16. M. Sabri, M.F., Danapalasingam, K.A., and Rahmat, M.F., "A review on hybrid electric vehicles architecture and energy management strategies," *Renew. Sustain. Energy Rev.* 53:1433–1442, 2016, doi:10.1016/j.rser.2015.09.036.

17. Liu, W., "Hybrid Electric Vehicle System Modeling and Control," 2017.

18. Wyczalek, F.A., "Hybrid electric vehicles (EVS-13 Osaka)," *Northcon - Conf. Rec.* 409–412, 1996, doi:10.1109/northc.1996.564972.

19. Emadi, A., Rajashekara, K., Williamson, S.S., and Lukic, S.M., "Topological overview of hybrid electric and fuel cell vehicular power system architectures and configurations," *IEEE Trans. Veh. Technol.* 54(3):763–770, 2005, doi:10.1109/TVT.2005.847445.

20. Ross, M. and Wu, W., "Fuel economy analysis for a hybrid concept car based on a buffered fuel-engine operating at an optimal point," *SAE Tech. Pap.* (41 2), 1995, doi:10.4271/950958.

21. Solouk, A. and Shahbakhti, M., "Modeling and Energy Management of an HCCI based Powertrain for Series Hybrid and Extended Range Electric Vehicles," *Int. J. Powertrains* 6(2):1, 2017, doi:10.1504/ijpt.2017.10001761.

22. Gökce, K. and Ozdemir, A., "An instantaneous optimization strategy based on efficiency maps for internal combustion engine/battery hybrid vehicles," *Energy Convers. Manag.* 81:255–269, 2014, doi:10.1016/j.enconman.2014.02.034.

23. Yang, Y., Ali, K.A., Roeleveld, J., and Emadi, A., "State-of-the-art electrified powertrains - hybrid, plug-in, and electric vehicles," *Int. J. Powertrains* 5(1):1, 2016, doi:10.1504/ijpt.2016.075181.

24. Sai, L.W., Schultz, G., and Higuchi, N., "A novel parallel hybrid transmission," *J. Mech. Des. Trans. ASME* 123(2):161–168, 2001, doi:10.1115/1.1365118.

25. Chau, K.T. and Wong, Y.S., "Overview of power management in hybrid electric vehicles," *Energy Convers. Manag.* 43(15):1953–1968, 2002,

doi:10.1016/S0196-8904(01)00148-0.

26. Yang, Y., Hu, X., Pei, H., and Peng, Z., “Comparison of power-split and parallel hybrid powertrain architectures with a single electric machine: Dynamic programming approach,” *Appl. Energy* 168:683–690, 2016, doi:10.1016/j.apenergy.2016.02.023.

27. Amjad, S., Neelakrishnan, S., and Rudramoorthy, R., “Review of design considerations and technological challenges for successful development and deployment of plug-in hybrid electric vehicles,” *Renew. Sustain. Energy Rev.* 14(3):1104–1110, 2010, doi:10.1016/j.rser.2009.11.001.

28. Offer, G.J., Howey, D., Contestabile, M., Clague, R., and Brandon, N.P., “Comparative analysis of battery electric, hydrogen fuel cell and hybrid vehicles in a future sustainable road transport system,” *Energy Policy* 38(1):24–29, 2010, doi:10.1016/j.enpol.2009.08.040.

29. Momoh, O.D. and Omoigui, M.O., “An overview of hybrid electric vehicle technology,” *5th IEEE Veh. Power Propuls. Conf. VPPC ’09* 1286–1292, 2009, doi:10.1109/VPPC.2009.5289703.

30. Wu, G., Zhang, X., and Dong, Z., “Powertrain architectures of electrified vehicles: Review, classification and comparison,” *J. Franklin Inst.* 352(2):425–448, 2015, doi:10.1016/j.jfranklin.2014.04.018.

31. Picarelli, A. and Dempsey, M., “Simulating the complete 2014 hybrid electric Formula 1 cars,” 9.2-9.2, 2015, doi:10.1049/cp.2014.0960.

32. Limebeer, D.J.N., Perantoni, G., and Rao, A. V., “Optimal control of Formula One car energy recovery systems,” *Int. J. Control* 87(10):2065–2080, 2014, doi:10.1080/00207179.2014.900705.

33. Mattarelli, E., Rinaldini, C.A., Scrignoli, F., and Mangeruga, V., “Development of a Hybrid Power Unit for Formula SAE Application: ICE CFD-1D Optimization and Vehicle Lap Simulation,” *SAE Tech. Pap. Ser.* 1, 2019, doi:10.4271/2019-24-0200.

34. Karden, E., Ploumen, S., Fricke, B., Miller, T., and Snyder, K., “Energy storage devices for future hybrid electric vehicles,” *J. Power Sources* 168(1 SPEC. ISS.):2–11, 2007, doi:10.1016/j.jpowsour.2006.10.090.

35. Lukic, S.M., Cao, J., Bansal, R.C., Rodriguez, F., and Emadi, A., “Energy storage systems for automotive applications,” *IEEE Trans. Ind. Electron.* 55(6):2258–2267, 2008, doi:10.1109/TIE.2008.918390.

36. González, A., Goikolea, E., Barrena, J.A., and Mysyk, R., Review on supercapacitors: Technologies and materials, *Renew. Sustain. Energy Rev.* 58:1189–1206, 2016, doi:10.1016/j.rser.2015.12.249.

37. Barr, A. and Veshagh, A., “Fuel economy and performance comparison of alternative mechanical hybrid powertrain configurations,” *SAE Tech. Pap.* (724):776–790, 2008, doi:10.4271/2008-01-0083.

38. O’hayre, R., Cha, S.-W., Colella, W., and Prinz, F.B., “Fuel cell

fundamentals," John Wiley & Sons, ISBN 1119113806, 2016.

39. Budde-Meiwes, H., Drillkens, J., Lunz, B., Muennix, J., Rothgang, S., Kowal, J., and Sauer, D.U., "A review of current automotive battery technology and future prospects," *Proc. Inst. Mech. Eng. Part D J. Automob. Eng.* 227(5):761–776, 2013, doi:10.1177/0954407013485567.

40. Kwade, A., Haselrieder, W., Leithoff, R., Modlinger, A., Dietrich, F., and Droeder, K., "Current status and challenges for automotive battery production technologies," *Nat. Energy* 3(4):290–300, 2018, doi:10.1038/s41560-018-0130-3.

41. Higashimoto, K., Homma, H., Uemura, Y., Kawai, H., Saibara, S., and Hironaka, K., "Automotive Lithium-ion Batteries," 2011.

42. John T. Warner, "The Handbook of Lithium-Ion Battery Pack Design," 2015, doi:10.1016/c2013-0-23144-5.

43. Babu, S.S., Santella, M.L., Feng, Z., Riemer, B.W., and Cohron, J.W., "Empirical model of effects of pressure and temperature on electrical contact resistance of metals," *Sci. Technol. Weld. Join.* 6(3):126–132, 2001, doi:10.1179/136217101101538631.

44. Pattipati, B., Pattipati, K., Christopherson, J.P., Namburu, S.M., Prokhorov, D. V., and Qiao, L., "Automotive battery management systems," *AUTOTESTCON (Proceedings)* (September):581–586, 2008, doi:10.1109/AUTEST.2008.4662684.

45. Zeraoulia, M., Benbouzid, M.E.H., and Diallo, D., Electric motor drive selection issues for HEV propulsion systems: A comparative study, *IEEE Trans. Veh. Technol.* 55(6):1756–1764, 2006, doi:10.1109/TVT.2006.878719.

46. Ehsani, M., Gao, Y., Longo, S., and Ebrahimi, K., "Modern electric, hybrid electric, and fuel cell vehicles," CRC press, ISBN 0429998244, 2018.

47. Ehsani, M., Gao, Y., and Gay, S., "Characterization of Electric Motor Drives for Traction Applications," *IECON Proc. (Industrial Electron. Conf.* 1:891–896, 2003, doi:10.1109/IECON.2003.1280101.

48. Hanselman, D., "Brushless permanent magnet motor design," 2003.

49. Awadallah, M., Tawadros, P., Walker, P., and Zhang, N., "Selection and Characterisation of PMSM motor for mild HEV Applications," *EVS 2016-29th International Electric Vehicle Symposium*, ISBN 151083270X, 2016.

50. Yang, Z., Shang, F., Brown, I.P., and Krishnamurthy, M., "Comparative study of interior permanent magnet, induction, and switched reluctance motor drives for EV and HEV applications," *IEEE Trans. Transp. Electrif.* 1(3):245–254, 2015, doi:10.1109/TTE.2015.2470092.

51. Rahman, Z., Ehsani, M., and Butler, K.L., "An investigation of electric motor drive characteristics for EV and HEV propulsion systems," *SAE Tech. Pap.* (724), 2000, doi:10.4271/2000-01-3062.

52. Rahman, K.M. and Ehsani, M., “PERFORMANCE ANALYSIS OF ELECTRIC MOTOR DRIVES FOR ELECTRIC AND HYBRID ELECTRIC VEHICLE APPLICATIONS,” 49–56, 1998.

53. Jeongwoo, L. and Nelson, D.J., “Rotating inertia impact on propulsion and regenerative braking for electric motor driven vehicles,” *2005 IEEE Vehicle Power and Propulsion Conference, VPPC*, ISBN 0780392809: 308–314, 2005, doi:10.1109/VPPC.2005.1554575.

54. Feng, Z.M., Li, J.L., and Liu, G.W., “Dynamic Analysis of Silent Chain Drive System for Hybrid Car,” *Adv. Mater. Res.* 694–697:84–89, 2013, doi:10.4028/www.scientific.net/amr.694-697.84.

55. Meng, F., Feng, Z., and Chu, Y., “MESHING THEORY AND DESIGN_ METHOD OF NEW SILENT CHAIN AND SPROCKET,” *Chinese J. Mech. Eng. Ed.* 19(3):425–427, 2006.

56. Hoag, K. and Dondlinger, B., “Vehicular Engine Design,” 2nd ed., ISBN 9783709118580: 145–146, 2016.

57. Barbieri, S.G., Giacopini, M., Mangeruga, V., and Mantovani, S., “A Design Strategy Based on Topology Optimization Techniques for an Additive Manufactured High Performance Engine Piston,” *Procedia Manuf.* 11(June):641–649, 2017, doi:10.1016/j.promfg.2017.07.162.

58. Barbieri, S.G., Giacopini, M., Mangeruga, V., and Mantovani, S., “Design of an Additive Manufactured Steel Piston for a High Performance Engine: Developing of a Numerical Methodology Based on Topology Optimization Techniques,” *SAE Tech. Pap. Ser.* 1:1–10, 2018, doi:10.4271/2018-01-1385.

59. Mirzendehdel, A.M. and Suresh, K., “Support structure constrained topology optimization for additive manufacturing,” *CAD Comput. Aided Des.* 81:1–13, 2016, doi:10.1016/j.cad.2016.08.006.

60. Adam, G.A.O. and Zimmer, D., “On design for additive manufacturing: Evaluating geometrical limitations,” *Rapid Prototyp. J.* 21(6):662–670, 2015, doi:10.1108/RPJ-06-2013-0060.

61. Thompson, M.K., Moroni, G., Vaneker, T., Fadel, G., Campbell, R.I., Gibson, I., Bernard, A., Schulz, J., Graf, P., Ahuja, B., and Martina, F., “Design for Additive Manufacturing: Trends, opportunities, considerations, and constraints,” *CIRP Ann. - Manuf. Technol.* 65(2):737–760, 2016, doi:10.1016/j.cirp.2016.05.004.

62. Mertens, A., Dedry, O., Reuter, D., Rigo, O., and Lecomte-Beckers, J., “THERMAL TREATMENTS OF AlSi10Mg PROCESSED BY LASER BEAM MELTING.”

63. Kerbrat, O., Mognol, P., and Hascoët, J.Y., “A new DFM approach to combine machining and additive manufacturing,” *Comput. Ind.* 62(7):684–692, 2011, doi:10.1016/j.compind.2011.04.003.

64. Mukherjee, T., Zhang, W., and DebRoy, T., “An improved prediction of residual stresses and distortion in additive manufacturing,” *Comput. Mater. Sci.* 126:360–372, 2017, doi:10.1016/j.commatsci.2016.10.003.

65. Boglietti, A., Cavagnino, A., Staton, D., Shanel, M., Mueller, M., and Mejuto, C., “Evolution and modern approaches for thermal analysis of electrical machines,” *IEEE Trans. Ind. Electron.* 56(3):871–882, 2009, doi:10.1109/TIE.2008.2011622.

66. Schofield, N., Bilgin, B., Kasprzak, M., Emadi, A., Preindl, M., Nalakath, S., Sadek, H., Cotton, J., and Yang, Y., “Thermal management of electric machines,” *IET Electr. Syst. Transp.* 7(2):104–116, 2016, doi:10.1049/iet-est.2015.0050.

67. Cao, M., Kovent, I., and Ku, J., “Efficient thermal modeling and integrated control strategy of powertrain for a parallel hybrid EcoCAR2 competition vehicle,” *SAE Tech. Pap.* 1, 2014, doi:10.4271/2014-01-1927.

68. Menter, F.R., “Improved two-equation k-omega turbulence models for aerodynamic flows,” *Nasa Tm-103975* 1–31, 1992.

69. Menter, F. and Esch, T., “Elements of Industrial Heat Transfer Predictions,” *16th Brazilian Congr. Mech. Eng.*, 2001.

70. Berni, F., Fontanesi, S., Cicalese, G., and D’Adamo, A., “Critical Aspects on the Use of Thermal Wall Functions in CFD In-Cylinder Simulations of Spark-Ignition Engines,” *SAE Int. J. Commer. Veh.* 10(2):547–561, 2017, doi:10.4271/2017-01-0569.

71. Cicalese, G., Berni, F., Fontanesi, S., D’Adamo, A., and Andreoli, E., “A Comprehensive CFD-CHT Methodology for the Characterization of a Diesel Engine: from the Heat Transfer Prediction to the Thermal Field Evaluation,” *SAE Tech. Pap. Ser.* 1, 2017, doi:10.4271/2017-01-2196.

72. Fontanesi, S., Cicalese, G., Fantoni, S., and Rosso, M., “CFD Investigation of the Thermo-Mechanical Behavior of a High Performance Bike Engine,” 2011, doi:10.4271/2011-32-0525.

73. Fontanesi, S., Giacopini, M., Cicalese, G., Sissa, S., and Fantoni, S., “Numerical investigation of the cavitation damage in the wet cylinder liner of a high performance motorbike engine,” *Eng. Fail. Anal.* 44:408–423, 2014, doi:10.1016/j.engfailanal.2014.05.025.

74. Giacopini, M., Sissa, S., Rosi, R., and Fantoni, S., “Influence of different temperature distributions on the fatigue life of a motorcycle piston,” *Proc. Inst. Mech. Eng. Part D J. Automob. Eng.* 229(9):1276–1288, 2015, doi:10.1177/0954407014560201.

75. Lanchester, F.W., “ENGINE BALANCING,” 1914.

76. Sandor, G.N., “A lumped parameter approach to vibration and stress analysis of elastic linkages,” *J. Manuf. Sci. Eng. Trans. ASME* 95(2):549–557, 1973, doi:10.1115/1.3438189.

77. Shiao, Y. and Moskwa, J.J., An Investigation of Load Force and Dynamic Error Magnitude Using the Lumped Mass Connecting Rod Model, *SAE Trans.* 102:837–846, 1993, doi:10.2307/44611421.

78. Yang, C., Hao, Z., and Zheng, G., "Balance mechanism design of single cylinder engine based on continuous mass distribution of connecting rod," *Trans. Tianjin Univ.* 15(4):255–259, 2009, doi:10.1007/s12209-009-0045-y.

79. Clink and R, "BALANCING OF HIGH-SPEED FOUR-STROKE ENGINES," (2), 1958.

80. Heifetz, M. and Marsh, M., "Engine dynamics and balancing," *SAE Technical Papers*, SAE International, 1984, doi:10.4271/840914.

81. Yoshioka, T. and Sugita, H., "Noise and vibration reduction technology in hybrid vehicle development," *SAE Tech. Pap.* 114, 2001, doi:10.4271/2001-01-1415.

82. Veprik, A.M., "Vibration protection of critical components of electronic equipment in harsh environmental conditions," *J. Sound Vib.* 259(1):161–175, 2003, doi:10.1006/jsvi.2002.5164.

83. Harkness, J.R., "Methods of Balancing Single Cylinder Engines," *SAE Tech. Pap. Ser.* 77(3):2329–2338, 1968, doi:10.4271/680571.

84. Home | BMW Motorrad, https://www.bmw-motorrad.com, Dec. 2019.

85. Forcelli, A., Grasso, C., and Pappalardo, T., "The transmission gear rattle noise: Parametric sensitivity study," *SAE Technical Papers*, SAE International, ISBN 0768013194, 2004, doi:10.4271/2004-01-1225.

86. Niola, V. and Quaremba, G., "The gear whine noise," ISBN 9781618040220, 2011.

87. Ducati Supermono - Wikipedia, https://en.wikipedia.org/wiki/Ducati_Supermono, Dec. 2019.

88. Ducati Supermono | Historical Models | Ducati Heritage, https://www.ducati.com/ww/en/heritage/bikes/supermono, Dec. 2019.

89. Duncan, W.J., "A kinematic property of the articulated quadrilateral," *Q. J. Mech. Appl. Math.* 7(2):222–225, 1954, doi:10.1093/qjmam/7.2.222.

90. Grigore, J.-C. and Pandrea, N., "Algorithm and numerical calculation of undetermined static reactions to the plan articulated quadrilateral mechanism with straight bars," Dec. 2019, doi:10.26825/bup.ar.2018.014.

91. Pellicano, F., "MECCANICA APPLICATA ALLE MACCHINE."

92. Uy, M. and Telford, J.K., "Optimization by design of experiment techniques," *IEEE Aerosp. Conf. Proc.*, 2009, doi:10.1109/AERO.2009.4839625.

93. Maile, K., Campean, F., and Day, A., “Design for reliability of an engine timing chain,” *SAE Technical Papers*, SAE International, 2009, doi:10.4271/2009-01-0206.

94. Weber, C., Herrmann, W., and Stadtmann, J., “Experimental investigation into the dynamic engine timing chain behaviour,” *SAE Tech. Pap.* (724), 1998, doi:10.4271/980840.

95. Takagishi, H., Muguruma, K., Takahashi, N., and Nagakubo, A., “Analysis of effect of tensioner on chain system,” *SAE Technical Papers*, SAE International, 2008, doi:10.4271/2008-01-1496.

96. Krueger, K., Engelhardt, T., Ginzinger, L., and Ulbrich, H., “Dynamical analysis of hydraulic chain tensioners - Experiment and simulation,” *SAE Technical Papers*, SAE International, 2007, doi:10.4271/2007-01-1461.

97. Michele Calabretta, Diego Cacciatore, P.C. and J.P., “Development of a Timing Chain Drive Model for a High Speed Gasoline Engine,” *SAE Int. J. Engines* 4(1):432–440, 2011.

98. Prescott, W.C., Moss, K.D., and Powell, M.S., “Role of multibody dynamics in the design of chain drive systems,” *Proceedings of the ASME International Design Engineering Technical Conferences and Computers and Information in Engineering Conference - DETC2005*, ISBN 0791847438: 1841–1846, 2005, doi:10.1115/detc2005-84872.

99. LI Yi-min, HAO Zhi-yong, ZHANG Zhi-ming, YANG Guo-fang, F.F., “Simulation Research on Dynamic Characteristic of Timing Chain Trains of Gasoline Engine,” *Chinese Intern. Combust. Engine Eng.*, 2013.

100. Moreno, D., Mucchi, E., Dalpiaz, G., and Rivola, A., “Multibody Analysis of the Desmodromic Valvetrain of the Ducati MotoGp Engine,” *Proc. ECCOMAS, Multibody Dyn.*, 2007.

101. Rivola, A., Carlini, A., and Dalpiaz, G., “Modelling the elastodynamic behaviour of a desmodromic valve train,” *Proc. 2002 Int. Conf. Noise Vib. Eng. ISMA* 1417–1426, 2002.

102. Lin, S.T. and Hong, M.C., “Stabilization method for numerical integration of multibody mechanical systems,” *J. Mech. Des. Trans. ASME* 120(4):565–572, 1998, doi:10.1115/1.2829316.

103. Pogorelo, D., “Differential-algebraic equations in multibody system modeling,” *Numer. Algorithms* 19(1–4):183–194, 1998, doi:10.1023/A:1019131212618.

104. Flores, P. and Lankarani, H.M., “Numerical methods in multibody system dynamics,” *Solid Mechanics and its Applications*, Springer Verlag: 93–134, 2016, doi:10.1007/978-3-319-30897-5_5.

105. Neusser, Z., Sopouch, M., Schaffner, T., and Priebsch, H.H., “Multi-body dynamics based gear mesh models for prediction of gear dynamics and transmission error,” *SAE Technical Papers*, SAE International, 2010,

doi:10.4271/2010-01-0897.

106. Linke, H., “Stirnradverzahnung,” Hanser, ISBN 3446414649, 2010.

107. Hoffmann, N. and Gaul, L., “Effects of damping on mode-coupling instability in friction induced oscillations,” *ZAMM* 83(8):524–534, 2003, doi:10.1002/zamm.200310022.

108. Brusa, E., Delprete, C., and Genta, G., “Torsional vibration of crankshafts: Effects of non-constant moments of inertia,” *J. Sound Vib.* 205(2):135–150, 1997, doi:10.1006/jsvi.1997.0964.

109. Rivola, A. and Carlini, A., “A Camshaft Non-Linear Model for the Desmodromic Valve Train Simulation.”

110. Paranjpe, R.S., “Dynamic analysis of a valve spring with a coulomb-friction damper,” *J. Mech. Des. Trans. ASME* 112(4):509–513, 1990, doi:10.1115/1.2912639.

111. Akiba, K., Shimizu, A., and Sakai, H., “A comprehensive simulation of high speed driven valve trains,” *SAE Technical Papers*, SAE International, 1981, doi:10.4271/810865.

112. Wang, K.W., “Vibration analysis of engine timing chain drives with camshaft torsional excitations,” *SAE Prepr.* (244):196–207, 1991, doi:10.4271/911063.

113. Cikanek, S.R. and Bailey, K.E., “Regenerative braking system for a hybrid electric vehicle,” *Proceedings of the American Control Conference*, ISBN 0780372980: 3129–3134, 2002, doi:10.1109/ACC.2002.1025270.

114. Dang Van, K., Griveau, B., and Massage, O., “On a new multiaxial fatigue limit criterion: Theory and application,” *Biaxial and Multiaxial Fatigue* 479–496, 1989.

115. Van, K.D., Cailletaud, G., Flavenot, J.F., Douaron, A. Le, and Lieurade, H.P., “Criterion for high-cycle fatigue failure under multiaxial loading,” *Icbmff2*, 1986.

116. Sissa, S., Giacopini, M., and Rosi, R., “Low-cycle thermal fatigue and high-cycle vibration fatigue life estimation of a diesel engine exhaust manifold,” *Procedia Eng.* 74:105–112, 2014, doi:10.1016/j.proeng.2014.06.233.

117. Ceraolo, M., Donato, A. di, and Franceschi, G., “A general approach to energy optimization of hybrid electric vehicles,” *IEEE Trans. Veh. Technol.* 57(3):1433–1441, 2008, doi:10.1109/TVT.2007.909268.

118. Lyshevski, S.E. and Yokomoto, C., “Control of hybrid - Electric vehicles,” *Proc. Am. Control Conf.* 4(April):2148–2149, 1998, doi:10.1109/ACC.1998.703007.

119. Bass, E., Mabrito, B., Kong, H., and McAlwee, G., “A competition hybrid electric vehicle,” *SAE Tech. Pap.*, 1992, doi:10.4271/921544.

120. Tate, E.D. and Boyd, S.P., “Finding ultimate limits of performance for hybrid electric vehicles,” *SAE Tech. Pap.* (724), 2000, doi:10.4271/2000-01-3099.

121. Langari, R. and Won, J.S., “Intelligent energy management agent for a parallel hybrid vehicle - Part I: System architecture and design of the driving situation identification process,” *IEEE Trans. Veh. Technol.* 54(3):925–934, 2005, doi:10.1109/TVT.2005.844685.

122. Won, J.S. and Langari, R., “Intelligent energy management agent for a parallel hybrid vehicle - Part II: Torque distribution, charge sustenance strategies, and performance results,” *IEEE Trans. Veh. Technol.* 54(3):935–953, 2005, doi:10.1109/TVT.2005.844683.

123. Holder, C. and Gover, J., “Optimizing the hybridization factor for a parallel hybrid electric small car,” *2006 IEEE Veh. Power Propuls. Conf. VPPC 2006* 1:1–5, 2006, doi:10.1109/VPPC.2006.364359.

124. Buecherl, D., Bolvashenkov, I., and Herzog, H.G., “Verification of the optimum hybridization factor as design parameter of hybrid electric vehicles,” *5th IEEE Veh. Power Propuls. Conf. VPPC ’09* 847–851, 2009, doi:10.1109/VPPC.2009.5289758.

125. Patil, C., Varade, S., and Wadkar, S., “International Journal of Current Engineering and Technology A Review of Engine Downsizing and its Effects,” Jan. 2020.

126. Mierlo, J. Van, Bossche, P. Van den, and Maggetto, G., “Models of energy sources for EV and HEV: Fuel cells, batteries, ultracapacitors, flywheels and engine-generators,” *J. Power Sources* 128(1):76–89, 2004, doi:10.1016/j.jpowsour.2003.09.048.

127. Hu, X., Murgovski, N., Johannesson, L.M., and Egardt, B., “Comparison of three electrochemical energy buffers applied to a hybrid bus powertrain with simultaneous optimal sizing and energy management,” *IEEE Trans. Intell. Transp. Syst.* 15(3):1193–1205, 2014, doi:10.1109/TITS.2013.2294675.

128. Ehsani, M., Gao, Y., and Miller, J.M., “Hybrid electric vehicles: Architecture and motor drives,” *Proc. IEEE* 95(4):719–728, 2007, doi:10.1109/JPROC.2007.892492.

129. Xue, X.D., Cheng, K.W.E., and Cheung, N.C., “Selection of electric motor drives for electric vehicles,” ISBN 9781424441624, https://ieeexplore.ieee.org/abstract/document/4813059, 2008.

130. Carter, C.D., Sherman, C.B., and Matthews, R.D., “Design of a Formula SAE Race car,” 1982.

131. Liu, J. and Peng, H., “Modeling and control of a power-split hybrid vehicle,” *IEEE Trans. Control Syst. Technol.* 16(6):1242–1251, 2008, doi:10.1109/TCST.2008.919447.

132. Pisu, P. and Rizzoni, G., “A comparative study of supervisory control strategies for hybrid electric vehicles,” *IEEE Trans. Control Syst. Technol.* 15(3):506–518, 2007, doi:10.1109/TCST.2007.894649.

133. Salmasi, F.R., “Control strategies for hybrid electric vehicles: Evolution, classification, comparison, and future trends,” *IEEE Trans. Veh. Technol.* 56(5 I):2393–2404, 2007, doi:10.1109/TVT.2007.899933.

134. Pisu, P., Koprubasi, K., and Rizzoni, G., “Energy management and drivability control problems for hybrid electric vehicles,” *Proc. 44th IEEE Conf. Decis. Control. Eur. Control Conf. CDC-ECC ’05* 2005:1824–1830, 2005, doi:10.1109/CDC.2005.1582425.

135. Opila, D.F., Wang, X., McGee, R., Gillespie, R.B., Cook, J.A., and Grizzle, J.W., “An energy management controller to optimally trade off fuel economy and drivability for hybrid vehicles,” *IEEE Trans. Control Syst. Technol.* 20(6):1490–1505, 2012, doi:10.1109/TCST.2011.2168820.

136. Wei, X., Pisu, P., Rizzoni, G., and Yurkovich, S., “Dynamic modeling of a hybrid electric drivetrain for fuel economy, performance and driveability evaluations,” *American Society of Mechanical Engineers, Dynamic Systems and Control Division (Publication) DSC*, American Society of Mechanical Engineers (ASME): 443–450, 2003, doi:10.1115/IMECE2003-42548.

137. Lin, C.C., Peng, H., Grizzle, J.W., and Kang, J.M., “Power management strategy for a parallel hybrid electric truck,” *IEEE Trans. Control Syst. Technol.* 11(6):839–849, 2001.

138. Kim, J., Kim, N., Hwang, S., Hori, Y., and Kim, H., “Motor control of input-split hybrid electric vehicles,” *Int. J. Automot. Technol.* 10(6):733–742, 2009, doi:10.1007/s12239-009-0086-1.

139. Ilić-Spong, M., Miller, T.J.E., Macminn, S.R., and Thorp, J.S., “Instantaneous Torque Control of Electric Motor Drives,” *IEEE Trans. Power Electron.* PE-2(1):55–61, 1987, doi:10.1109/TPEL.1987.4766332.

140. Chen, Y., Song, L., and Evans, J.W., “Modeling studies on battery thermal behaviour, thermal runaway, thermal management, and energy efficiency,” *Proceedings of the Intersociety Energy Conversion Engineering Conference*, IEEE: 1465–1470, 1996, doi:10.1109/iecec.1996.553943.

141. Pang, S., Farrell, J., Du, J., and Barth, M., “Battery state-of-charge estimation,” *Proceedings of the American Control Conference*, 1644–1649, 2001, doi:10.1109/acc.2001.945964.

142. Zhang, Y., Jiang, Z., and Yu, X., “Control strategies for battery/supercapacitor hybrid energy storage systems,” *2008 IEEE Energy 2030 Conference, ENERGY 2008*, ISBN 9781424428502, 2008, doi:10.1109/ENERGY.2008.4781031.

143. Gao, Y., Chen, L., and Ehsani, M., Investigation of the Effectiveness of

Regenerative Braking for EV and HEV, *SAE Trans.* 108:3184–3190, Jan. 2020, doi:10.2307/44733986.

144. Ahn, J.K., Jung, K.H., Kim, D.H., Jin, H.B., Kim, H.S., and Hwang, S.H., "Analysis of a regenerative braking system for Hybrid Electric Vehicles using an Electro-Mechanical Brake," *Int. J. Automot. Technol.* 10(2):229–234, 2009, doi:10.1007/s12239-009-0027-z.

145. Peng, D., Zhang, Y., Yin, C.L., and Zhang, J.W., "Combined control of a regenerative braking and antilock braking system for hybrid electric vehicles," *Int. J. Automot. Technol.* 9(6):749–757, 2008, doi:10.1007/s12239-008-0089-3.

146. Gao, Y. and Ehsani, M., Electronic Braking System of EV And HEV---Integration of Regenerative Braking, Automatic Braking Force Control and ABS, *SAE Trans.* 110:576–582, 2001, doi:10.2307/44718374.

147. Tanaka, H., Takemori, D., Miyachi, T., Iribe, Y., and Oguri, K., "Analysis of drivers' anxiety and security during the braking of a vehicle," *IEICE Trans. Fundam. Electron. Commun. Comput. Sci.* E100A(2):466–472, 2017, doi:10.1587/transfun.E100.A.466.

148. Naito, M., Koike, Y., Osaki, S., Morishita, S., and Quan, N., "Development of regenerative cooperative braking system with conventional ESC," *SAE Technical Papers*, SAE International, 2014, doi:10.4271/2014-01-0331.

149. Nüesch, T., Cerofolini, A., Mancini, G., Cavina, N., Onder, C., and Guzzella, L., "Equivalent Consumption Minimization Strategy for the Control of Real Driving NOx Emissions of a Diesel Hybrid Electric Vehicle," *Energies* 7(5):3148–3178, 2014, doi:10.3390/en7053148.

150. Musardo, C., Rizzoni, G., Guezennec, Y., and Staccia, B., "A-ECMS: An adaptive algorithm for hybrid electric vehicle energy management," *Eur. J. Control* 11(4–5):509–524, 2005, doi:10.3166/ejc.11.509-524.

151. Onori, S., Serrao, L., and Rizzoni, G., "Adaptive equivalent consumption minimization strategy for hybrid electric vehicles," *ASME 2010 Dynamic Systems and Control Conference, DSCC2010*, ISBN 9780791844175: 499–505, 2010, doi:10.1115/DSCC2010-4211.

152. Park, J. and Park, J.H., "Development of equivalent fuel consumption minimization strategy for hybrid electric vehicles," *Int. J. Automot. Technol.* 13(5):835–843, 2012, doi:10.1007/s12239-012-0084-6.

153. Rezaei, A., Burl, J.B., and Zhou, B., "Estimation of the ECMS Equivalent Factor Bounds for Hybrid Electric Vehicles," *IEEE Trans. Control Syst. Technol.* 26(6):2198–2205, 2018, doi:10.1109/TCST.2017.2740836.

154. Malikopoulos, A.A., "Supervisory power management control algorithms for hybrid electric vehicles: A survey," *IEEE Trans. Intell. Transp. Syst.* 15(5):1869–1885, 2014, doi:10.1109/TITS.2014.2309674.

155. Chen, J.S. and Salman, M., "Learning energy management strategy for

hybrid electric vehicles," *2005 IEEE Vehicle Power and Propulsion Conference, VPPC*, ISBN 0780392809: 427–432, 2005, doi:10.1109/VPPC.2005.1554593.

156. Crolla, D.A., Ren, Q., ElDemerdash, S., and Yu, F., "Controller design for hybrid vehicles - State of the art review," *2008 IEEE Vehicle Power and Propulsion Conference, VPPC 2008*, ISBN 9781424418497, 2008, doi:10.1109/VPPC.2008.4677808.

157. Gandhi, K.K., Zvonow, V.A., and Singh, H., "Development of a driving cycle for fuel economy in a developing country," *Transp. Res. Part A Gen.* 17(1):1–11, 1983, doi:10.1016/0191-2607(83)90128-0.

158. Kuhler, M. and Karstens, D., "Improved driving cycle for testing automotive exhaust emissions," *SAE Technical Papers*, SAE International, 1978, doi:10.4271/780650.

159. Reeven, V. Van, Hofman, T., Huisman, R., and Steinbuch, M., "Extending Energy Management in Hybrid Electric Vehicles with explicit control of gear shifting and start-stop," *Proceedings of the American Control Conference*, ISBN 9781457710957: 521–526, 2012, doi:10.1109/acc.2012.6315200.

160. Pacejka, H.B. and Bakker, E., "The magic formula tyre model," *Veh. Syst. Dyn.* 21(sup1):1–18, 1992, doi:10.1080/00423119208969994.

161. Kim, N., Cha, S.W., and Peng, H., "Optimal equivalent fuel consumption for hybrid electric vehicles," *IEEE Trans. Control Syst. Technol.* 20(3):817–825, 2012, doi:10.1109/TCST.2011.2123099.